Title

Generating, Enhancing, and Leveraging Nonlinear and Electro-Optic Effects in Silicon-Based Waveguides

Author

Puckett, Matthew Wade

Publication Date

2016

UNIVERSITY OF CALIFORNIA, SAN DIEGO

Generating, Enhancing, and Leveraging Nonlinear and Electro-Optic Effects in Silicon-Based Waveguides

A dissertation submitted in partial satisfaction of the requirements for the degree Doctor of Philosophy

in

Electrical Engineering (Photonics)

by

Matthew Wade Puckett

Committee in charge:

Professor Yeshaiahu Fainman, Chair
Professor Dimitri Basov
Professor Eric Fullerton
Professor Boubacar Kante
Professor Andrew Kummel

2016

The Dissertation of Matthew Wade Puckett is approved, and it is acceptable in quality and form for publication on microfilm and electronically:

Chair

University of California, San Diego

2016

DEDICATION

I would like to dedicate this dissertation to my mother Winnie, my father Zane, and my older sister Sarah, who have always encouraged me to commit myself fully to all of my pursuits. If not for the values they instilled in me, I doubt that I would have had the conviction to pursue my education to such an extent as this.

Put more simply, none of this would have been possible without the help of my family. Thanks so much, I love you!

EPIGRAPH

The secret of change is to focus all of your energy, not on fighting the old, but on building the new.

Socrates

TABLE OF CONTENTS

LIST OF ABBREVIATIONS

CMOS	Complementary metal-oxide-semiconductor
TE	Transverse electric
TM	Transverse magnetic
DBR	Distributed Bragg reflector
FSR	Free spectral range
EFISH	Electric field-induced second-harmonic generation
MOS	Metal-oxide-semiconductor
EBL	Electron beam lithography
SOI	Silicon-on-insulator
PECVD	Plasma-enhanced chemical vapor deposition
RIE	Reactive ion etching
ALD	Atomic layer deposition
EDFA	Erbium-doped fiber amplifier
FEM	Finite element method
FDTD	Finite-difference time-domain
HSQ	Hydrogen silsesquioxane
TMAH	Tetramethylammonium hydroxide
CV	Capacitance-voltage
SEM	Scanning electron microscope
SHG	Second-harmonic generation

THG	Third-harmonic generation
DFWM	Degenerate four-wave mixing
EO	Electro-Optic

LIST OF SYMBOLS

λ_0	Free-space wavelength
c	Speed of light
ν	Frequency
ω	Angular frequency
ε_0	Permittivity of free space
ε	Permittivity
ε_r	Relative permittivity
μ_0	Permeability of free space
μ	Permeability
μ_r	Relative permeability
E	Electric field
D	Electric flux density
H	Magnetic field
B	Magnetic flux density
P	Polarization
C	Capacitance
$P^{(2)}$	Second-order polarization
A	Mode amplitude
M	Transmission/Transformation matrix
α	Attenuation coefficien

β	Phase constant
τ	Attenuation factor
κ	Coupling coefficient
t	Transmission coefficient
θ	Phase
$\Delta\lambda_{3dB}$	Full-width at half-maximum
n_g	Group index
Q	Quality factor
τ_p	Photon lifetime
χ	Linear susceptibility
$\chi^{(2)}$	Second-order nonlinear susceptibility
$\chi^{(3)}$	Third-order nonlinear susceptibility
Γ	Confinement factor
Λ	Grating period
σ	Electrical conductivity
ρ	Electrical resistivity
ρ_f	Bound charge density
J_f	Free electrical current
k_0	Free-space wavenumber
Γ	Confinement factor
β	Guided wavenumber

n_{eff}	Effective index
L_c	Coherence length
N_e	Electron concentration
N_h	Hole concentration
ρ	Electrical resistivit

LIST OF FIGURES

ACKNOWLEDGEMENTS

I would like to thank my advisor, Yeshaiahu Fainman, for the incredible amount of time and effort he has put into not only my own education, but the education of each and every one of his students throughout his tenure as a professor. It means one thing to care about doing good research, but quite another to care about helping people, and I can proudly say that my advisor values these two goals equally. Having been an expert in the field of photonics since before I was born, Professor Fainman has been the most well-equipped mentor I can imagine, and I feel luckier than I can articulate to have been given the opportunity to benefit from his knowledge, and to have worked under him over these past five years.

The other members of my doctoral committee, Professor Eric Fullerton, Professor Boubacar Kante, Professor Dimitri Basov, and Professor Andrew Kummel, deserve my sincere thanks as well. I have worked with Professor Fullerton to fabricate unique metamaterials based on dielectric-semiconductor superlattices, and his facilities at the Center for Memory and Recording Research have been beneficial for the characterization of these structures. Professor Boubacar Kante is an expert in the field of electromagnetics, and his insight into the behavior of silicon waveguides patterned on the nanoscale has been hugely beneficial. Professors Dimitri Basov and Andy Kummel have offered sage advice to my work as well, and Professor Andy Kummel in particular offered feedback during my qualifying exam which has led to a significant redirection and improvement of my work.

I would also like to thank the wonderful group members I have been allowed to work with. To do research of any real value, it is important to be able to work together with others as a cohesive unit, and throughout my graduate program I have been consistently amazed by the willingness and capability of my peers to work alongside me. In particular I would like to the Rajat Sharma, with whom I worked very closely. He is incredibly intelligent and talented, and I doubt that either of us could have accomplished anything near what we have without the other’s support.

My friends (Schuyler Madsen, Matthew Bowersox, Paul Blackwell, and Mighells Deuel in particular) and my family have provided steadfast support throughout my time here at UCSD, and I would like to thank them as well. My fiancé Cassidy Sossaman has shown unfailing patience and understanding where my work is involved, and has consistently encouraged me to do the best I can.

Lastly, I would like to thank the many agencies which sponsored my work, including The National Science Foundation, the Defense Advanced Research Projects Agency, and the Office of Naval Research. Scientific research is a notoriously expensive pursuit, and none of this would have been possible without their funding.

Again, thank you all so much. I’m so grateful to have been allowed to do such fascinating work at this incredible university.

Chapter 2 contains material which has been published in, "Tensor of the Tensor of the second-order nonlinear susceptibility in asymmetrically strained silicon waveguides: analysis and experimental validation,” Optics Letters (2014). The dissertation author was the primary investigator and author of this paper.

Chapter 2 contains material which has been published in, "Effect of dielectric claddings on the electro-optic behavior of silicon waveguides," Optics Letters (2016). The dissertation author was the primary investigator and author of this paper.

Chapter 3 contains material which is being prepared for submission. The dissertation author was the primary investigator of this work.

Chapter 4 contains material which has been submitted for publication in, "Observation of second-harmonic generation in silicon nitride waveguides through bulk nonlinearities," Optics Letters. The dissertation author was the primary investigator and author of this paper.

Chapter 4 contains material which is being prepared for submission. The dissertation author was the primary investigator of this work.

VITA

2010-2011	Undergraduate Student Researcher, University of California, Los Angeles
2011	Bachelor of Science, University of California, Los Angeles
2011-2013	Research Assistant, Department of Electrical and Computer Engineering, University of California, San Diego
2013	Master of Science, University of California, San Diego
2013-2015	Research Assistant, Department of Electrical and Computer Engineering, University of California, San Diego
2015	Candidate of Philosophy, University of California, San Diego
2015-2016	Research Assistant, Department of Electrical and Computer Engineering, University of California, San Diego
2016	Doctor of Philosophy, University of California, San Diego

PUBLICATIONS

J. S. T. Smalley, M. W. Puckett, and Y. Fainman, “Invariance of optimal composite waveguide geometries with respect to permittivity of the metal cladding,” Optics Letters **38**, 5161-5164 (2013).

M. W. Puckett, J. S. T. Smalley, M. Abashin, A. Grieco, and Y. Fainman, “Tensor of the second-order nonlinear susceptibility in asymmetrically strained silicon waveguides: analysis and experimental validation,” Optics Letters **39**, 1693-1696 (2014).

M. W. Puckett, F. Vallini, A. Grieco, and Y. Fainman, “Multichannel Bragg gratings in silicon waveguides with asymmetric sidewall modulation,” Optics Letters **40**, 379-382 (2015).

R. Sharma, M. W. Puckett, H. Lin, F. Vallini, and Y. Fainman, “Characterizing the effects of free carriers in fully etched, dielectric-clad silicon waveguides,” Applied Physics Letters **106**, 241104 (2015).

M. W. Puckett, R. Sharma, F. Vallini, S. Shahin, F. Monifi, P. N. Barrina, S. Mehravar, K. Kieu, and Y. Fainman, "Silicon Nanoridge Array Waveguides for Nonlinear and Sensing Applications," Optics Express **23**, 28224-28233 (2015).

R. Sharma, M. W. Puckett, H. Lin, A. Isichenko, F. Vallini, and Y. Fainman, "The effect of dielectric claddings on the electro-optic behavior of silicon waveguides," Optics Letters **41**, 1185-1188 (2016).

M. W. Puckett, R. Sharma, H. Lin, M. Yang, F. Vallini, and Y. Fainman, "Observation of second-harmonic generation in silicon nitride waveguides through bulk nonlinearities," Optics Express (In submission).

FIELDS OF STUDY

Major Field: Electrical Engineering (Photonics)

Studies in Electromagnetism
Professors Yeshaiahu Fainman, Eric Fullerton, and Boubakar Kante

Studies in Chemistry
Professor Andrew Kummel

Studies in Physics
Professor Dimitri Basov

ABSTRACT OF THE DISSERTATION

Generating, Enhancing, and Leveraging Nonlinear and Electro-Optic Effects in Silicon-Based Waveguides

by

Matthew Wade Puckett

Doctor of Philosophy in Electrical Engineering (Photonics)

University of California, San Diego, 2016

Professor Yeshaiahu Fainman, Chair

In integrated photonics, most fundamental device functionalities rely on nonlinear or electro-optic phenomena, and optical waveguides with higher second- and third-order nonlinear coefficients are generally desirable for high-efficiency modulators and wavemixers. Silicon, despite being a material of interest due to its prevalence in the electronics industry, intrinsically lacks a second-order nonlinear susceptibility, so a great deal of work in the literature has been focused on circumventing this shortcoming by either (1) relying instead on free-carrier plasma dispersion or (2) generating strain-induced second-order effects. This dissertation focuses primarily on providing a comprehensive study of the nonlinear effects in silicon waveguides, with the intent of determining which phenomena and consequent waveguide designs are the most desirable for achieving modulation and wavemixing, respectively. A detailed analysis is additionally applied to the integration of silicon with other media with favorable optical properties, with the goal of designing hybrid waveguides with enhanced nonlinear coefficients. Electro-optic and wavemixing measurements are performed using combination fiber, integrated, and free-space optical setups, and the experimental data show conclusively that conventional silicon waveguide topologies may be modified to improve the performance of modulators and wavemixers in terms of (1) energy efficiency, (2) device footprint, and (3) speed. This work is intended to contribute to the study of nonlinear integrated photonics, ideally advancing the ongoing assimilation of the field by electronics and leading to the eventual design of hybrid photonic-electronic circuits.

Chapter 1:

Introduction

1.1: The Current State of Silicon Photonics

Since the initial discovery of silicon's transparency beyond wavelengths of 1.2 µm, this cheap, readily available semiconductor has been generally accepted as an ideal candidate for the guiding of light in photonics circuits, particularly in the telecommunication C-band ranging from 1530 to 1565 nm [1]. The field of integrated photonics was established with silicon at its heart in the mid 1980's [2,3], and research from that point onward has been focused on the optimization of silicon waveguides in terms of (1) reducing their propagation loss [4], (2) increasing fiber-to-chip coupling efficiency [5,6], (3) controlling wavelength dispersion [7], (4) understanding and leveraging multimodal properties [8], and (5) exploring the generation and exploitation of different nonlinear optical effects [9]. To date, the vast majority of these topics has been exhaustively studied, and the performance of silicon waveguides has steadily improved in conjunction with fabrication capabilities and physical intuition [10].

One of the most critical obstacles still faced by integrated silicon photonics is the improvement of optical modulators and switches. Modulation of light has historically been achieved in silicon waveguides through the free-carrier plasma dispersion effect [11-13], in which deviations in the concentrations of electrons and holes in silicon lead to changes in both the real and imaginary parts of the material's index of refraction. The most critical metric for an optical modulator is the switching voltage, defined here as the energy required to turn transmission through an optical device from “on” to “off,” or vice versa, and modulation based on the free-carrier plasma dispersion effect has been shown to have switching energies as low as 7.5 mV/bit [12]. A second important metric called the modulation bandwidth determines the maximum frequency at which switching may be performed, and consequently sets a limit on the amount of data which may be encoded into the optical regime via an applied voltage. For the free-carrier plasma dispersion effect, roll-off generally occurs beyond 1 GHz [14].

In order to increase this second figure of merit, some work over the past decade has focused on generating and leveraging second-order optical nonlinearities in silicon through strain-engineering [15,16]. The Pockels effect, which can be used in interferometric structures to achieve electro-optic modulation, is known to have a faster response time than the free-carrier plasma dispersion effect, and can therefore achieve higher bandwidths [17]. Because of this, the realization of a Pockels effect-based modulator in strain-engineered silicon, which will be discussed in greater detail in Chapter 2, is obviously desirable. However, recent studies suggest that the generation of this effect in semiconductors may not be as straightforward as initially anticipated [18-20]. This dissertation will discuss the complicating effects which exist in this field of study, in addition to designing and testing new waveguide designs based on a more complete understanding of silicon’s nuanced electro-optic responses to applied bias voltages and currents.

A second critical device functionality, wavemixing, is used in integrated photonic circuits to increase the number of wavelength data channels and consequently increase the data capacity of optical transceivers [9]. Around one central wavelength, degenerate four-wave mixing achieves this functionality by coupling energy from a pump and a signal into a third wavelength called the idler [21], and this phenomenon is fairly well-understood in silicon [22]. However, many applications additionally require photonic circuits to generate optical power in distinct telecommunication bands, and this is most readily achieved through such second-order wavemixing phenomena as second-harmonic generation [23]. Again silicon's lack of a second-order nonlinearity becomes problematic, but strain-engineering may serve here as well to remove the material's shortcoming. Several demonstrations of second-harmonic generation in silicon suggest that, for this particular application, asymmetric strain does show potential, but again there are other complicating effects at work as well [24,25]. In the context of wavemixing, just as in modulation, this dissertation aims to decouple the effects involved and determine an ideal waveguide design for the task at hand.

If complementary metal-oxide-semiconductor (CMOS) fabrication allows [26], it may additionally be beneficial to combine other media with silicon for the design of nonlinear hybrid waveguides. The benefits of such waveguides would be that they could leverage silicon's transparency and high index of refraction for the purposes of guiding, while additionally making use of the potentially preferable optical properties of dielectrics such as silicon nitride, zinc oxide, titanium dioxide, or aluminum oxide [27]. This dissertation will consider the feasibility of such hybrid waveguides, both in terms of fabrication and characterization, and will provide a theoretical analysis of their linear and nonlinear optical properties for both modulation and second- and third-order wavemixing.

It is the author's hope that this dissertation will serve as a comprehensive breakdown of both the linear and nonlinear properties of silicon waveguides, in addition to introducing prospective waveguide geometries with unique, freely tunable, and desirable characteristics. As the demand for highly evolved optical circuits continues to grow alongside the field of information technology, it is anticipated that the conclusions drawn from this work will become increasingly important to the photonics and electronics academic communities as well as their industrial analogues.

But first, the current chapter aims to introduce the reader to some of the more fundamental concepts surrounding silicon waveguides, including (1) the derivation of optical modes in transparent media, (2) the coupling of light between waveguide modes, and (3) the physics which define the operation of some common device components. A brief overview of these topics is essential before moving on to a discussion of the nonlinear properties of silicon waveguides, the ways in which they are leveraged, and the means which have been developed for their generation and enhancement.

1.2: Optical Waveguide Modes

The fundamental relations which govern the properties of electromagnetic waves are given by the collectively-named Maxwell's equations, which came hard-earned through years of study and observation during the nineteenth century [28]. These equations are given in their differential form as:

$$\nabla \cdot D = \rho_f \tag{1.1}$$

$$\nabla \cdot B = 0 \tag{1.2}$$

$$\nabla \times E = \frac{-\partial B}{\partial t} \tag{1.3}$$

$$\nabla \cdot H = J_f + \frac{\partial D}{\partial t} \tag{1.4}$$

where D is the electric flux density in units of Cm^{-2}, ρ_f is the bound charge density in units of Cm^{-3}, B is the magnetic flux density in units of Wbm^{-2}, E is the electric field in units of Vm^{-1}, H is the magnetic field in units of Am^{-1}, and J_f is the free electrical current in units of Am^{-2}. In these equations, the magnetic and electric fields and flux densities are additionally related as:

$$D = \varepsilon E \tag{1.5}$$

$$B = \mu H \tag{1.6}$$

where ε and μ are the permittivity and permeability of the medium under consideration.

Now let us assume that an electromagnetic field propagates along one direction, say the z-axis, and let us additionally enforce that it has a constant shape of varying magnitude along an unperturbed x-y cross-section. Specifically, let us assume the cross-sectional geometry of a conventional silicon waveguide, shown for reference in Fig. 1.1.

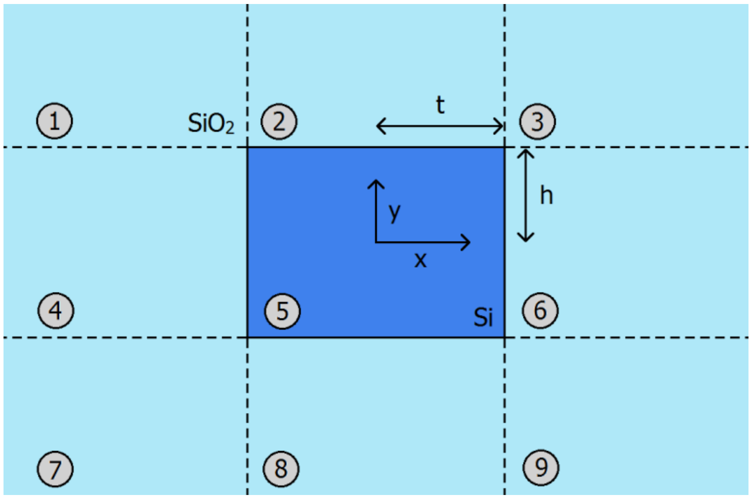

Figure 1.1. Cross-section of a silicon waveguide with arbitrary height 2t and width 2w.

We may then define the vector electric and magnetic fields of the wave, respectively, as:

$$E(x,y,z,t)=E(x,y)e^{j\omega t-jkz} \tag{1.7}$$

$$H(x,y,z,t)=H(x,y)e^{j\omega t-jkz} \tag{1.8}$$

where k is the propagation wavenumber and ω is the wave's angular frequency. The wavenumber may be defined in turn as:

$$k=\frac{2\pi}{\lambda_0}n_{eff} \tag{1.9}$$

where λ_0 is the free-space wavelength and n_{eff} is the effective refractive index defined for the wave. By requiring that this proposed solution for the wave adheres to Maxwell's equations, we may derive a relation known as the wave equation, which relates the transverse gradient of the field to its wavenumber based on the medium in which the wave exists and the its angular frequency. This equation may be written for the electric and magnetic fields as:

$$\nabla_{\perp}{}^{2}E = (\omega^{2}\mu\varepsilon - k^{2})E \tag{1.10}$$

$$\nabla_{\perp}{}^{2}H = (\omega^{2}\mu\varepsilon - k^{2})H \tag{1.11}$$

In these expressions, which must hold true in each of the constituent media in which the wave exists, $\nabla_{\perp}$ represents the transverse gradient. Despite the fact that ε changes value between silicon and silicon dioxide, k must remain constant for a given solution, and this requires the transverse distributions of the electric and magnetic fields to have specific functional forms in each of the media under consideration. In regions where $\omega^{2}\mu\varepsilon\text{-}k^{2}$ is positive, the electric and magnetic fields have solutions of the general form:

$$E(x,y) = \left[A_1\cos(\beta_x x) + B_1\sin(\beta_x x)\right]\left[C_1\cos(\beta_y y) + D_1\sin(\beta_y y)\right] \tag{1.12}$$

$$H(x,y) = \left[A_2\cos(\beta_x x) + B_2\sin(\beta_x x)\right]\left[C_2\cos(\beta_y y) + D_2\sin(\beta_y y)\right] \tag{1.13}$$

where β_x and β_y are the transverse wavenumbers in the x- and y-direction, respectively, and the capitalized variables are arbitrary scaling coefficients. In this case, it is necessary that $\beta_x^2+\beta_y^2+k^2=\omega^2\mu\varepsilon$. On the other hand, in regions where $\omega^{2}\mu\varepsilon\text{-}k^{2}$ is negative, the solution instead takes the general form:

$$E(x,y) = \left[A_1 e^{-\alpha_x(x-t)} + B_1 e^{\alpha_x(x+t)}\right]\left[C_1 e^{-\alpha_y(y-h)} + D_1 e^{\alpha_y(y+h)}\right] \tag{1.14}$$

$$H(x,y) = \left[A_2 e^{-\alpha_x(x-t)} + B_2 e^{\alpha_x(x+t)}\right]\left[C_2 e^{-\alpha_y(y-h)} + D_2 e^{\alpha_y(y+h)}\right] \tag{1.15}$$

where α_x and α_y are the attenuation coefficients in the x- and y-direction, respectively, and t and h are the cross-sectional dimensions of the structure as shown in Fig. 1.1. In this case, it is necessary that $-\alpha_x^2-\alpha_y^2+k^2=\omega^2\mu\varepsilon$. It is important to note that, in each of the nine regions shown in Fig. 1.1, the variables A_1 through D_2 are independently redefined to adhere to Maxwell's equations.

The number of solutions which satisfy the previously outlined conditions will change depending on (1) the permittivities and permeabilities of the media under consideration, and (2) the dimensions of the silicon region in Fig. 1.1. Finite-element method (FEM) software such as Comsol may be used to derive the solutions to these equations numerically, and Fig. 1.2 plots the effective indices of the solutions against the variable 2t, assuming a 2h=250 nm-tall waveguide composed of silicon, an infinitely extending cladding in each direction of silicon dioxide, and a free-space wavelength of 1.55 μm [29].

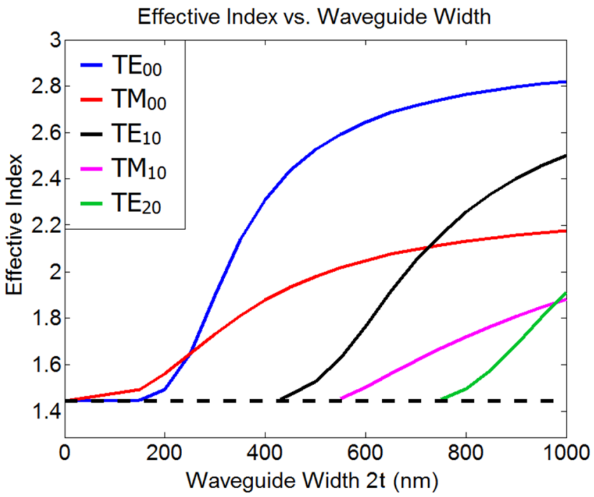

Figure 1.2. Effective indices of the different modes supported by a 250 nm-tall silicon waveguide with silicon dioxide cladding, as a function of the waveguide width. The horizontal dashed line represents the cutoff effective index, below which guided modes are not supported.

Fig. 1.2 shows data for two modes, identified here as TE_{00} and TM_{00}, which will be supported for infinitely small waveguide dimensions, whereas the higher-order modes only appear after certain cutoff dimensions are reached. TE_{00} and TM_{00} are typically the only two modes which are of interest in integrated silicon photonics, as they may be easily coupled into and out of via lensed tapered optical fibers [6]. As a result, the widths of silicon waveguides are generally maintained at values less than 400 nm, especially across regions at which coupling among modes may occur, in order to limit operation to these two modes of interest.

1.3: Mode Coupling

In this section, the theory of mode perturbation which leads to coupling either within or among waveguides will be briefly reviewed in the context of a 250 nm-tall, 500 nm-wide waveguide, in which only the TE_{00} and TM_{00} modes are supported. This analysis, which dates back over 50 years [30,31], is critical to the design of waveguide gratings and couplers [32], Bragg resonators [33], Mach-Zehnder interferometers [34], and ring and racetrack resonators [35], among many other device components in integrated photonics.

Likely the most straightforward instance in which coupling occurs is the case in which two waveguides are placed in close proximity to one another, as shown in Fig. 1.3a. If the modes of one waveguide overlap significantly with those of the other, we may instead think of the two as a new, combined waveguide which supports its own “supermodes” [36]. The two TE-like supermodes supported by the structure in Fig. 1.3a are shown in Fig. 1.3b and Fig. 1.3c, assuming a separation between two 500 nm-wide waveguides of 150 nm, and these are known as symmetric and antisymmetric supermodes, respectively.

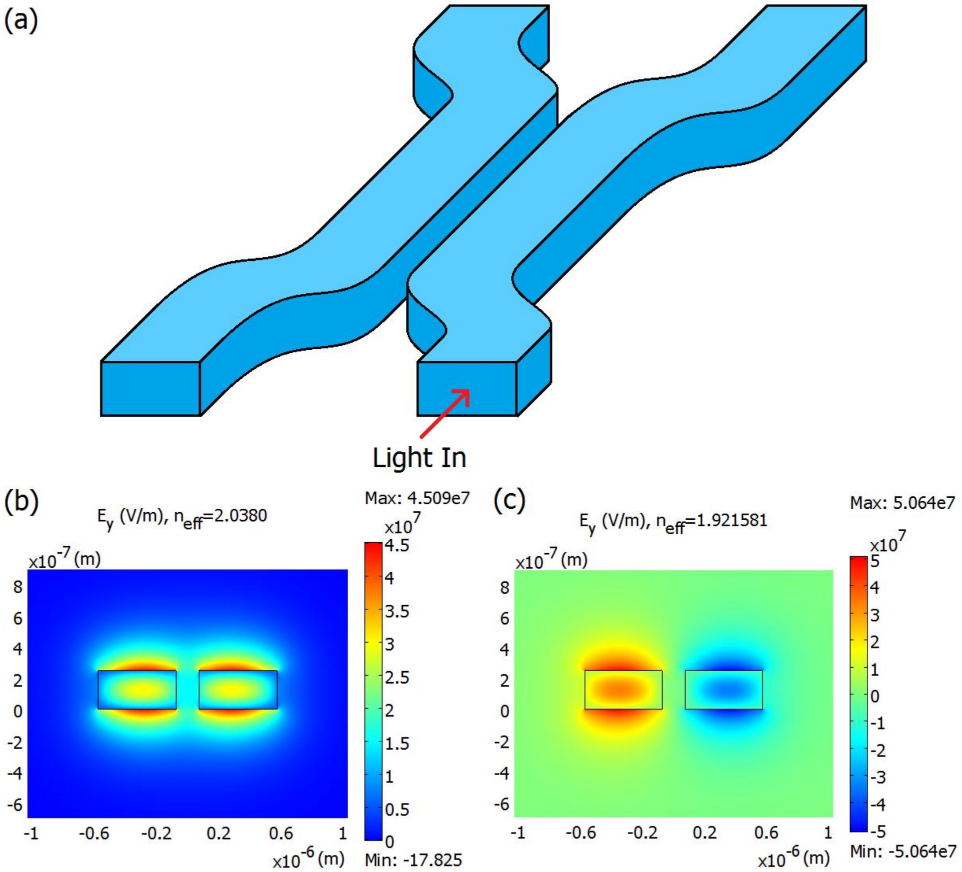

Figure 1.3. (a) A codirectional coupler, consisting of two silicon waveguides placed in close proximity. (b,c) Vertical electric field component of the (b) symmetric and (c) antisymmetric TM-like supermodes supported by the coupling section.

Let us assume (1) that the two waveguides under consideration are initially far away from one another and are gradually brought close together, and (2) that only the TM_{00} mode of one of the waveguides has been excited at the input. For this case, illustrated in Fig. 1.3a, we may decompose the input mode into a linear combination of the supermodes supported by the coupled waveguide system. In other words, half of the input field’s energy will couple into the symmetric TM-like supermode, whereas a second half will couple into the antisymmetric TM-like supermode. Because the two supermodes propagate with different wavenumbers defined by their dissimilar indices of refraction, listed in Fig. 1.3b and Fig. 1.3c, they will gradually move out of phase relative to each other, and when the waveguides are eventually moved apart, the interference of the two supermodes with one another will determine the splitting ratio of energy between the two waveguides.

Fig. 1.4 shows the results of several two-dimensional FEM model intended to illustrate this effect, clearly showing that for certain coupling lengths, 100% of the energy contained in the input mode may be coupled from the upper waveguide to the lower one. The shortest length for which this occurs may be calculated based on the phase mismatch between the two supermodes as:

$$L_c = \frac{\lambda_0}{2\left(n_{sym} - n_{antisym}\right)} \tag{1.16}$$

where n_{sym} and $n_{antisym}$ are the effective indices of the symmetric and antisymmetric supermodes, respectively. As the two waveguides are moved closer together, the index mismatch between the asymmetric and symmetric supermodes increases, and the coupling length L_c consequently decreases. Naturally, this type of coupling becomes more complicated when, for example, the two waveguides are not the same width or height, but a discussion of this distinction is not necessary for the purposes of this dissertation, and may be readily found in the literature [37].

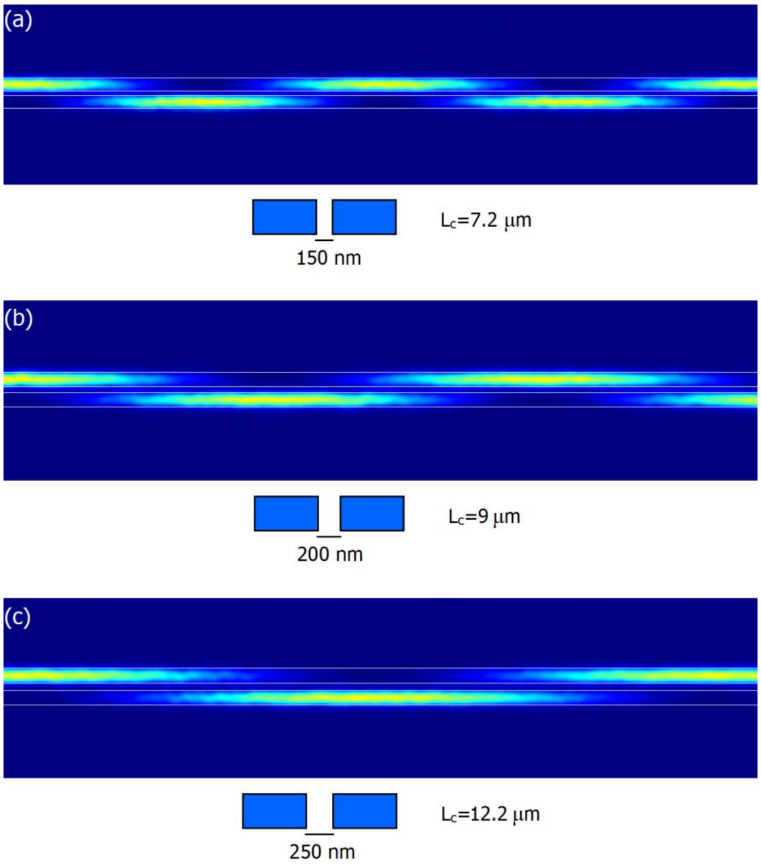

Figure 1.4. Codirectional coupling between 500 nm-wide, 250 nm-tall waveguides separated by (a) 150 nm, (b) 200 nm, and (c) 250 nm.

1.4: Resonant Waveguides

Even within a single waveguide, any perturbation to the waveguide cross-section may additionally cause modes to exchange energy with one another. For this type of coupling, it is beneficial to formally introduce the theoretical approach commonly referred to as the coupled mode theory [30,31]. As an example, we may consider the structure shown in Fig. 1.5a, in which the sidewalls of a waveguide are periodically moved either closer to or farther away from its center. Devices which rely on periodic modulation to achieve reflection are known as distributed Bragg reflectors (DBR's) [38].

The modes supported by the uncorrugated waveguide, defined generally by Eq. 1.7 and 1.8, satisfy Maxwell's equations as:

$$\nabla \times \left(H_m e^{-jk_m z} \right) = \varepsilon \frac{\partial \left(E_m e^{-jk_m z} \right)}{\partial t} \tag{1.17}$$

$$\nabla \times \left(E_m e^{-jk_m z} \right) = \mu \frac{\partial \left(H_m e^{-jk_m z} \right)}{\partial t} \tag{1.18}$$

where m is used to distinguish between the different supported modes. The perturbation by the sidewall modulation presents to the normal waveguide cross-section may be incorporated into Maxwell's equations as a position-dependent deviation from the linear polarization with which the supported fields interact [39]. The fields in the presence of this perturbation must then satisfy:

$$\nabla \times H = \varepsilon \frac{\partial E}{\partial t} + \frac{\partial \Delta P}{\partial t} \tag{1.19}$$

$$\nabla \times E = \mu \frac{\partial H}{\partial t} \tag{1.20}$$

By combining Eq. 1.17-1.20, we can obtain:

$$\nabla\left(E \times \left(H_m e^{-jk_m z}\right)^* + \left(E_m e^{-jk_m z}\right)^* \times H\right) = -i\omega\left(E_m e^{-jk_m z}\right)^* \Delta P \tag{1.21}$$

and integrating 1.21 over the entire x-y cross-section further yields:

$$\iint \frac{\partial}{\partial z}\left(E_t \times \left(H_{t,m} e^{jk_m z}\right)^* + \left(E_{t,m} e^{jk_m z}\right)^* \times H_t\right) dxdy = -i\omega \iint \left(E_m e^{jk_m z}\right)^* \Delta P dxdy \tag{1.22}$$

An important assumption to make at this point is that the perturbation presented by the sidewall modulation is sufficiently weak that the total field at any point may still be treated as a linear combination of the unperturbed modes:

$$E_t(x,y,z) = \sum_m A_m E_{t,m} e^{-jk_m z} \tag{1.23}$$

$$H_t(x,y,z) = \sum_m A_m H_{t,m} e^{-jk_m z} \tag{1.24}$$

Applying these definitions of the total field to Eq. 1.22 and exploiting the orthonormality of the modes then provides us with a fairly explicit equation defining the spatial evolution of the amplitude of mode m:

$$\frac{\partial A_m}{\partial z} = -i\omega \iint E_m{}^* e^{jk_m z} \Delta P dxdy \tag{1.25}$$

The perturbing polarization caused by the corrugation may be written as:

$$\Delta P = \Delta\varepsilon E = \Delta\varepsilon \sum_m E_m e^{-jk_m z} \tag{1.26}$$

and combining this with Eq. 1.25 yields:

$$\frac{\partial A_m}{\partial z} = -i \sum_n \kappa_{mn} A_n e^{j(k_m - k_n)z} \tag{1.27}$$

$$\kappa_{mn} = \omega \iint \Delta\varepsilon E_m{}^{*} E_n dxdy \tag{1.28}$$

To illustrate this point, again consider the silicon waveguide grating illustrated in Fig. 1.5a. For this particular device component, the index perturbation contains a complex term of the form $e^{j\Lambda z}$, where Λ is the period of the modulation. When the wavelength of light is such that:

$$\frac{2\pi}{\Lambda} = k_m - k_{-m} = 2k_m \tag{1.29}$$

Eq. 1.27 becomes purely imaginary, and energy is coupled coherently from the forward-propagating mth mode into the same mode propagating in the reverse direction. Because this phase-matching condition can only be obtained for one wavelength with a single grating period, the transmission spectra of these sidewall-modulated couplers, known commonly as Bragg gratings [40], strongly reflect light within their stopbands, and transmit data at other wavelengths. The transmission spectrum of the fundamental TE-like mode for the grating in Fig. 1.5a, generated used the finite-difference time-domain (FDTD) software Lumerical [41], is shown in Fig. 1.5b to elucidate this point.

Coupling between the supported modes of waveguides will occur, in general, any time a perturbation is presented to the waveguide geometry, and coupled mode theory is a powerful tool in determining how and between which modes coupling will occur. In the next section, some of the basic components which are employed in nonlinear photonic devices will be discussed, bearing in mind the broad review of coupled-mode theory presented here.

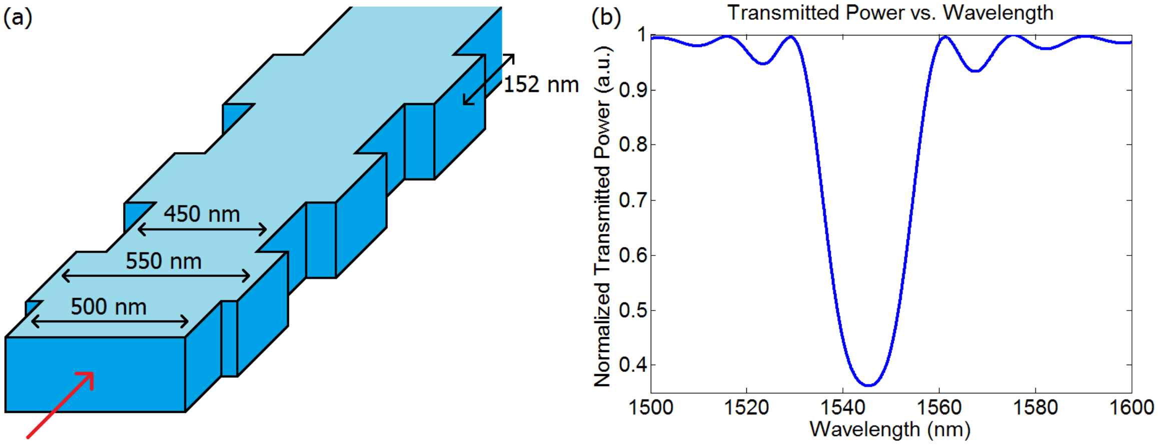

Figure 1.5. (a) Illustration of a Bragg grating in a 250 nm-tall silicon waveguide. (b) Transmission spectrum for a 25 µm-long grating with the specifications given in (a).

1.5: Interferometers and Resonators

In the field of integrated optics, a vast majority of electro-optic modulators rely on either a Mach-Zehnder interferometer [34], a ring resonator [13], or a Bragg resonator configuration. This is because, in any of the three cases, the optical power transmitted through the device is highly dependent on the refractive index of the guided modes of the constituent waveguides, as well as the optical wavelength. This allows small perturbations to the effective index to lead to large changes in the transmitted power, reducing the energy required to encode data from the electrical domain into the optical domain. Ring resonators and Bragg resonators find additional use in wavemixing applications because they increase the modal amplitude, consequently improving the conversion efficiency for adiabatic processes [42,43]. Here we will explain the operation of each of these important device topologies, paving the way for the theoretical and experimental analyses of nonlinear silicon waveguides which will be presented in subsequent chapters.

1.5.1: Mach-Zehnder Interferometers

Mach-Zehnder interferometers are relatively straightforward device components in which the power of an input waveguide is split into two separate arms. These arms are recombined some distance later, and the differences in phase between the optical wave fronts they contain lead to an interference which translates to changes in the transmitted power. Below, Fig. 1.6 illustrates the basic layout of a Mach-Zehnder interferometer, in which codirectional couplers have been employed to redistribute the power propagating within the two input waveguides.

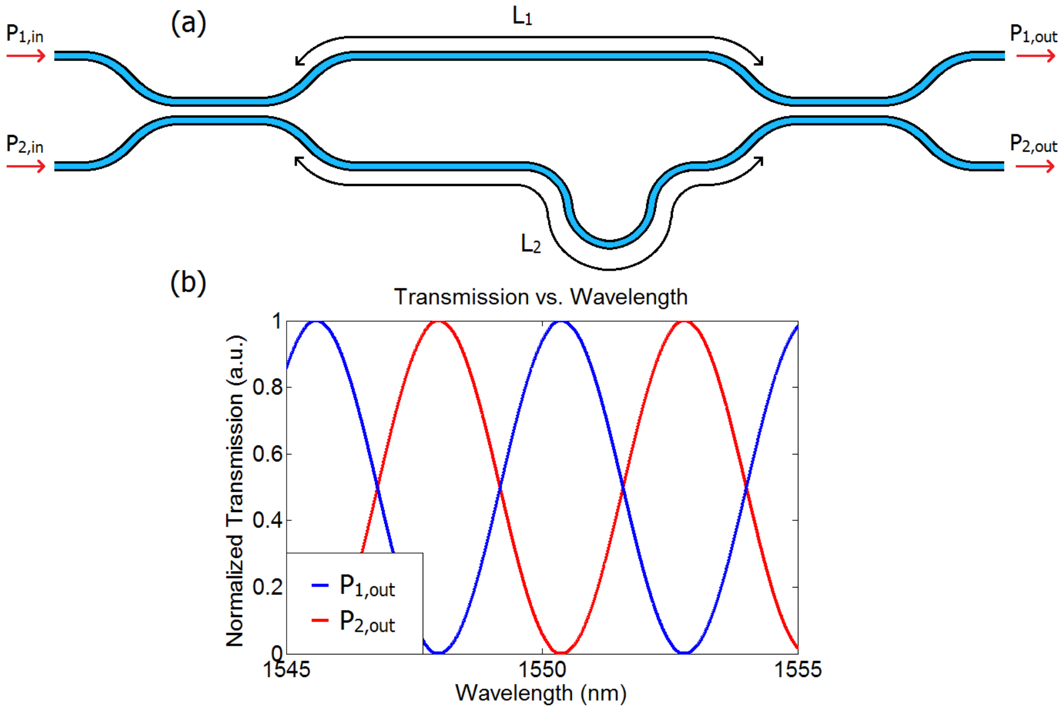

Figure 1.6. (a) Schematic of a waveguide Mach-Zehnder interferometer employing two codirectional couplers. (b) Transmission spectrum of the interferometer, assuming L_1=400 μm, L_2=600 μm, a 50% splitting ratio for both couplers, and $P_{out,2}$=0 W.

The transfer matrix for a symmetric codirectional coupler may be found, through a treatment similar to that provided in Chapter 1.1, to be [44]:

$$\begin{bmatrix} E_{1,o} \\ E_{2,o} \end{bmatrix} = \begin{bmatrix} \cos(\kappa L_c) & i\sin(\kappa L_c) \\ i\sin(\kappa L_c) & \cos(\kappa L_c) \end{bmatrix} \begin{bmatrix} E_{1,i} \\ E_{2,i} \end{bmatrix} \tag{1.30}$$

where κ is the coupling coefficient between the two waveguides and L_c is the length over which they are coupled. For the two arms of the interferometer, the transfer matrix is given as:

$$\begin{bmatrix} E_{1,o} \\ E_{2,o} \end{bmatrix} = \begin{bmatrix} e^{\frac{-j2\pi n_{eff} L_1}{\lambda}} & 0 \\ 0 & e^{\frac{-j2\pi n_{eff} L_2}{\lambda}} \end{bmatrix} \begin{bmatrix} E_{1,i} \\ E_{2,i} \end{bmatrix} \tag{1.31}$$

The transfer matrix of the second codirectional coupler is the same as that of the first. Taking the product of these three transfer matrices, making the important assumption that the codirectional couplers are 3 dB couplers, we define the transfer matrix of the total system as:

$$\begin{bmatrix} E_{1,out} \\ E_{2,out} \end{bmatrix} = \left(\frac{1}{2}\right) \begin{bmatrix} e^{\frac{-j2\pi n_{eff} L_1}{\lambda}} - e^{\frac{-j2\pi n_{eff} L_2}{\lambda}} & i\left(e^{\frac{-j2\pi n_{eff} L_1}{\lambda}} + e^{\frac{-j2\pi n_{eff} L_2}{\lambda}}\right) \\ i\left(e^{\frac{-j2\pi n_{eff} L_1}{\lambda}} + e^{\frac{-j2\pi n_{eff} L_2}{\lambda}}\right) & e^{\frac{-j2\pi n_{eff} L_2}{\lambda}} - e^{\frac{-j2\pi n_{eff} L_1}{\lambda}} \end{bmatrix} \begin{bmatrix} E_{1,in} \\ E_{2,in} \end{bmatrix} \tag{1.32}$$

Using Eq. 1.32 and assuming that (1) there is no input power in waveguide two (2) L_1=400 µm and L_2=450 µm, and (3) n_{eff}=2.5, we may then generate the transmission spectrum shown in Fig. 1.3b. For a more accurate result, it is additionally necessary to take into consideration the wavelength dispersion of κ and n_{eff}, but for the purposes of this work, the simplified treatment given here is sufficient.

We see from Fig. 1.3b that the transmission spectrum of the interferometer exhibits sharp periodic dips and rises, making it a strong candidate for electro-optic modulation. If we assume several different values of the modal effective index, we may see how the transmission at a single wavelength changes in response to the waveguide's optical properties. This effect is shown in Fig. 1.7, which plots the transmission spectra for several different values of the effective index. It is generally necessary for Mach-Zehnder modulators to be very long, on the scale of 1 mm or more, to have dips in transmission with slopes comparable to those exhibited by resonant cavities.

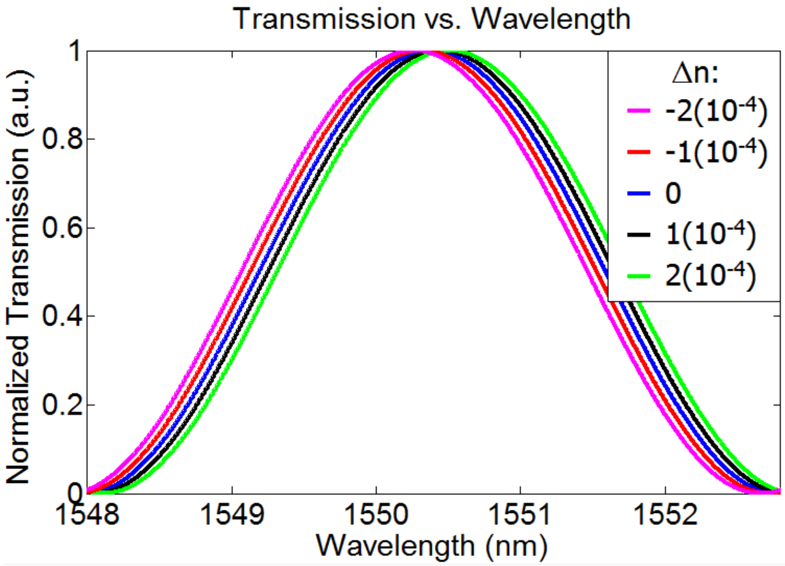

Figure 1.7. Transmission spectra for Mach-Zehnder interferometers with different effective indices.

1.5.2: Ring Resonators

Put simply, a ring resonator is a waveguide made into a closed loop, placed close enough to a second waveguide to exchange energy with it. A schematic of one such device is shown in Fig. 1.8.

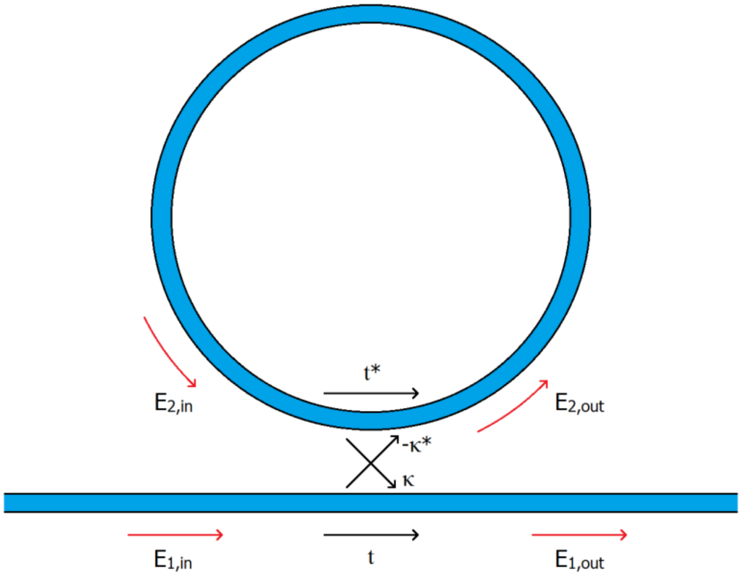

Figure 1.8. A ring resonator coupled to a bus waveguide. The cross- and self-coupling coefficients are labeled along with the input and output electric fields.

A fraction of the light propagating through the straight waveguide, known as the bus, will be transferred to the ring when the two waveguides approach one another, as discussed in the previous chapter. In order to maintain reciprocity and energy conservation, the transfer matrix of the coupling section may be defined as:

$$\begin{bmatrix} E_{1,out} \\ E_{2,out} \end{bmatrix} = \begin{bmatrix} t & \kappa \\ -\kappa^* & t^* \end{bmatrix} \begin{bmatrix} E_{1,in} \\ E_{2,in} \end{bmatrix} \tag{1.33}$$

where κ and t are known as the cross- and self-coupling coefficients, respectively, which are in turn related by:

$$\left|t^2\right|+\left|\kappa^2\right|=1 \tag{1.34}$$

Within the ring, we may assume that the optical mode's amplitude is attenuated by a factor τ, and that it accrues a phase shift θ. In this case, we may relate the field $E_{2,in}$ to the field $E_{2,out}$ as:

$$E_{2,in}=E_{2,out}\tau e^{j\theta} \tag{1.35}$$

where the phase change may in turn be defined as:

$$\theta=\frac{2\pi}{\lambda_0}n_{eff}L \tag{1.36}$$

In this expression, λ_0 is the free-space wavelength, n_{eff} is the effective index, and L is the length of the ring. If we now consider a single propagating wavefront and sum the energy coupling into the bus waveguide from each round-trip within the ring, the transmitted power may be written as:

$$E_{1,out}=t-\kappa^2\tau e^{j\theta}-\kappa^2 t\tau^2 e^{j2\theta}-\kappa^2 t^2\tau^3 e^{j3\theta}-\kappa^2 t^3\tau^4 e^{j4\theta}-\ldots \tag{1.37}$$

or more simply, as:

$$E_{1,out}=t-\kappa^2\tau e^{j\theta}\sum_{n=0}^{\infty}\left(t\tau e^{j\theta}\right)^n \tag{1.38}$$

We have identified an infinite geometric sum in this expression, and through a few lines of algebraic simplification we may arrive at the following expression for the transmitted power:

$$P_{1,out} = P_{1,in}\left[\frac{t^2 - 2t\tau\cos(\theta) + \tau^2}{1 - 2t\tau\cos(\theta) + (t\tau)^2}\right] \tag{1.39}$$

For certain wavelengths, the round-trip phase shift for the ring will be an integer multiple of 2π. When this condition is satisfied, there will be purely destructive interference at the output of the bus waveguide, leading to a sharp drop in the transmitted power and a dissipation of light into the ring's cladding material. This is shown in Fig. 1.9a, which plots the transmitted power as a function of wavelength assuming a ring radius of 40 µm, an effective modal index of 2.5, a t of .95, a κ of .3122, and a τ of .95. Because t and τ are equivalent, there is absolutely no on-resonance transmission, and this condition is known as critical coupling. As these two values become more dissimilar, the minimum transmitted power will increase away from zero.

Fig. 1.9b illustrates how small changes in the effective modal index of the waveguide lead to significant changes in the transmitted power at a single wavelength. The means by which these changes occur will be discussed in greater detail in Chapter 2, but this provides a first look at how electro-optic modulation may occur in ring resonators. Specifically, the change in the resonant wavelength may be related to the change in an optical mode's effective index as [45]:

$$\Delta\lambda_{res} = \lambda_{res}\frac{\Delta n_{eff}}{n_g} \tag{1.40}$$

where λ_{res} is the resonant wavelength and n_g is the group index of the mode, defined in turn as [46]:

$$n_g = n_{eff} - \lambda\frac{dn_{eff}}{d\lambda} \tag{1.41}$$

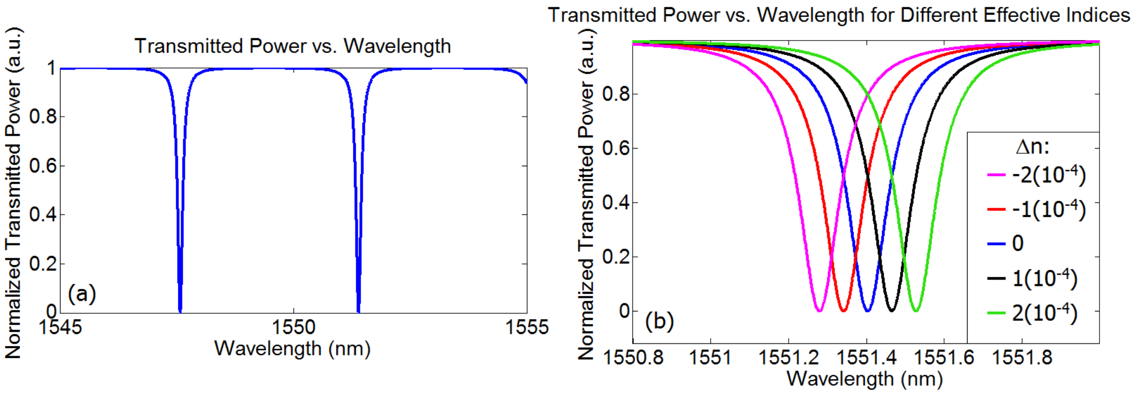

Figure 1.9. (a) The theoretical transmission spectrum of a ring resonator coupled to a bus waveguide. (b) Several different transmission spectra, showing how the resonant wavelength of a ring resonator changes with the effective modal index.

For the purposes of electro-optic modulation, the only other critical factor to consider is the photon lifetime within the ring, which determines the maximum rate at which the transmission may be modulated. This term is defined as [13]:

$$\tau_p = \frac{\lambda_0 Q}{2\pi c} \tag{1.42}$$

where Q is the resonator's quality factor [45]:

$$Q = \frac{\lambda_0}{\Delta\lambda_{3dB}} \tag{1.43}$$

In Eq. 1.43, $\Delta\lambda_{3dB}$ is the 3 dB-bandwidth of the resonance, or the wavelength span over which the transmission through the bus waveguide is less than half of its off-resonance value. In the literature, Q-factors as high as 10^6 have been demonstrated for ring resonators, and values such as these naturally correspond to incredibly low switching energies [47].

In the context of wavemixing, it is also worth noting that the field propagating within the ring resonator may be drastically enhanced at its resonant wavelengths. Revisiting our theoretical treatment from Fig. 1.6, we may write the field leaving the ring's coupling section as:

$$E_{2,out} = -\kappa - \kappa t\tau e^{j\theta} - \kappa t^2\tau^2 e^{j2\theta} - \kappa t^3\tau^3 e^{j3\theta} - \kappa t^4\tau^4 e^{j4\theta} - \ldots \qquad (1.44)$$

Again, we see that there is an infinite geometric sum in this expression, and a similar treatment to that which led to Eq. 1.39 yields the following expression for the modal amplitude within the ring:

$$A_{2,out} = A_{1,in}\sqrt{\frac{1-t^2}{1-2t\tau\cos(\theta)+(t\tau)^2}} \qquad (1.45)$$

This term is plotted for the same ring resonator under consideration in Fig. 1.7, and as Fig. 1.10 clearly shows, the modal amplitude within the ring can be significantly larger the corresponding value at the input of the bus waveguide. This is hugely beneficial in the context of wavemixing, and this effect will be discussed in greater detail in Chapter 2.

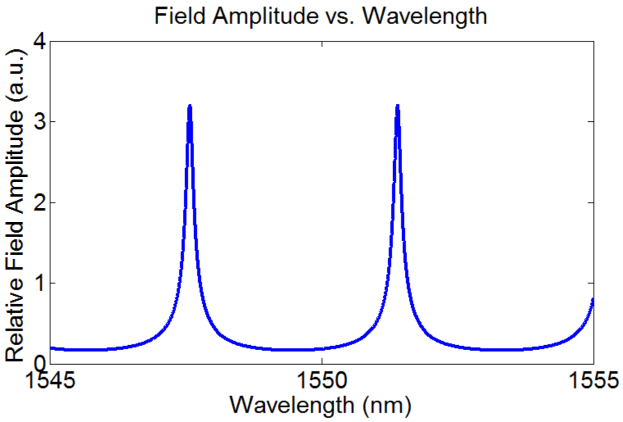

Figure 1.10. Wavelength-dependent field amplitude in a ring resonator, normalized to the input mode amplitude.

For some applications, it is desirable to include a drop port to the ring resonator, as shown in Fig. 1.11a. In this case, a similar analysis to that which produced equations 1.34 through 1.45 yields the following expressions for the power in the through port, the power in the drop port, and the field within the resonator, respectively:

$$P_{1,out} = P_{1,in}\left[\frac{t^2 - 2t^2\tau\cos(\theta) + t^2\tau^2}{1 - 2t^2\tau\cos(\theta) + \left(t^2\tau\right)^2}\right] \tag{1.46}$$

$$P_{drop} = P_{1,in}\left[\frac{\tau\left(1 - t^2\right)^2}{1 - 2t^2\tau\cos(\theta) + \left(t^2\tau\right)^2}\right] \tag{1.47}$$

$$A_{2,out} = A_{1,in}\sqrt{\frac{1 - t^2}{1 - 2t^2\tau\cos\theta + \left(t^2\tau\right)^2}} \tag{1.48}$$

For the same conditions as those considered for the ring resonator without the drop port, these three values are plotted as a function of the optical wavelength in Fig. 1.11b-1.11d.

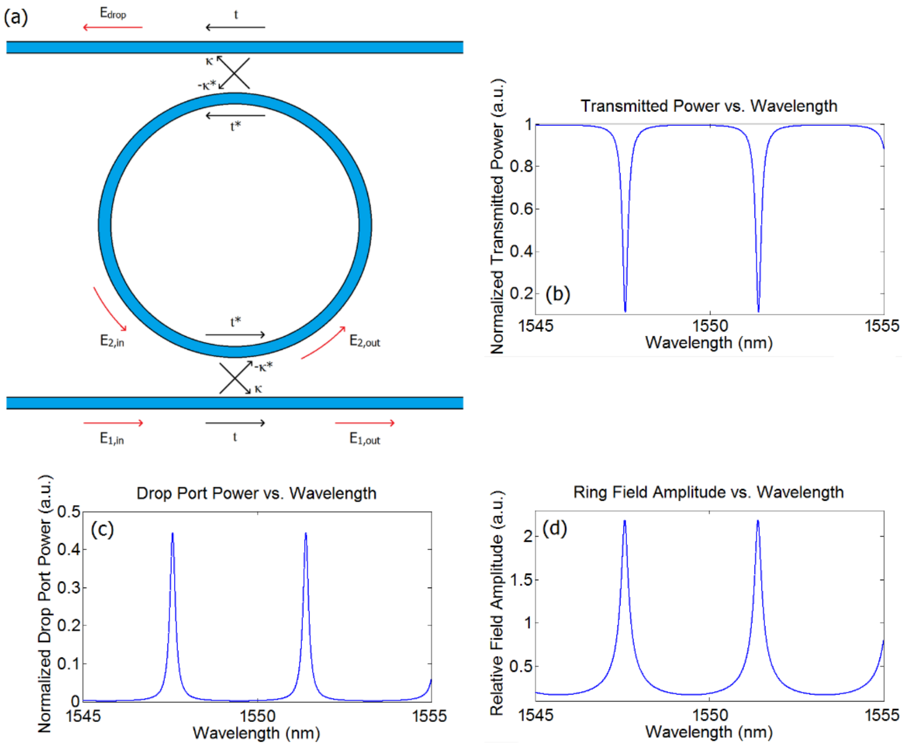

Figure 1.11. (a) Schematic of a ring resonator coupled to both an input waveguide and a drop-port waveguide. (b-c) Wavelength dependence of (a) the power transmitted through the bus waveguide (b) the power coupled into the drop-port, and (c) the modal amplitude within the ring.

Modulation of the effective index has identical effects in ring resonators with and without drop ports, acting in both cases to shift the optical resonances to either shorter or longer wavelengths. However, coupling from the resonator to the drop port generally reduces the Q-factor of a ring by introducing a new source of loss. For the purposes of modulation, drop ports increase the switching voltage and are therefore undesirable.

1.5.3: Bragg Resonators

Similarly to ring resonators, Bragg resonators impose a strong spectral dependence on the power transmitted through a waveguide by folding the optical path over a single area and forcing light to interfere with itself. In Chapter 1.4 we introduced the Bragg grating, also known as the DBR, which couples energy among a waveguide’s modes by introducing periodic perturbations to its cross-section. Bragg gratings may be used to achieve reflection with arbitrarily high extinction ratios, and when two gratings are placed in series within the same waveguide as illustrated in Fig. 1.12a, an optical cavity, or etalon, is created between them. The round-trip path length of the cavity is then 2L, where L is the distance separating the two gratings. Qualitatively, we may consider transmission through this resonator by considering three distinct wavelength regimes.

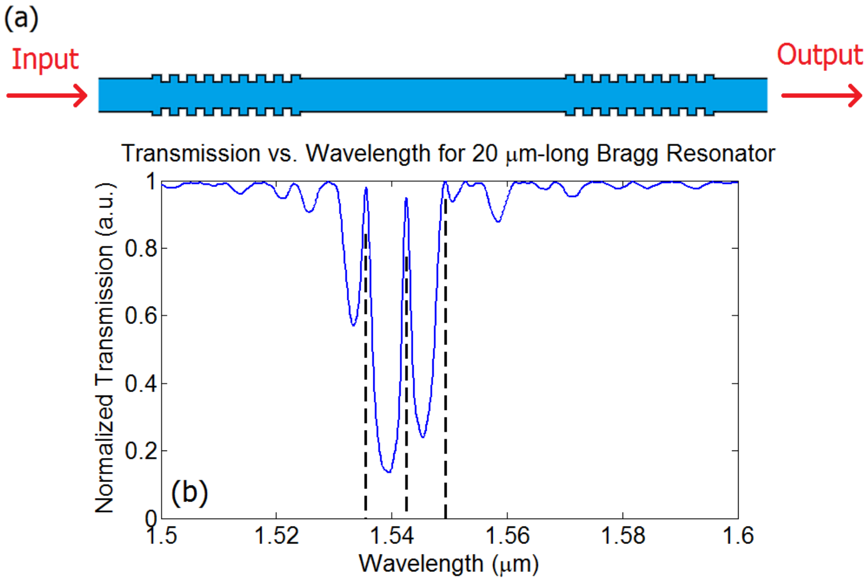

Figure 1.12. (a) Overhead schematic of a Bragg resonator, consisting of two Bragg reflectors and a cavity. (b) Transmission spectrum of a 20 μm-long Bragg resonator, showing three optical resonances within the gratings' stopband (illustrated by dashed vertical lines).

In the first of these, the optical mode's propagation constant does not satisfy the conservation of momentum condition for the gratings. Consequently, the gratings do not interact with the mode, and no reflection occurs. Within the so-called stopband, however, the gratings reflect the optical mode, and we must consider the effects of the cavity between them. For wavelengths at which the round-trip path length of the cavity is an integer number of guided wavelengths, the wavelets escaping from the cavity interfere coherently with one another, leading to high transmission. When this condition is not satisfied, however, the transmitted power reduces drastically and energy is instead reflected into the counter-propagating mode. We can model a Bragg resonator using the finite-difference time-domain software Lumerical, and if we assume two gratings identical to the one considered in Chapter 1.4, as well as a 20 μm cavity length, the resulting transmission spectrum is as shown in Fig. 1.12b.

The free spectral range (FSR) and Q-factor of the cavity's resonances decrease and increase, respectively, as the cavity length is increased, and the Q-factor increases independently of the FSR as the grating length is increased. Bragg gratings are comparable to ring resonators for the purposes of electro-optic modulation, assuming a voltage may be applied across them in an efficient manner, and as we will show in Chapter 3, emerging waveguide designs combined with Bragg resonator topologies show potential for some of the most promising modulation configurations to date.

But before this work can be discussed, the next chapter will begin a more involved discussion of how some of the more fundamental changes to a silicon-based waveguide's supported optical modes may occur. Additionally, special attention will be paid to the potential for second-order wavemixing to occur in silicon and CMOS-compatible waveguides, based on an effect known commonly as electric field-induced second-harmonic generation (EFISH).

Bibliography

1. B. Jalali and S. Fathpour, “Silicon Photonics,” Journal of Lightwave Technology **24**, 4600-4615 (2006).

2. R. Soref and J. Lorenzo, “Single-crystal silicon—A new material for 1.3 and 1.6 μm integrated-optical components,” Electronics Letters **21**, 953-954 (1985).

3. R. Soref and J. Lorenzo, “All-silicon active and passive guided-wave components for λ=1.3 and 1.6 μm,” IEEE Journal of Quantum Electronics **22**, 873-879 (1986).

4. M. Asghari and A. Krishnamoorthy, “Silicon photonics: Energy-efficient communication,” Nature Photonics **5**, 268-270 (2011).

5. M. Antelius, K. Gylfason, and H. Sohlstrom, “An apodized SOI waveguide-to-fiber surface grating coupler for single lithography silicon photonics,” Optics Express **19**, 3592-3598 (2011).

6. Q. Fang, T. Liow, J. Song, C. Tan, M. Yu, G. Lo, and D. Kwong, “Suspended optical fiber-to-waveguide mode size converter for silicon photonics,” Optics Express **18**, 7763-7769 (2010).

7. L. Tong, J. Lou, and E. Mazur, “Single-mode guiding properties of subwavelength-diameter silica and silicon wire waveguides,” Optics Express **12** 1025-1035 (2004).

8. H. Chen, “Low-loss multimode-interference-based crossings for silicon wire waveguides,” IEEE Photonics Technology Letters **18**, 2260-2262 (2006).

9. J. Leuthold, C. Koos, and W. Freude, “Nonlinear silicon photonics,” Nature Photonics **4**, 535-544 (2010).

10. R. Soref, “The past, present, and future of silicon photonics,” IEEE Journal of elected Topics in Quantum Electronics **12**, 1678-1687 (2006).

11. A. Liu, L. Liao, D. Rubin, H. Nguyen, B. Ciftcioglu, Y. Chetrit, N. Izhaky, and M. Paniccia, “High-speed optical modulation based on carrier depletion in a silicon waveguide,” Optics Express **15**, 660-668 (2007).

12. Y. Jiang, W. Jiang, L. Gu, X. Chen, and R. Chen, “80-micron interaction length silicon photonic crystal waveguide modulator,” Applied Physics Letters **87**, 221105 (2005).

13. Q. Xu, B. Schmidt, S. Pradhan, and M. Lipson, “Micrometre-scale silicon electro-optic modulator,” Nature **435**, 325-327 (2005).

14. A. Liu, R. Jones, L. Liao, D. Samara-Rubio, D. Rubin, O. Cohen, R. Nicolaescu, and M. Paniccia, “A high-speed silicon optical modulator based on a metal-oxide-semiconductor capacitor,” Nature **427**, 615-618 (2004).

15. R. Jacobsen, K. Andersen, P. Borel, J. Fage-Pedersen, L. Frandsen, O. Hansen, M. Kristensen, A. Lavrinenko, G. Moulin, H. Ou, C. Peucheret, B. Zsigri, and A. Bjarklv, “Strained silicon as a new electro-optic material,” Nature **441**, 199-202 (2006).

16. B. Chmielak, M. Waldow, C. Matheisen, C. Ripperda, J. Bolten, T. Wahlbrink, M. Nagel, F. Merget, and H. Kurz, “Pockels effect based fully integrated, strained silicon electro-optic modulator,” Optics Express **19**, 17212-17219 (2011).

17. F. Pockels, “On the influence of the electrostatic field on the optical behavior of piezoelectric crystals,” Annals of Physics **273**, 269-305 (1889).

18. S. Azadeh, F. Merget, M. Nezhad, and J. Witzens, “On the Measurement of the Pockels Effect in Strained Silicon,” Optics Letters **40**, 1877-1880 (2015).

19. R. Sharma, M. Puckett, H. Lin, F. Vallini, and Y. Fainman, “Characterizing the effects of free carriers in fully etched, dielectric-clad silicon waveguides,” Applied Physics Letters **106**, 241104 (2015).

20. R. Sharma, M. Puckett, H. Lin, A. Isichenko, F. Vallini, and Y. Fainman, “The effect of dielectric claddings on the electro-optic behavior of silicon waveguides,” Optics Letters **41**, 1185-1188 (2016).

21. R. Carman, R. Chiao, and P. Kelley, “Observation of degenerate stimulated four-photon interaction and four-wave parametric amplification,” Physical Review Letters **17**, 1281-1283 (1966).

22. L. Jia, M. Geng, L. Zhang, L. Yang, P. Chen, T. Wang, Y. Liu, “Wavelength conversion based on degenerate-four-wave-mixing with continuous-wave pumping in silicon nanowire waveguide,” Optics Communications **282**, 1659-1663 (2009).

23. A. Prem, *Study of applications of second harmonic generation*, UT Electronic Theses and Dissertations (2011).

24. M. Cazzanelli, F. Bianco, E. Borga, G. Pucker, M. Ghulinyan, E. Degoli, E. Luppi, V. Veniard, S. Ossicini, D. Modotto, S. Wabnitz, R. Pierobon, and L.

Pavesi, “Second-harmonic generation in silicon waveguides strained by silicon nitride,” Nature Materials **11**, 148-154 (2012).

25. C. Schriever, F. Bianco, M. Cazzanelli, M. Ghulinyan, C. Eisenschmidt, J. de Boor, A. Schmid, J. Heitmann, L. Pavesi, and J. Schilling, “Second-Order Optical Nonlinearity in Silicon Waveguides: Inhomogeneous Stress and Inferfaces,” Advanced Optical Materials **3**, 129-136 (2014).

26. W. Clark, B. El-Kareh, R. Pires, S. Titcomb, and R. Anderson, “Low temperature CMOS-a brief review,” IEEE Transactions on Components, Hybrids, and Manufacturing Technology **15**, 397-404 (1992).

27. K. Buschow, R. Cahn, M. Flemings, B. Ilschner, E. Kramer, S. Mahajan, and P. Veyssiere, *Encyclopedia of Materials: Science and Technology*, Elsevier Science Ltd. (2001).

28. J. Maxwell, “A Dynamical Theory of the Electromagnetic Field,” Proceedings of the Royal Society of London **13**, 1863-1864 (1863).

29. COMSOL, Inc., http://www.comsol.com

30. A. Yariv, “On the Coupling Coefficients in the ‘Coupled-Mode’ Theory,” Proceedings of the IRE **46**, 1956-1957 (1958).

31. A. Yariv, “Coupled-Mode Theory for Guided-Wave Optics,” IEEE Journal of Quantum Electronics **9**, 919-933 (1973).

32. W. Shi, X. Wang, W. Zhang, L. Chrostowski, and N. Jaeger, “Contradirectional couplers in silicon-on-insulator rib waveguides,” Optics Letters **36**, 3999-4001 (2011).

33. A. Grieco, B. Slutsky, D. Tan, S. Zamek, M. Nezhad, and Y. Fainman, “Optical bistability in a silicon waveguide distributed Bragg reflector Fabry-Perot resonator,” Journal of Lightwave Technology **30**, 2352-2355 (2012).

34. W. Green, M. Rooks, L. Sekaric, and Y. Vlasov, “Ultra-compact, low RF power, 10 Gb/s silicon Mach-Zehnder modulator,” Optics Express **15**, 17106-17113 (2007).

35. B. Little, J. Foresi, G. Steinmeyer, E. Thoen, S. Chu, H. Haus, E. Ippen, L. Kimmerling, and W. Greene, “Ultra-compact Si-SiO$_2$ microring resonator optical channel dropping filters,” IEEE Photonics Technology Letters **10**, 549-551 (2002).

36. C. Nobriga, G. Hobbs, W. Wadsworth, J. Knight, D. Skryabin, A. Samarelli, M. Sorel, and R. De La Rue, "Supermode dispersion and waveguide-to-slot mode transition in arrays of silicon-on-insulator waveguides," Optics Letters **35**, 3925-3927 (2010).

37. N. Fontaine, C. Doerr, M. Mestre, R. Ryf, P. Winzer, L. Buhl, Y. Sun, X. Jiang, and R. Lingle, "Space-division multiplexing and all-optical MIMO demultiplexing using a photonic integrated circuit," Optical Fiber Communication Conference (2012).

38. A. Fang, B. Koch, R. Jones, E. Lively, D. Liang, Y. Kuo, and J. Bowers, "A distributed Bragg reflector silicon evanescent laser," IEEE Photonics Technology Letters **20**, 1667-1669 (2008).

39. A. Barybin and V. Dmitriev, *Modern Electrodynamics and Coupled-Mode Theory: Application to Guided-Wave Optics*, Rinton Pr. Inc. (2002).

40. T. Murphy, J. Hastings, and H. Smith, "Fabrication and characterization of narrow-band Bragg-reflection filters in silicon-on-insulator ridge waveguides," Journal of Lightwave Technology **19**, 1938-1942 (2001).

41. Lumerical Solutions, Inc. http://www.lumerical.com/tcad-products/fdtd/

42. J. Levy, M. Foster, A. Gaeta, and M. Lipson, "Harmonic generation in silicon nitride ring resonators," Optics Express **19**, 11415-11421 (2011).

43. W. Pernice, C. Xiong, C. Schuck, and H. Tang, "Second harmonic generation in phase matched aluminum nitride waveguides and micro-ring resonators," Applied Physics Letters **100**, 223501 (2012).

44. W. Huang and J. Hong, "A transfer matrix approach based on local normal modes for coupled waveguides with periodic perturbations," Journal of Lightwave Technology **10**, 1367-1375 (1992).

45. W. Bogaerts, P. De Heyn, T. Van Vaerenbergh, K. De Vos, S. Kumar, Selvaraja, T. Claes, P. Dumon, P. Bienstman, D. Van Thourhout and R. Baets, "Silicon microring resonators," Laser and Photonics Reviews **6**, 47-73 (2012).

46. E. Dulkeith, F. Xia, L. Schares, W. Green, and Y. Vlasov, "Group index and group velocity dispersion in silicon-on-insulator photonic wires," Optics Express **14**, 3853-3863 (2006).

47. K. Luke, A. Dutt, C. Poitras, and M. Lipson, "Overcoming Si_3N_4 film stress limitation for high quality factor ring resonators," Optics Express **21**, 22829-22833 (2013).

Chapter 2:

Nonlinear and Electro-Optic Effects

In this chapter we will discuss three optical effects which are of particular interest for telecommunications applications. Two of these, the Pockels effect and second-harmonic generation, are based on second-order optical nonlinearities, whereas the third, free-carrier plasma dispersion, is a result of the free charge carriers present in semiconductors.

Both the Pockels effect and the free-carrier plasma dispersion effect result in changes in the real part of a material's refractive index, making them appealing for electro-optic modulation, but because both effects are present to some degree in noncentrosymmetric semiconductors, it can be challenging to experimentally disentangle the two. In previous work, researchers have attempted to characterize the Pockels effect in strained silicon waveguides while neglecting the free-carrier effect [1-3], but this is now known to have led to significant inaccuracies in the reported nonlinear coefficients. More recent research has confirmed that, even in semiconductor waveguides which do possess second-order nonlinear coefficients, electric field screening disables modulation based on these coefficients. As this chapter will show, it is now apparent that free-carrier plasma dispersion is the dominant effect in the electro-optic behavior of semiconductor waveguides.

Second-harmonic generation, an effect not immediately relevant to electro-optic modulation, is an additional second-order nonlinear effect which allows for wavelength multiplexing in telecommunications applications. The effect, which will be explained, couples energy among different wavelengths of light, potentially allowing for data to be replicated at different carrier wavelengths. Because second-order effects such as the Pockels effect and second-harmonic generation often go hand in hand, it is straightforward to extend our analysis of semiconductor waveguides beyond modulation, additionally considering the potential for nonlinear wavemixing in the same or similar structures.

2.1: The Pockels Effect

As discussed in Chapter 1.2, waveguide configurations which exhibit sharp spectral dips in transmission may be utilized to achieve electro-optic modulation, but this is only true of the material used to guide the optical mode possesses certain desirable characteristics. Here we will consider the Pockels effect, which occurs in materials possessing nonzero second-order nonlinear coefficients, defined commonly by the 3x3x3 $\chi^{(2)}$ tensor.

In general, the second-order polarization resulting from an electric field in a nonlinear material may be written as [4]:

$$P_i^{(2)} = \varepsilon_0 \sum_{j,k} \chi_{ijk}^{(2)} E_j E_k \tag{2.1}$$

where $\chi^{(2)}{}_{ijk}$ is the ijkth component of the material's $\chi^{(2)}$ tensor, and E_j and E_k are the j and k components of the generalized electric field within the material, respectively. For simplicity's sake, let us assume that the electromagnetic field propagating through the material only possesses a component along the x-direction. If we now define a DC bias field applied in second direction, taken here to by the y-direction, the second order polarization may be written fully as:

$$\begin{bmatrix} P_x^{(2)} \\ P_y^{(2)} \\ P_z^{(2)} \end{bmatrix} = \varepsilon_0 \begin{bmatrix} \chi_{xxy}^{(2)} E_{x,opt} E_{y,DC} \\ \chi_{yxy}^{(2)} E_{x,opt} E_{y,DC} \\ \chi_{zxy}^{(2)} E_{x,opt} E_{y,DC} \end{bmatrix} \tag{2.2}$$

Then, by including the nonlinear polarization as a modification to Eq. 1.5, we obtain the following relation defining the material's permittivity:

$$D = \varepsilon E = \varepsilon_o \varepsilon_r E + P^{(2)} \tag{2.3}$$

Assuming the material is isotropic and lossless, we may expand Eq. 2.3 into matrix form as:

$$\begin{bmatrix} \varepsilon_{xx} & \varepsilon_{xy} & \varepsilon_{xz} \\ \varepsilon_{yx} & \varepsilon_{yy} & \varepsilon_{yz} \\ \varepsilon_{zx} & \varepsilon_{zy} & \varepsilon_{zz} \end{bmatrix} \begin{bmatrix} E_x \\ E_y \\ E_z \end{bmatrix} = \varepsilon_o \begin{bmatrix} \varepsilon_r & 0 & 0 \\ 0 & \varepsilon_r & 0 \\ 0 & 0 & \varepsilon_r \end{bmatrix} \begin{bmatrix} E_x \\ E_y \\ E_z \end{bmatrix} + \varepsilon_o \begin{bmatrix} 2\chi^{(2)}_{xxy} E_x E_y \\ 2\chi^{(2)}_{yxy} E_x E_y \\ 2\chi^{(2)}_{zxy} E_x E_y \end{bmatrix} \tag{2.4}$$

Looking more closely at the x-component of this equation, and more completely specifying our electric field components, we have:

$$\varepsilon_{xx} E_{x,opt} + \varepsilon_{xy} E_{y,DC} = \varepsilon_o \varepsilon_r \left(E_{x,opt} + E_{y,DC} \right) + 2\varepsilon_o \chi^{(2)}_{xxy} E_{x,opt} E_{y,DC} \tag{2.5}$$

and considering only the components of Eq. 2.5 which vary at the optical frequency, this becomes:

$$\varepsilon_{xx} E_{x,opt} = \varepsilon_o \left(\varepsilon_r + 2\chi^{(2)}_{xxy} E_{y,DC} \right) E_{x,opt} \tag{2.6}$$

It is immediately apparent from Eq. 2.6 that the material's second-order polarization has in this case led to a change in the value of $\varepsilon_{r,x}$, the x-component of the material's relative permittivity tensor. Through a few steps of algebra, we may further express the change in the x-component of the material's index of refraction as:

$$\Delta n_x = \frac{\chi^{(2)}_{xxy} E_{y,DC}}{n_x} \tag{2.7}$$

This important phenomenon, known commonly as the Pockels effect, shows how materials with second-order nonlinearities may be used to modulate the flow of light in integrated waveguides. By applying properly oriented bias voltages across either interferometric or resonant structures such as those discussed in Chapter 1.4, the optical power transmitted through a waveguide may be modulated via a change in the refractive index.

2.1.1: The Implications of Symmetry

In the context of silicon, however, there are two distinct problems which prevent the Pockels effect from occurring. First, let us consider inversion symmetry, an important property in determining whether or not a material will be suitable for electro-optic modulation. If a material is said to possess inversion symmetry, it may be inverted about the x-, y-, and z-axes, taking some point as the origin, without changing the positions of its constituent atoms. This concept is illustrated conceptually in Fig. 2.1.

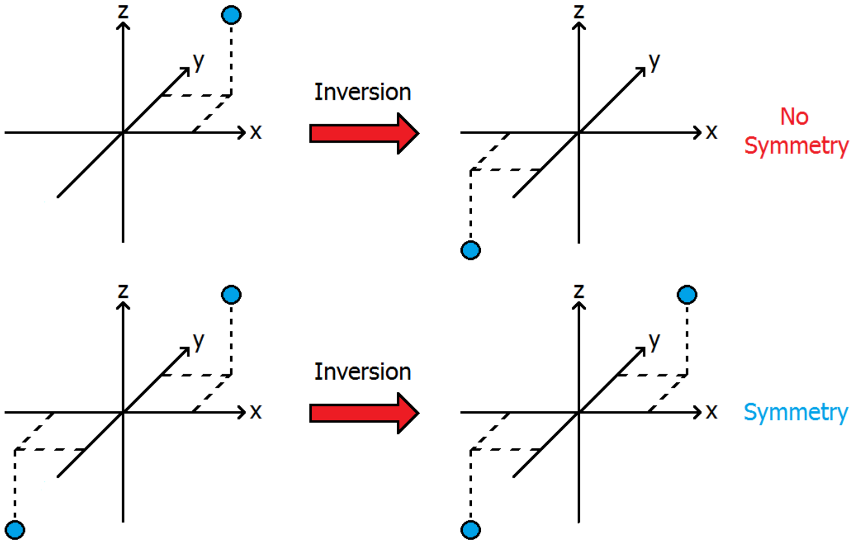

Figure 2.1. Conceptual illustration highlighting the fundamental difference between non-centrosymmetric (top) and centrosymmetric (bottom) materials. The blue circles represent atoms.

The transformation matrix corresponding to the inversion may be written as:

$$M = \begin{bmatrix} -1 & 0 & 0 \\ 0 & -1 & 0 \\ 0 & 0 & -1 \end{bmatrix} \tag{2.2}$$

Let us again consider the second-order polarization arising from an interaction between the material's as-of-yet undefined $\chi^{(2)}$ tensor and a generalized electric field, defined in Eq. 2.1. By explicitly writing out the summation, as opposed to the performing the more simplified treatment done previously, we may write the total second-order polarization as:

$$\begin{bmatrix} P_x^{(2)} \\ P_y^{(2)} \\ P_z^{(2)} \end{bmatrix} = \varepsilon_0 \begin{bmatrix} \chi_{xxx}^{(2)} E_x{}^2 + \chi_{xyy}^{(2)} E_y{}^2 + \chi_{xzz}^{(2)} E_z{}^2 + 2\chi_{xxy}^{(2)} E_x E_y + 2\chi_{xxz}^{(2)} E_x E_z + 2\chi_{xyz}^{(2)} E_y E_z \\ \chi_{yxx}^{(2)} E_x{}^2 + \chi_{yyy}^{(2)} E_y{}^2 + \chi_{yzz}^{(2)} E_z{}^2 + 2\chi_{yxy}^{(2)} E_x E_y + 2\chi_{yxz}^{(2)} E_x E_z + 2\chi_{yyz}^{(2)} E_y E_z \\ \chi_{zxx}^{(2)} E_x{}^2 + \chi_{zyy}^{(2)} E_y{}^2 + \chi_{zzz}^{(2)} E_z{}^2 + 2\chi_{zxy}^{(2)} E_x E_y + 2\chi_{zxz}^{(2)} E_x E_z + 2\chi_{zyz}^{(2)} E_y E_z \end{bmatrix} \tag{2.3}$$

If we now assume that the material under consideration is invariant under the inversion transformation, we may alternatively represent the electric fields in the transformed coordinate system while leaving the $\chi^{(2)}$ tensor unchanged, perform the summation to obtain the second-order polarization in the transformed coordinate system, and transform the result back to the original coordinate system. The result, by definition, should be equivalent to Eq. 2.3. This second representation of the second-order polarization may be written as:

$$P_i^{(2)} = \varepsilon_0 \sum_i M_{i,l}^{-1} \sum_{m,n} \left[\chi_{lmn}^{(2)} \left(\sum_p M_{m,p} E_p \right) \left(\sum_q M_{n,q} E_q \right) \right] \tag{2.4}$$

In vector form this becomes:

$$\begin{bmatrix} P_x^{(2)} \\ P_y^{(2)} \\ P_z^{(2)} \end{bmatrix} = \varepsilon_0 \begin{bmatrix} -\chi_{xxx}^{(2)} E_x{}^2 - \chi_{xyy}^{(2)} E_y{}^2 - \chi_{xzz}^{(2)} E_z{}^2 - 2\chi_{xxy}^{(2)} E_x E_y - 2\chi_{xxz}^{(2)} E_x E_z - 2\chi_{xyz}^{(2)} E_y E_z \\ -\chi_{yxx}^{(2)} E_x{}^2 - \chi_{yyy}^{(2)} E_y{}^2 - \chi_{yzz}^{(2)} E_z{}^2 + 2\chi_{yxy}^{(2)} E_x E_y - 2\chi_{yxz}^{(2)} E_x E_z - 2\chi_{yyz}^{(2)} E_y E_z \\ -\chi_{zxx}^{(2)} E_x{}^2 - \chi_{zyy}^{(2)} E_y{}^2 - \chi_{zzz}^{(2)} E_z{}^2 + 2\chi_{zxy}^{(2)} E_x E_y - 2\chi_{zxz}^{(2)} E_x E_z - 2\chi_{zyz}^{(2)} E_y E_z \end{bmatrix} \tag{2.5}$$

However, we can now see that this second expression, which has just been stated to be equivalent to the one given in Eq. 2.3, is in fact the negative of it. In order for the two terms to be equivalent, every element of the second-order polarization must be zero, and consequently, so too must every element of the $\chi^{(2)}$ tensor equal zero. What we have just shown, put simply, is that centrosymmetric materials, which possess inversion symmetry, intrinsically lack second-order nonlinearities. Silicon possesses the diamond lattice illustrated in Fig. 2.2, which does exhibit centrosymmetry, and because of this, the Pockels effect cannot occur in silicon.

Over the past decade, however, a significant amount of research has been done in the field of integrated silicon photonics exploring the possibility to deform silicon in an asymmetric way, thereby removing its centrosymmetry [1-3]. Theoretically, this is predicted to reduce the number of elements in the $\chi^{(2)}$ tensor which are identically required to equal zero. Consider, for example, the two unit cells of silicon's lattice shown in Fig. 2.2. The unstrained case may be inverted about all three axes, taking the point halfway between any adjacent silicon atoms as the origin, without moving atoms to positions which were not previously occupied by the same atom.

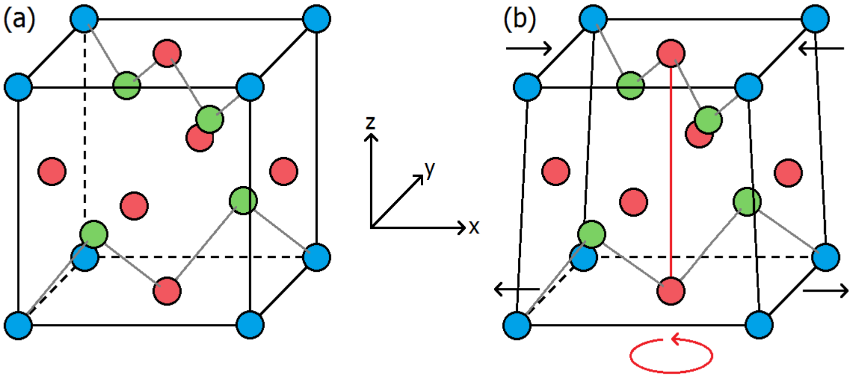

Figure 2.2. Single unit cell of (a) unstrained and (b) strained crystalline silicon. Blue, red, and green circles represent silicon atoms at corners, faces, and the interior of the cell, respectively. Gray lines represent some key Si-Si bonds, for clarity. The directions of strain are indicated by black arrows in (b).

For the strained case, however, this is no longer true. Here, the material's centrosymmetry has been reduced to a weaker, rotational symmetry about the z-axis, as illustrated in Fig. 2.2b by the red vertical line. The transformation matrix corresponding to this new symmetry is given as:

$$M = \begin{bmatrix} -1 & 0 & 0 \\ 0 & -1 & 0 \\ 0 & 0 & 1 \end{bmatrix} \tag{2.6}$$

If we now represent the second-order polarization using Eq. 2.6 in place of Eq. 2.2, we may write it as:

$$\begin{bmatrix} P_x^{(2)} \\ P_y^{(2)} \\ P_z^{(2)} \end{bmatrix} = \varepsilon_0 \begin{bmatrix} -\chi_{xxx}^{(2)} E_x{}^2 - \chi_{xyy}^{(2)} E_y{}^2 - \chi_{xzz}^{(2)} E_z{}^2 - 2\chi_{xxy}^{(2)} E_x E_y + 2\chi_{xxz}^{(2)} E_x E_z + 2\chi_{xyz}^{(2)} E_y E_z \\ -\chi_{yxx}^{(2)} E_x{}^2 - \chi_{yyy}^{(2)} E_y{}^2 - \chi_{yzz}^{(2)} E_z{}^2 - 2\chi_{yxy}^{(2)} E_x E_y + 2\chi_{yxz}^{(2)} E_x E_z + 2\chi_{yyz}^{(2)} E_y E_z \\ +\chi_{zxx}^{(2)} E_x{}^2 + \chi_{zyy}^{(2)} E_y{}^2 + \chi_{zzz}^{(2)} E_z{}^2 + 2\chi_{zxy}^{(2)} E_x E_y - 2\chi_{zxz}^{(2)} E_x E_z - 2\chi_{zyz}^{(2)} E_y E_z \end{bmatrix} \tag{2.7}$$

In this case there are four unique components of the $\chi^{(2)}$ tensor, $\chi^{(2)}{}_{\mathrm{xxz}}$, $\chi^{(2)}{}_{\mathrm{yyz}}$, $\chi^{(2)}{}_{\mathrm{xyz}}$, and $\chi^{(2)}{}_{\mathrm{zzz}}$, which are no longer required to equal zero. In coming to this conclusion, we have made use of Kleinman symmetry [4], which states that permuting the indices of a $\chi^{(2)}$ tensor element will not change its value, assuming the value is considered to be a nonresonant one. In other words, deforming silicon generates nonzero second-order nonlinearities within the material, potentially allowing it to exhibit the Pockels effect for electro-optic modulation.

In past work, we have attempted to characterize some of the components of the nonlinear susceptibility tensor by applying vertical bias voltages across waveguides composed of strained silicon [5]. Fig. 2.3a shows an SEM image of the edge of a silicon waveguide clad with compressively stressed silicon nitride, fabricated in the CalIT2 cleanroom facility at UCSD. The compressive stress in the nitride causes it to expend, and although the bottom of the silicon waveguide is fixed in place by the silicon dioxide substrate, the top of the waveguide expands along with the nitride layer, leading to a vertical gradient of horizontal stress within the waveguide. Fig. 2.3b plots the simulated horizontal strain, generated in Comsol, across the device.

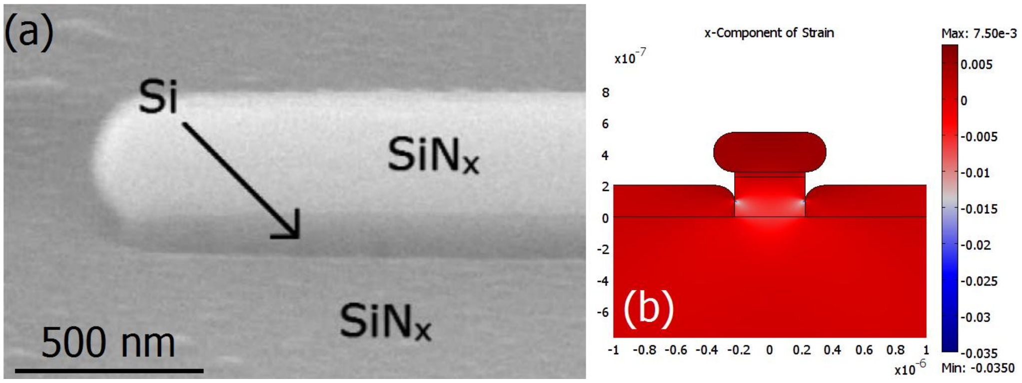

Figure 2.3. (a) SEM image of the edge of a silicon waveguide clad with 150 nm of compressively stressed silicon nitride. (b) Horizontal component of strain induced in the silicon waveguide, assuming a value of stress in the nitride layer of -1.7 GPa.

In order to measure the electro-optic effect generated by the applied voltages, we fabricated Bragg resonators, as discussed in Chapter 1.5.3. The resonators' reflectors were Bragg gratings consisting of 70 modulation periods, and the resonant cavities were 100 μm in length. The passive transmission of the TE- and TM-like modes across two different resonators, with respective grating periods of 312 and 376 nm, are shown in Fig. 2.4a. We observed the change in resonant wavelength for the two guided mode, as shown in Fig. 2.4b, and by relating our results to a change in the waveguide's effective modal indices, we were able to extract the effective nonlinear susceptibility components $\chi^{(2)}_{xxy}$=-74 pm/V and $\chi^{(2)}_{yyy}$=188 pm/V.

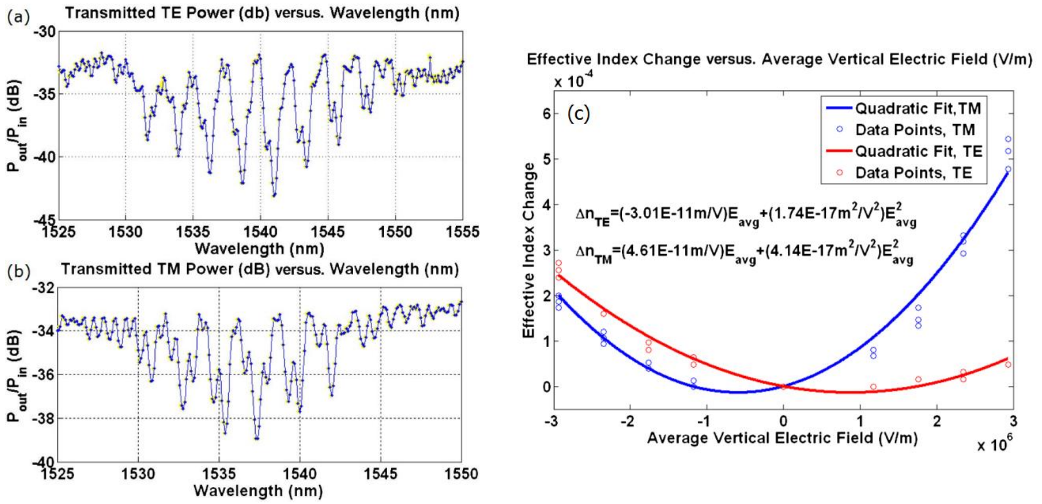

Figure 2.4. (a,b) Measured transmission spectra of the (a) TE- and (b) TM-like modes across Bragg resonators with modulation periods of (a) 312 and (b) 376 nm. (c) Measured electro optic-behavior of the TE- (red) and TM-like modes, showing both quadratic and linear components.

The measured second-order nonlinearities of strained silicon waveguides have been steadily increasing, recently reaching values as high as 330 pm/V [6]. Fig. 2.5 plots the progress made in the field as a function of time, illustrating this development. Until very recently, it seemed as if strained silicon would be a promising platform for electro-optic modulation based on the Pockels effect. However, as will be discussed in the next subsection, there is an additional effect arising from silicon’s nonzero conductivity which may have served as a complicating variable in the work done to date.

2.1.2: Electric Field Screening in Semiconductors

Silicon is a semiconductor, which means that it has a conductivity between those of either insulators or metals, and because of this, electric fields applied across silicon do not simply penetrate into the material, and are instead screened out by the displacement of holes and electrons typical to semiconductor-dielectric interfaces [7]. In the majority of the work done involving strained silicon, however, this important material property was not taken into consideration when extracting the material's second-order nonlinear coefficient. More recently, new work has more clearly shown how capacitive free-carrier effects impact the properties of semiconductor waveguides [8- 11]. In this section, we highlight how difficult it really is to perform electro-optic modulation based on the Pockels effect in semiconductor waveguides.

As an example, let us again consider a silicon waveguide which is 500 nm-tall, 250 nm-wide, and clad with 1 μm of silicon dioxide. Furthermore, let us assume that the silicon is slightly p-type, with a boron dopant concentration of 10^{15} cm^{-3}. A voltage may be applied vertically across the sample by depositing a metal, say aluminum, on top of the cladding layer, then touching electrical probe tips to both this top electrode and the silicon handle. This scheme is illustrated in Fig. 2.5a. Using the semiconductor physics tool Silvaco [12], we may theoretically predict how effectively the bias electric field penetrates into the waveguide. For more accurate simulations it is necessary to take into consideration the fixed charges at the semiconductor-dielectric interfaces, but for the purposes of this demonstration these values may be set to zero. The results, shown in Fig.

2.5b and Fig. 2.5c, confirm the intuitive prediction that the bias electric field does not interact strongly with the core of the waveguide. For voltages of either positive or negative 10 V, the value of the electric field is drastically reduced within the waveguide as opposed to the cladding. Modulation based on the Pockels effect is then clearly difficult to realize in silicon, even if a large strain gradient has been introduced.

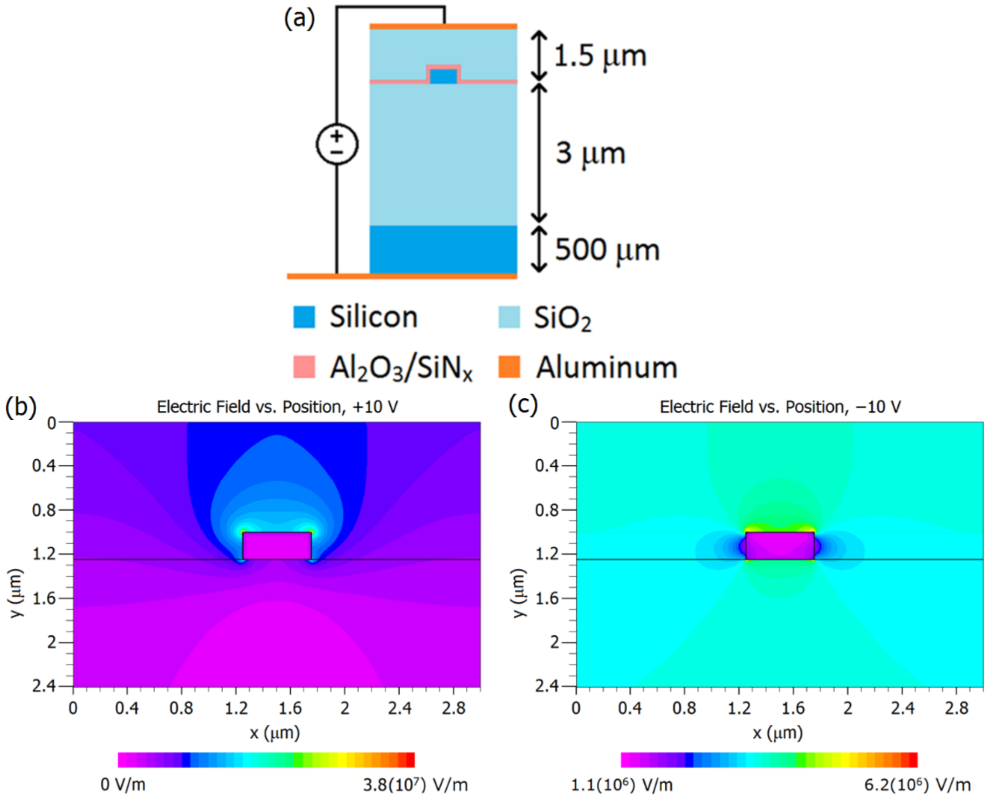

Figure 2.5. Magnitude of the electric field across a silicon waveguide with a p-type doping concentration of 10^{15} cm^{-3}, assuming applied voltages of (a) positive and (b) negative 10V.

For the same waveguide, we may calculate the change in the effective index of the TE-like mode through use of the Soref and Bennett equations, which relate the concentrations of free carriers in silicon to changes in the real and imaginary parts of the material's index of refraction. At an optical wavelength of 1.55 µm, these are given as [13]:

$$\Delta n = -5.4\left(10^{-22}cm^3\right)\Delta N_e^{1.011} - 1.53\left(10^{-18}cm^3\right)\Delta N_h^{.838} \tag{2.8}$$

$$\Delta\alpha = 8.88\left(10^{-21}cm^2\right)\Delta N_e^{1.167} + 5.84\left(10^{-20}cm^2\right)\Delta N_h^{1.109} \tag{2.9}$$

where ΔN_e and ΔN_h are the deviations away from the intrinsic concentrations for electrons and holes, respectively. Using these equations, we may generate maps of the spatially variant refractive index of the waveguide and, again using the finite-difference time-domain solver Lumerical, calculate the effective indices of the waveguide's supported modes for each of the applied voltages under consideration. This analysis will be performed for more physically realistic waveguide geometries in Chapter 2.3.

2.2: Second-Harmonic Generation

Waveguides with second-order optical nonlinearities exhibit unique effects as electromagnetic waves propagate through them. Sum- and difference frequency generation are two such effects [4], and second-harmonic generation, the degenerate case of sum-frequency generation, is perhaps the most readily understood of these. If we assume that a TM-like mode propagates along a waveguide composed of a second-order nonlinear material at some fundamental frequency ω, the y-component of the second-order polarization within the waveguide may be written as:

$$P_{yyy}^{(2)}(x,y,z,t)=\varepsilon_0\chi_{yyy}^{(2)}\left(\mathrm{Re}\left\{E_y(x,y)e^{-j(\beta z+\omega t)}\right\}\right)^2 \tag{2.10}$$

This term, proportional to the square of the propagating electric field, contains terms at frequencies of 0 and 2ω, and the magnitude of the latter is given as:

$$P_{yyy,2\omega}^{(2)}(x,y,z)=\frac{\varepsilon_0}{2}\chi_{yyy}^{(2)}E_y(x,y)^2e^{-j2\beta z} \tag{2.11}$$

If we now include this polarization as a perturbation to the normal modes of the waveguide as in Chapter 1.3, we may solve for the spatial evolution of both the pump mode and a second TM-like mode at twice the fundamental frequency as:

$$\frac{dA^{\omega}}{dz}=-j\kappa^{*}A^{\omega}\left(z\right)^{*}A^{2\omega}\left(z\right)e^{-j2\Delta z} \tag{2.12}$$

$$\frac{dA^{2\omega}}{dz}=-j\kappa A^{\omega}\left(z\right)^{2}e^{j2\Delta z} \tag{2.13}$$

where κ is the nonlinear coupling coefficient between the two modes, defined as:

$$\kappa = \frac{\omega\varepsilon_0}{4}\iint E^{2\omega}(x,y)^* \chi^{(2)}_{yyy}(x,y)\, E^{\omega}(x,y)^2\, dxdy \tag{2.14}$$

and Δ is the phase mismatch, given by:

$$\Delta = \frac{\beta^{2\omega} - 2\beta^{\omega}}{2} \tag{2.15}$$

Finally, the expression for the second-harmonic power, as a function of length, may be written as:

$$P^{2\omega} = \left(\kappa P^{\omega} z \exp\left(j\Delta\mathrm{z}\right)\frac{\sin\left(\Delta\mathrm{z}\right)}{\Delta z}\right)^2 \tag{2.16}$$

In these expressions, the phase mismatch is arguably the most important term in determining what fraction of the pump mode’s power couples into the second-harmonic. If the phase mismatch is nonzero, locally generated second-harmonic wavelets will be dephased from each other and superimpose destructively, leading to a sinusoidal dependence of the second-harmonic signal to the propagation length. However, if the phase mismatch is somehow set to zero, the second-harmonic wavelets will superimpose constructively, leading to a coherent transfer of energy from the pump to the second-harmonic wavelength. Fig. 2.6 illustrates this effect, plotting the normalized second-harmonic power as a function of length for different phase mismatches, assuming that the pump mode is not depleted and is taken to be constant.

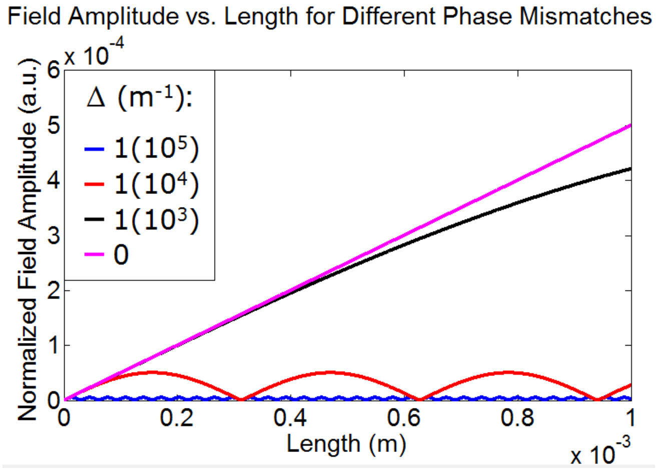

Figure 2.6. Normalized second-harmonic field amplitude, as a function of the propagation length within a waveguide composed of a nonlinear material, for different phase mismatches between the pump and second-harmonic modes.

Whereas the semiconducting nature of silicon is problematic in the context of electro-optic modulation based on the Pockels effect, it does not come directly into play when considering second-harmonic generation. As a result, strained silicon may very well present a viable platform for this effect, and second-harmonic generation has in fact been demonstrated in silicon waveguides deformed by silicon nitride in the literature [14]. It has been predicted, however, that a fraction of the observed effect may be due to electric field-induced second-harmonic generation (EFISH), an effect in which a static electric field allows a third-order optical nonlinearity to act as a second-order one. For example, let us assume that a TM-like mode propagates along a waveguide composed of a third-order material such as silicon, across which a vertical bias voltage has been applied. The vertical component of the third-order polarization may then be written as:

$$P_y^{(3)}\left(x,y,z,t\right)=\varepsilon_o\chi_{yyyy}^{(3)}\left(\mathrm{Re}\left\{E_y\left(x,y\right)e^{j(\omega t-\beta z)}\right\}\right)^2 E_{y,DC}\left(x,y\right) \tag{2.17}$$

where $\chi^{(3)}_{yyyy}$ is the all-vertical component of the material's third-order nonlinear susceptibility, and $E_{y,DC}$ is the bias electric field. It is clear from Eq. 2.16 that the third-order polarization will then have frequency components at both 0 and 2ω, similarly to Eq. 2.10, and may likewise couple energy from the pump mode to thee second-harmonic. In this case, the effective second-order nonlinear susceptibility may be written as:

$$\chi^{(2)}_{eff,yyy} = E_{y,DC}\chi^{(3)}_{yyyy} \tag{2.18}$$

Even without an applied voltage, a static electric field may exist within a waveguide due to fixed charges at interfaces between two media [7]. In silicon, for example, interfaces with silicon nitride have been found to possess values of fixed charge as high as $3(10^{12})$ C/cm^2, leading to large built-in electric fields, and this has been shown to contribute strongly to the second-harmonic generation measured in strained silicon waveguides [15]. It is then desirable to determine which of the potential effects discussed here, strain-induced symmetry breaking or EFISH, is the more promising candidate for high conversion efficiency second-harmonic generation in silicon-based waveguides. To this end, new waveguide topologies with favorable characteristics will be introduced and theoretically and experimentally characterized in Chapter 4.

2.3: Free-Carrier Plasma Dispersion

As mentioned in Chapter 2.1.2, the semiconducting nature of silicon creates a serious obstacle in the effort to modulate the material's refractive index through the Pockels effect. However, this same characteristic may be used to achieve modulation through a separate phenomenon known as the free-carrier plasma dispersion effect, and many silicon modulators based on this have been reported on in the literature to date [16-21]. Deviations in the concentration of holes and electrons away from their intrinsic values in silicon, $1.5(10^{10})\ \mathrm{cm}^{-3}$ [4], lead to changes in both the real and imaginary parts of the material's refractive index, as quantified by the Soref and Bennet equations given in Eq. 2.8 and 2.9 for an optical wavelength of 1.55 µm.

Although the majority of work in the literature involving free-carrier plasma dispersion has generated the effect by driving a current through continuous layers of silicon, the effect may also be realized in capacitive structures in which the anode and cathode are separated by one or more layers of insulating material [22-24]. In this second configuration, it becomes critical to take into consideration the values of fixed charges present at the different boundaries of the semiconductor waveguide, as these have a large impact on the electro-optic behavior of the device. As an example, let us consider a silicon waveguide clad with a thin layer of either silicon nitride or aluminum oxide, followed by a thick silicon dioxide cladding. Whereas the former possesses a large positive fixed charge along its interface with silicon, driving the p-type semiconductor into depletion, the aluminum oxide has a negative fixed charge, increasing the concentration of holes in silicon near the interface between the two materials. This effect is illustrated in Fig. 2.7, which shows electron concentrations for models generated again through Silvaco.

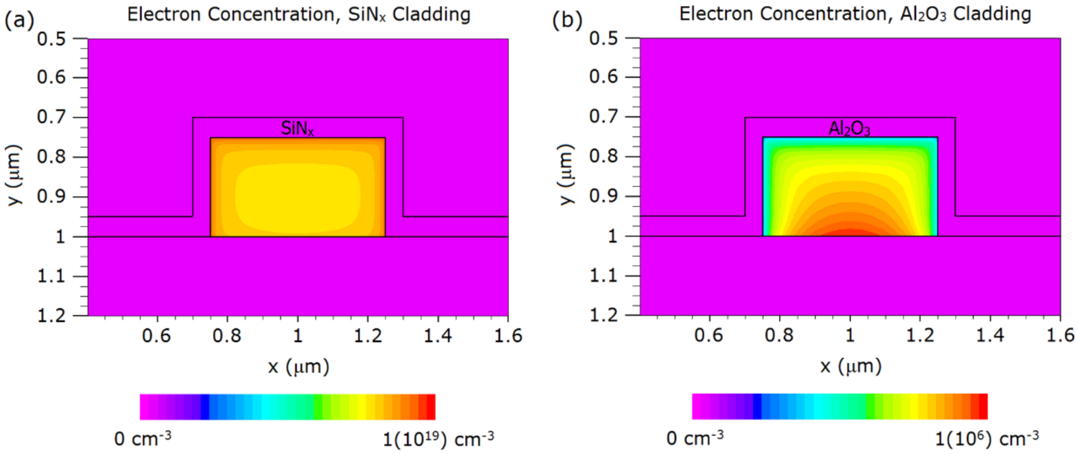

Figure 2.7. Electron concentration (log scale) in silicon waveguides clad with thin layers of either (a) silicon nitride or (b) aluminum oxide, followed by silicon dioxide.

The two waveguides' dissimilar electrical properties translate to optical effects through Eq. 2.8 and Eq. 2.9, and if we extend this analysis to consider nonzero bias voltages we may generate the electro-refractive and electro-absorptive plots shown in Fig. 2.8, which were created using Silvaco in combination with Lumerical. In this figure, we additionally consider the case of a silicon waveguide clad with silicon dioxide deposited through plasma-enhanced chemical vapor deposition (PECVD), which possesses a small positive charge.

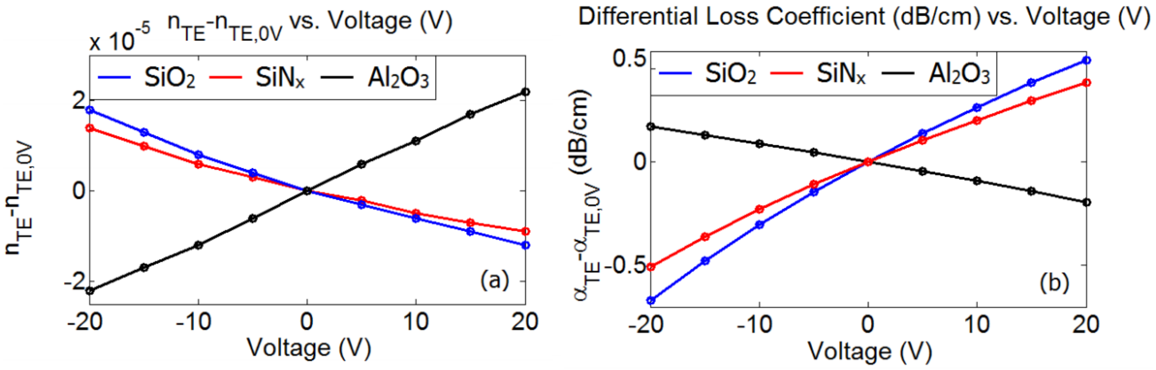

Figure 2.8. (a) Electro-refractive and (b) electro-absorptive behavior for the fundamental TE-like mode of silicon waveguides clad with either (blue) silicon dioxide, (red) silicon nitride, or (black) aluminum oxide.

It is important to note from Fig. 2.6 that, for the case of the aluminum oxide cladding, the slope of either of the electro-optic effects changes sign as compared to the other two claddings, and this is because of the opposite sign of the fixed charge.

We have additionally experimentally verified this predicted behavior by measuring the electro-optic effects of silicon ring resonators coupled to bus waveguides. To do so, we fabricated the three specified waveguide configurations in UCSD’s Nano3 cleanroom facility through a combination of electron beam lithography (EBL), reactive ion etching (RIE), plasma-enhanced chemical vapor deposition (PECVD), and atomic layer deposition (ALD) [25]. The results of this process are shown for the case of the silicon nitride cladding in Fig. 2.9a. The bias voltages were applied by creating aluminum electrodes on the samples, and the ring resonators’ transmission spectra were obtained by coupling a tunable laser into the devices via a lensed tapered fiber and collecting the transmitted light with an optical power meter.

The applied voltage induced shifts in the rings’ optical resonances, as shown for the case of the silicon dioxide cladding in Fig. 2.9b, and the transmission spectra of a ring resonators were then fit to Eq. 1.36 in order to extract the values of both the real and imaginary part of the modal refractive index. The results, shown in Fig. 2.9c and Fig. 2.9d, agree fairly well with the theoretical results, although some discrepancy is visible for the case of the silicon nitride cladding. This is likely due to the tendency of the fixed charge to vary in this case in response to the applied voltage, rather than remaining constant [26]. Nonetheless, it is clear from the results that fixed charge plays a significant role in determining the electro-optic behavior of these devices.

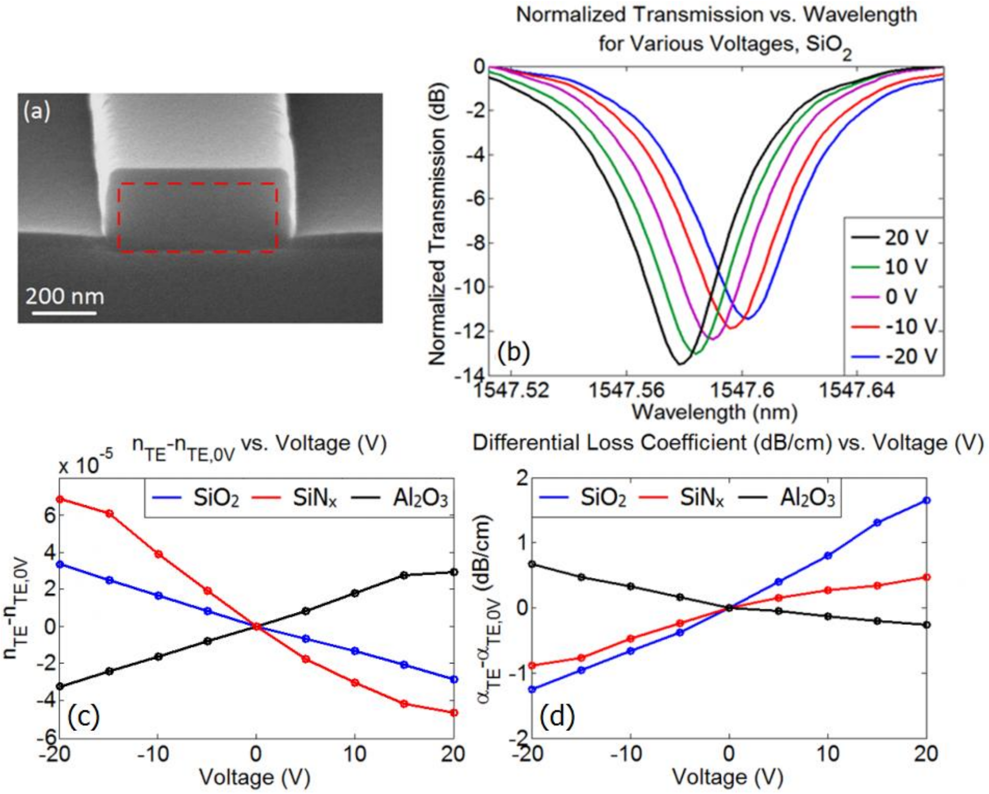

Figure 2.9. Experimental characterization of the effects of fixed charges on the electro-optic properties of silicon waveguides. (a) Scanning electron micrograph of one waveguide, clad with 50 nm of silicon nitride. (b) Voltage-dependent transmission spectra for a silicon waveguide clad with 1 µm of silicon dioxide. (c,d) Voltage dependence of the (a) real part of the effective index and (b) loss coefficient for the TE-like modes of the three waveguides.

When properly designed, capacitively-driven electro-optic modulators in silicon based on free-carrier plasma dispersion have the potential to exhibit low driving voltages, small device footprints, and high modulation bandwidths. In the following chapter, we will both theoretically and experimentally characterize the electro-optic properties of so-called “slot-rib” waveguides, which possess some of the highest sensitivities to bias voltages observed in the literature to date.

This chapter contains material which has been published in, "Tensor of the Tensor of the second-order nonlinear susceptibility in asymmetrically strained silicon waveguides: analysis and experimental validation,” Optics Letters (2014). The dissertation author was the primary investigator and author of this paper.

This chapter also contains material which has been published in, "Effect of dielectric claddings on the electro-optic behavior of silicon waveguides,” Optics Letters (2016). The dissertation author was the primary investigator and author of this paper.

Bibliography

1. R. Jacobsen, K. Andersen, P. Borel, J. Fage-Pedersen, L. Frandsen, O. Hansen, M. Kristensen, A. Lavrinenko, G. Moulin, H. Ou, C. Peucheret, B. Zsigri, and A. Bjarklev, “Strained silicon as a new electro-optic material,” Nature **441**, 199-202 (2006).

2. B. Chmielak, M. Waldow, C. Matheisen, C. Ripperda, J. Bolten, T. Wahlbrink, M. Nagel, F. Merget, and H. Kurz, “Pockels effect based fully integrated, strained silicon electro-optic modulator,” Optics Express **19**, 17212-17219 (2011).

3. J. Fage-Pedersen, L. Frandsen, A. Lavrinenko, and P. Borel, “A linear electrooptic effect in silicon, induced by use of strain,” 3rd IEEE International Conference on Group IV Photonics (2006).

4. T. Suhara, M. Fujimura, *Waveguide Nonlinear Optic Devices*, Springer (2003).

5. M. Puckett, J. Smalley, M. Abashin, A. Grieco, and Y. Fainman, “Tensor of the second-order nonlinear susceptibility in asymmetrically strained silicon waveguides: analysis and experimental validation,” Optics Letters **39**, 1693-1696 (2014).

6. B. Chmielak, C. Matheisen, C. Ripperda, J. Bolten, T. Wahlbrink, M. Waldow, and H. Kurz, “Investigation of local strain distribution and linear electro-optic effect in strained silicon waveguides,” Optics Express **21**, 25324-25332 (2013).

7. D. Neamen, *Semiconductor Physics and Devices*, McGraw-Hill, Inc. (2003).

8. R. Sharma, M. Puckett, H. Lin, F. Vallini, and Y. Fainman, “Characterizing the effects of free carriers in fully etched, dielectric-clad silicon waveguides,” Applied Physics Letters **106**, 241104 (2015).

9. M. Webster, P. Gothoskar, V. Patel, D. Piede, S. Anderson, R. Tummidi, D. Adams, C. Appel, P. Metz, S. Sunder, B. Dama, and K. Shastri, “An efficient MOS-capacitor based silicon modulator and CMOS drivers for optical transmitters,” 11th International Conference on Group IV Photonics (2014).

10. X. Chen, Y. Chen, Y. Zhao, W. Jiang, and R. Chen, “Capacitor-embedded 0.54 pJ/bit silicon-slot photonic crystal waveguide modulator,” Optics Letters **34**, 602-604 (2009).

11. L. Alloatti, C. Koos, and J. Leuthold, “Optical loss by surface transfer doping in silicon waveguides,” Applied Physics Letters **107**, 031107 (2015).

12. Silvaco, Inc., http://www.silvaco.com

13. M. Nedeljkovic, R. Soref, and G. Mashanovich, “Free-Carrier Electrorefraction and Electroabsorption Modulation Predictions for Silicon Over the 1-14-µm Infrared Wavelength Range,” IEEE Photonics Journal **3**, 1171-1180 (2011).

14. M. Cazzanelli, F. Bianco, E. Borga, G. Pucker, M. Ghulinyan, E. Degoli, E. Luppi, V. Veniard, S. Ossicini, D. Modotto, S. Wabnitz, R. Pierobon, and L. Pavesi, “Second-harmonic generation in silicon waveguides strained by silicon nitride,” Nature Materials **11**, 148-154 (2012).

15. C. Schriever, F. Bianco, M. Cazzanelli, M. Ghulinyan, C. Eisenschmidt, J. de Boor, A. Schmid, J. Heitmann, L. Pavesi, and J. Schilling, “Second-Order Optical Nonlinearity in Silicon Waveguides: Inhomogeneous Stress and Interfaces,” Advanced Optical Materials **3**, 129-136 (2015).

16. A. Liu, L. Liao, D. Rubin, H. Nguyen, B. Ciftcioglu, Y. Chetrit, N. Izhaky, and M. Paniccia, “High-speed optical modulation based on carrier depletion in a silicon waveguide,” Optics Express **15**, 660-668 (2007).

17. Y. Jiang, W. Jiang, L. Gu, X. Chen, and R. Chen, “80-micron interaction length silicon photonic crystal waveguide modulator,” Applied Physics Letters **87**, 221105 (2005).

18. Z. Li, D. Xu, W. McKinnon, S. Janz, J. Schmid, P. Cheben, and J. Yu, “Silicon waveguide modulator based on carrier depletion in periodically interleaved PN junctions,” Optics Express **17**, 15947-15958 (2009).

19. L. Gu, W. Jiang, X. Chen, L. Wang, and R. Chen, “High speed silicon photonic crystal waveguide modulator for low voltage operation,” Applied Physics Letters **90**, 071105 (2007).

20. Q. Xu, B. Schmidt, S. Pradhan, and M. Lipson, “Micrometre-scale silicon electro-optic modulator,” Nature **435**, 3250327 (2005).

21. W. Green, M. Rooks, L. Sekaric, and Y. Vlasov, “Ultra-compact, low RF power, 10 Gb/s silicon Mach-Zehnder modulator,” Optics Express **15**, 17106-17113 (2007).

22. A. Liu, R. Jones, L. Liao, D. Samara-Rubio, D. Rubin, O. Cohen, R. Nicolaescu, and M. Paniccia, “A high-speed silicon optical modulator based on a metal-oxide-semiconductor capacitor,” Nature **427**, 615-618 (2004).

23. M. Webster, P. Gothoskar, V. Patel, D. Piede, S. Anderson, R. Tunnidi, D. Adams, C. Appel, P. Metz, S. Sunder, B. Dama, and K. Shastri, “An efficient MOS-capacitor based silicon modulator and CMOS drivers for optical

transmitters," IEEE 11th International Conference on Group IV Photonics, 1-2 (2014).

24. X. Chen, Y. Chen, Y. Zhao, W. Jiang, and R. Chen, "Capacitor-embedded 0.54 pJ/bit silicon-slot photonic crystal waveguide modulator," Optics Letters 34, 602-604 (2009).

25. R. Sharma, M. Puckett, H. Lin, A. Isichenko, F. Vallini, and Y. Fainman, "The effect of dielectric claddings on the electro-optic behavior of silicon waveguides," Optics Letters **41**, 1185-1188 (2016).

26. M. Bazilchuk, H. Haug, and E. Marstein, "Modulating the fixed charge density in silicon nitride films while monitoring the surface recombination velocity by photoluminescence imaging," Applied Physics Letters **106**, 143505 (2015).

Chapter 3:

Electro-Optic Modulation

3.1: Slot-Rib Waveguides

In capacitively driven silicon waveguides, changes in carrier concentration are generated by the application of a voltage across a finite thickness of dielectric material [1,2]. This was shown in Chapter 2.3, which specifically illustrated how the effect may change when a different dielectric material is chosen as a cladding material. In general, the magnitude of the electro-optic effects in the semiconducting region increase as the total thickness of the dielectric stack decreases, and this is because the length over which the applied voltage must fall decreases, forcing the semiconductor's free carriers to more pronouncedly redistribute themselves in order to accommodate a larger voltage difference. To more clearly illustrate this effect, we may compare the theoretical electron distributions in silicon waveguides with different silicon dioxide cladding thicknesses, assuming the same applied voltage for each case. The results, shown in Fig. 3.1, confirm that as the electrode spacing is reduced, the induced carrier redistribution becomes more pronounced. It should be noted that, as in the simulations shown in Chapter 2.1.2, these models assume no fixed charge along interfaces in order to improve clarity.

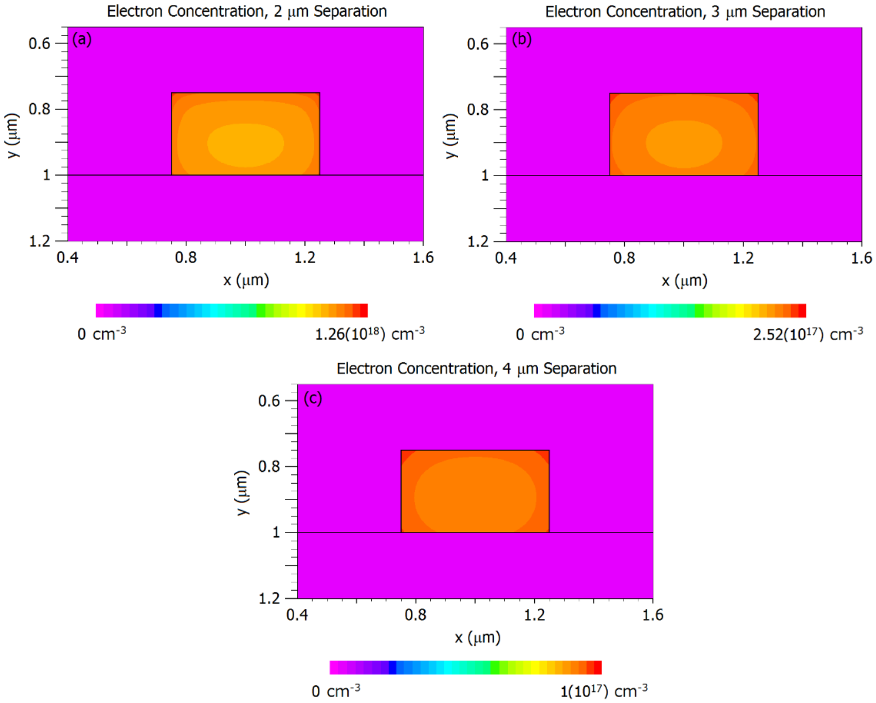

Figure 3.1. Theoretical electron concentrations (log scale) for a bias voltage of positive 2 V, assuming electrode separations of (a) 2 μm, (b) 3 μm, and (c) 4 μm. As the separation increases, the accumulation of electrons resulting from the applied voltage becomes less appreciable (note the different maxima of the scale bars).

As the total dielectric thickness between two electrodes becomes smaller, the applied voltage more strongly effects any semiconducting medium between them. The most efficient accumulation of carriers (electrons in the case of this particular case) is clearly achieved for the smallest electrode separation possible. However, as metallic electrodes are moved closer to the waveguide, they interact more strongly with the supported optical modes, and this can lead to undesirable Ohmic loss. To illustrate this effect, Fig. 3.2 shows how the loss coefficient of the TE-like mode for a 500 nm-wide, 250 nm-tall silicon waveguide with an aluminum electrode above it (shown in Fig. 3.2a) changes as a function of the silicon dioxide cladding thickness. The plot, generated through the finite element method (FEM) software Comsol, shows how rapidly the ohmic loss increases as the cladding thickness is reduced to values less than 400 nm [3].

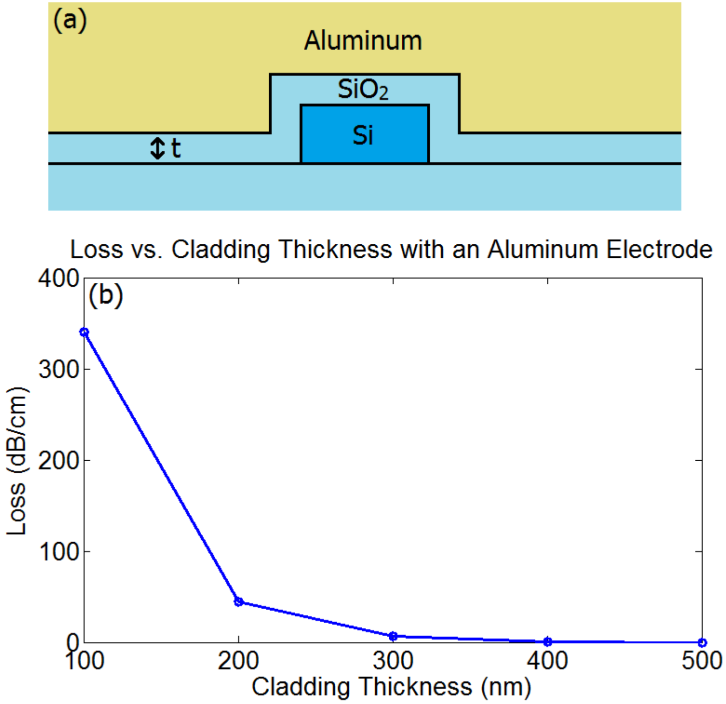

Figure 3.2. (a) Cross-section of a silicon waveguide clad with a thickness, t, of silicon dioxide, followed by an aluminum layer. (b) Ohmic propagation loss of the waveguide’s TE-like mode as a function of the silicon dioxide cladding thickness.

To circumvent this inherent trade-off between modulation efficiency and loss, one prospective technique would be to use the silicon device layer itself to apply the driving voltage, employing a ridge waveguide with a 50 nm-wide slot along its center. Doing so completely removes the necessity for metallic electrodes, eliminating any ohmic loss present in the system and allowing for an effective electrode separation orders of magnitude smaller than what has been previously considered. In the following chapter, we will present a theoretical analysis of the proposed waveguide geometry, as well as conducting a preliminary experimental characterization of its aptitude for electro-optic modulation.

3.1.1: Modeling

The goal of the slot-rib waveguide is to exhibit an improved sensitivity to bias voltages, applied as shown in Fig. 3.3a, due to a decreased separation between the two electrodes and an improved overlap between the optical mode and the induced free-carrier effects. The proposed waveguide geometry is additionally expected to have sufficiently low propagation losses due to a lack of any metallic electrodes. In Fig. 3.3b, we confirm through FEM models that that this type of waveguide supports a TM-like mode, and Fig. 3.3c and Fig. 3.3d show the results of Silvaco simulations, highlighting how strongly the waveguide's electrons redistribute for an applied voltage of only 1 V as opposed to the unbiased case. In these simulations, the waveguide is assumed to be unclad, eliminating the complicating effect of fixed charge along semiconductor-dielectric interfaces.

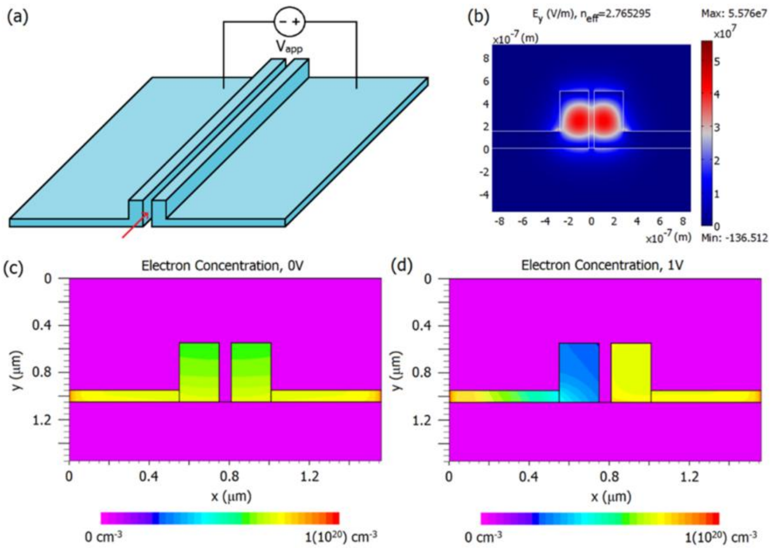

Figure 3.3. (a) Illustration of the proposed slot-rib waveguide configuration. (b) Electric field of the TM-like mode supported by the waveguide cross-section. (c,d) Theoretical electron concentrations (log scale) within the waveguide, assuming bias voltages of (c) 0 V and (d) 1 V.

As in the case of the more conventional waveguides considered in Chapter 2.3, we may translate the changes in carrier concentration to changes in the effective index of the waveguide's TM-like mode through use of Eq. 2.8 and Eq. 2.9, and the results this treatment yields are shown in Fig. 3.4. As anticipated, the reduction of the electrode spacing from several microns to only 50 nm significantly increases the magnitude of both of the predicted electro-optic effects. Changing the applied voltage from +1 V to +4 V, for example, already generates a larger differential change in the real part of the modal effective index than any of the analogous values for conventional waveguides observed experimentally in Fig. 2.7c. Furthermore, the symmetry of the waveguide cross-section results in even behavior, making the electro-optic effects sensitive only to the magnitude of the applied voltage and not its sign. These results suggest that, if incorporated into an electro-optic modulator, the slot-rib waveguide geometry may allow for an appreciable decrease in the bias voltage required to reduce the transmitted power by 3 dB, the minimum amount required for digital switching applications [4].

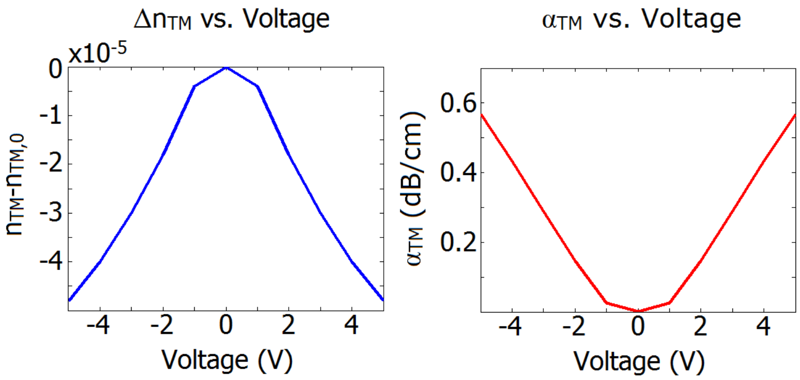

Figure 3.4. Theoretical electro-optic effects for the slot-rib waveguide, in terms of (a) the real part of the TM-like mode's effective index and (b) its absorption coefficient.

3.1.2: Fabrication and Preliminary Characterization

Based on these promising results, we have confirmed that the proposed slot-rib waveguide geometry may in fact be fabricated, and the fabrication process is illustrated in Fig. 3.5. We began with a silicon-on-insulator wafer consisting of a 500 nm-thick device layer and a 3 μm-thick buried oxide layer. In the first electron-beam lithographical step, we left the thin slot along the waveguide's center exposed and etched through the entire device layer. Following this, we aligned a second lithographical step to the first and etched 400 nm into the pedestal of the rib waveguide, resulting in the intended waveguide cross section.

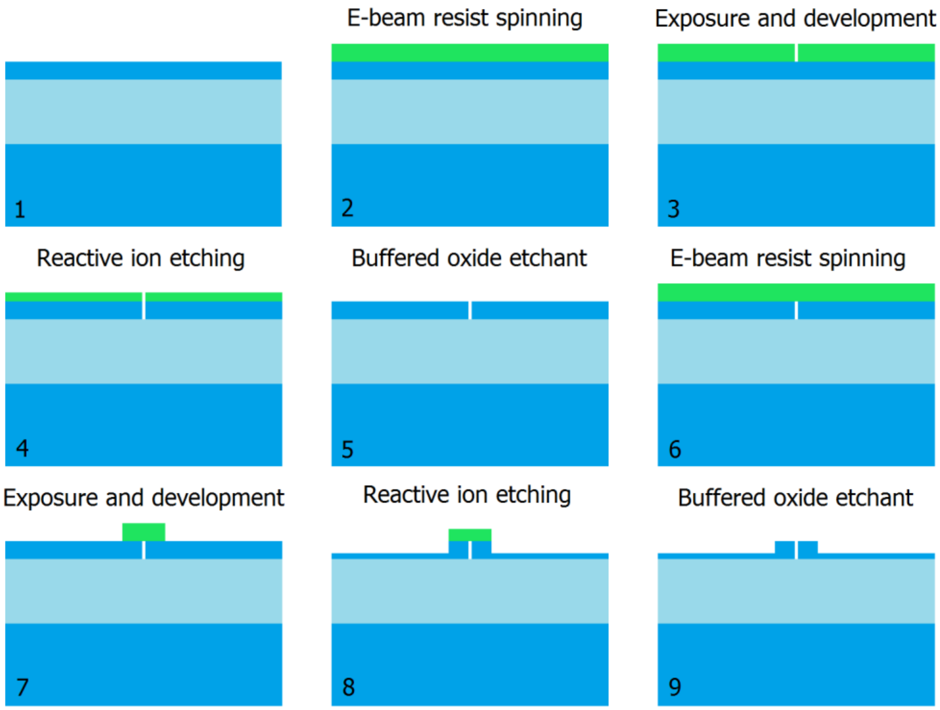

Figure 3.5. Fabrication process for the proposed slot-rib waveguide. In the illustrations, blue corresponds to silicon, light blue corresponds to silicon dioxide, and green corresponds to the electron beam resist hydrogen silsesquioxane (HSQ).

The results of this fabrication process are given in Fig. 3.6a, which shows a cross-sectional image of a slot-rib waveguide. The observed structure possesses a 60 nm-wide central slot, two 200 nm-wide ridges, and a 110 nm-thick pedestal, deviating only slightly from the target dimensions.

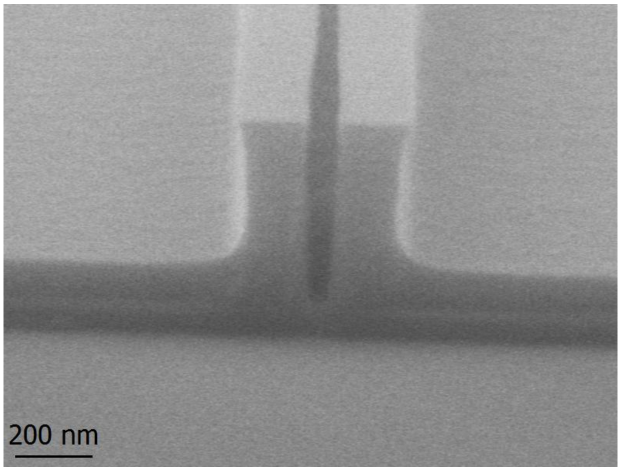

Figure 3.6. Cross-sectional SEM micrograph of the slot-rib waveguide, confirming that the center slot (shown to be approximately 60 nm wide) has etched through the entire silicon device layer. (b) Overhead SEM micrograph of a slot waveguide ring resonator, which is comparable in terms of its passive optical properties to the slot-rib geometry.

Before characterizing the electro-optic effects of these waveguides, it was important to test their passive optical properties and ascertain their validity for integrated optical applications. To do this, we measured the absorption coefficients of fully etched slot waveguides, which are known to have comparable passive optical properties to the slot-rib geometry. As in previous sections, this was done through the use of ring resonators coupled to bus waveguides as shown in Fig. 3.6b. The slot waveguides were 500 nm tall, the slots were 50 nm wide, and the two silicon nanowires making up the guiding material were 200 nm wide. Again, the theoretical transmission spectrum through a bus waveguide coupled to a ring resonator is as given by Eq. 1.36, and the experimentally measured transmission spectrum for our fully etched slot bus waveguide is as shown in Fig. 3.7.

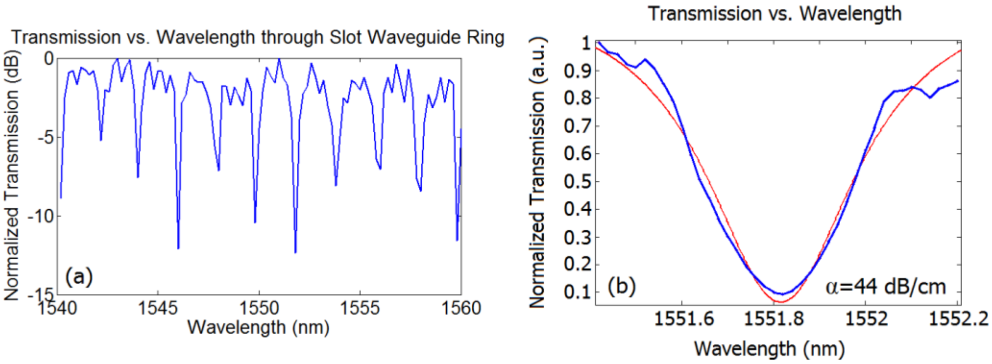

Figure 3.7. (a) Measured transmission spectrum of the TM-like mode in a slot waveguide coupled to a slot waveguide ring resonator. (b) Zoomed-in plot of the transmission for a single resonance of the ring (blue), shown along with a Lorentzian curve fit to the data (red).

From this data, we can extract a passive loss coefficient for the TM-like mode supported by the structure of 44 dB/cm. This value is larger than that of typical silicon waveguides, and this is because of the high degree of modal overlap with the etched silicon sidewalls at the center of the waveguide, which leads to scattering loss. However, this loss value is still low enough to allow electro-optic modulation, and is in fact smaller than the values reported in other capacitively operated modulators to date [1,2].

We additionally measured the effective index of the TM-like mode supported by the slot waveguides through the use of Bragg gratings, as shown in Fig. 3.8a. The effective index may be calculated simply from the measured Bragg wavelength and the grating period as:

$$n = \frac{\lambda_B}{2\Lambda} \tag{3.1}$$

where λ_B is the Bragg wavelength and Λ is the grating period. The transmission through four different Bragg gratings in silicon slot waveguides is shown in Fig. 3.8, and the effective index extracted from these measurements at a wavelength of 1520 nm is 2.30.

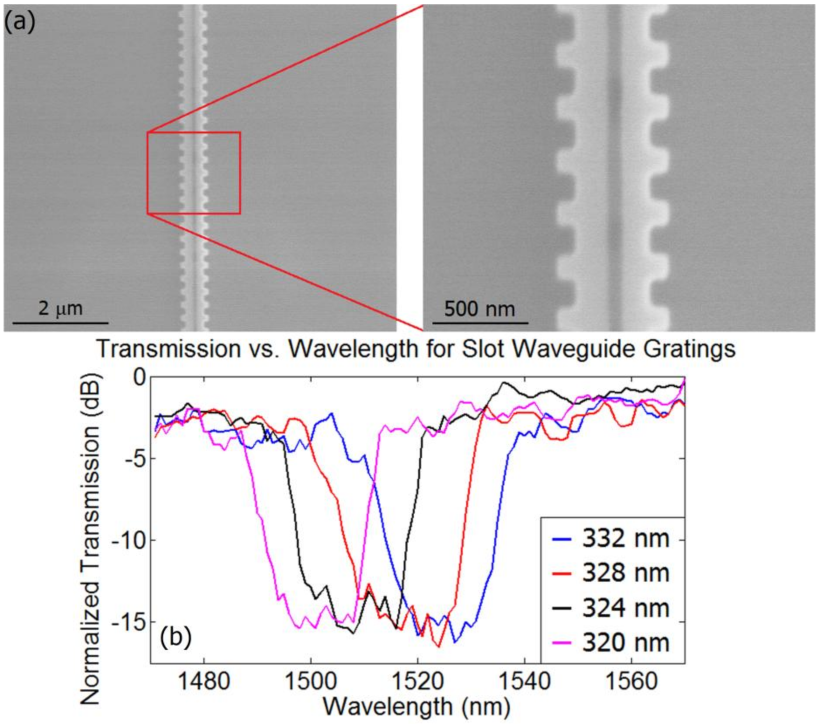

Figure 3.8. (a) SEM micrograph of a Bragg grating fabricated in a slot waveguide. (b) Measured transmission spectra of the TM-like mode in a slot waveguide through Bragg gratings with different modulation periods. For each grating, the modulation of the waveguide width was ±50 nm.

3.1.3: Theoretical Performance

The slot-rib waveguide's improved performance stems from the reduction of the dielectric thickness across which the bias voltage is applied, which is theoretically shown to increase the magnitude of the free-carrier effects generated in the silicon ribs. Based on these preliminary results, we have seen that the slot-rib waveguide geometry may be readily fabricated, and that the propagation loss exhibited by comparable structures, namely slot waveguides, are low enough to allow for efficient electro-optic modulation. Moderately increased propagation loss was observed for slot waveguides, and was attributed to an increased modal overlap with etched sidewalls, but the measured value of 44 dB/cm is still lower than the values reported in the literature for comparable structures. The slot-rib waveguide geometry is anticipated to have somewhat lower loss due to the incomplete second etch step, which reduces the total cross-sectional length of the etched sidewalls, and this will translate to a lower insertion loss in electro-optic modulators.

In future work, which will focus on the actual demonstration of modulation in these waveguides, ring resonators will likely be employed, and this is due to the fact that they are more tolerant to high losses than Bragg resonators [5]. The proposed device layout, illustrated in Fig. 3.9, couples a slot-rib bus waveguide to a slot-rib resonator, and based on the theoretically and experimentally obtained properties of the waveguide reported on previously, we may predict the performance of this device prior to its fabrication.

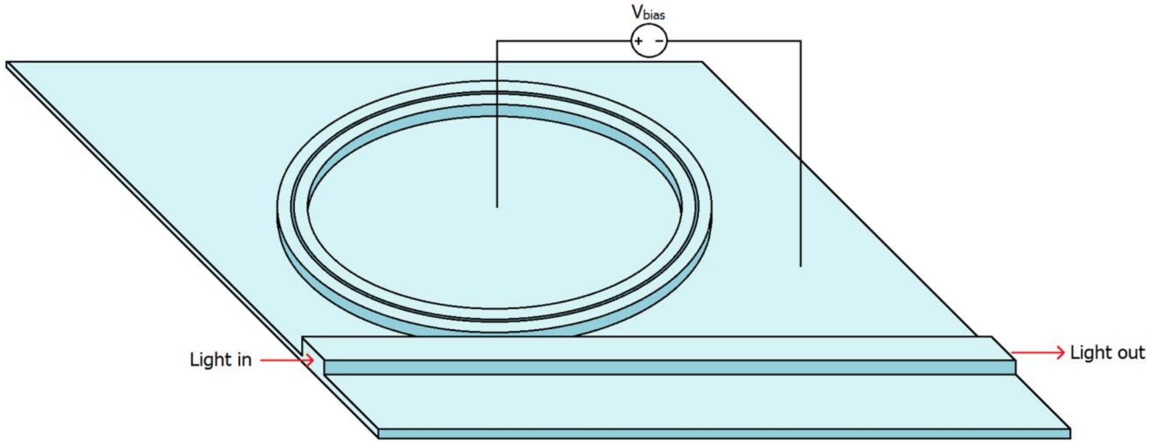

Figure 3.9. Schematic of the theoretically considered device, which relies on the enhanced electro-optic effects in slot-rib waveguides and the narrow spectral characteristics of ring resonators.

Employing Eq. 1.39, we may create theoretical transmission spectra for our proposed device. The passive spectrum is shown for a 100 μm-radius resonator in Fig. 3.10a, alongside the spectrum under an applied bias voltage of +2 V. As illustrated in the figure, changing the operating wavelength similarly changes the power swing attainable via the applied voltage, while similarly altering the insertion loss.

By considering several different ring radii, assuming critical coupling may be attained in each case by choosing the appropriate separation between the ring and bus waveguides, we can see how the power swing varies as a function of the insertion loss for each prospective device. Assuming that the propagation loss is 40 dB/cm, a value comparable to the one measured experimentally for the fully-etched slot waveguides, optimal performance is achieved for a ring radius of 100 μm. The target power swing of 3 dB may be achieve for this device for an applied voltage of +2 V (a voltage swing of ±1 V) and an insertion loss of approximately 12 dB. If the propagation loss is reduced, through either improved etch chemistries or post-etch RCA cleans [6-8], the insertion loss may be reduced without compromising device performance in terms of the required switching voltage.

Perhaps the most appealing aspect of the 100 μm-radius device is that, at a total area of less than 40000 μm^2, in does not require the use of a travelling wave electrode and may instead be driven with a simpler lumped electrode. The photon lifetime within the cavity, a parameter which is critical to the device bandwidth, may be measured from the Q-factor of the resonance using Eq. 1.42. The optical bandwidth of the 100 μm-radius modulator, which may be taken to be the inverse of the photon lifetime, is plotted in Fig. 3.10 for each of the considered ring radii, and each of the devices shows sufficiently high bandwidths for high-data-rate applications [9].

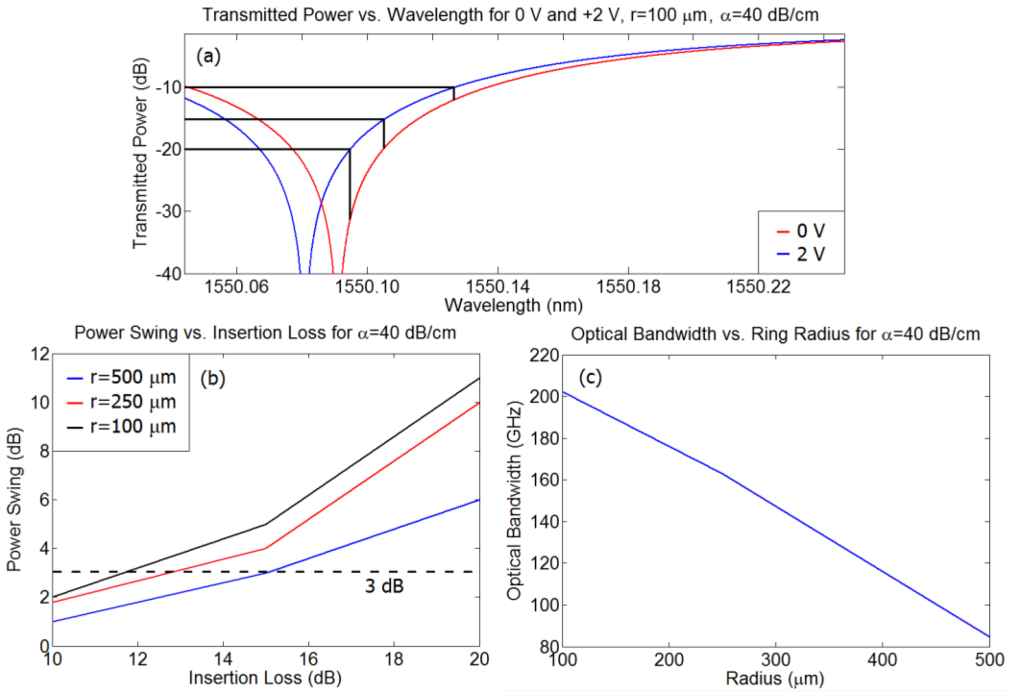

Figure 3.10. (a) A portion of the transmission spectra for 100 μm-radius slot-rib waveguide rings, assuming 40 dB/cm of propagation loss, and either 0 or +2 V of bias. Black lines indicate the trade-off between the electro-optic power swing and instertion loss. (b) Power-swing vs. instertion loss for ring resonant modulators with different radii. (c) Optical bandwidth as a function of ring radius.

Finally the energy-per-bit, an interesting value to consider in the context of electro-optic modulation, may be calculated from the effective device capacitance as:

$$E_{bit} = \frac{1}{2} C V_{3dB}{}^{2} = \frac{1}{2}\left(\frac{\varepsilon_0 L h}{d}\right) V_{3dB}{}^{2} \tag{3.2}$$

where L is the circumference of the ring, 628 μm, h is the height of the device layer, 500 nm, d is the slot width, 50 nm, and V_{3dB} is the voltage required to change the output power by 3 dB, 2V. For our device, this term equates to 111 fJ.

3.2: Hybrid Waveguides

In the field of electronics, so-called “high-k” dielectrics are desirable candidates for the realization of high-performance transistors. In general, high-k dielectrics are electrical insulators with exceptionally large dielectric constants at low to moderate modulation frequencies [10], and the benefit of such materials is that the electric fields within them may be significantly smaller than those within a lower-k dielectric, given the same transistor geometry and applied voltage. Because of this, a lower voltage falls across the dielectric, causing larger portions of applied voltages to drop across neighboring semiconductors. This effect is illustrated in the simple one-dimensional Silvaco models shown in Fig. 3.11, which compare two semiconductor-oxide-semiconductor (SOS) structures consisting of either silicon dioxide (k equal to 3.9) or titanium dioxide (k equal to 80) [12]. For the former case, approximately 30% of the applied voltage drops across the silicon dioxide, whereas for the high-k dielectric structure only 10% of the voltage drops across the titanium dioxide. This reduction in the voltage drop across the dielectric is beneficial because it increases the magnitude of any free-carrier effects which occur in the semiconductor, and this has obvious applications to the slot-rib waveguide modulator discussed in the previous section.

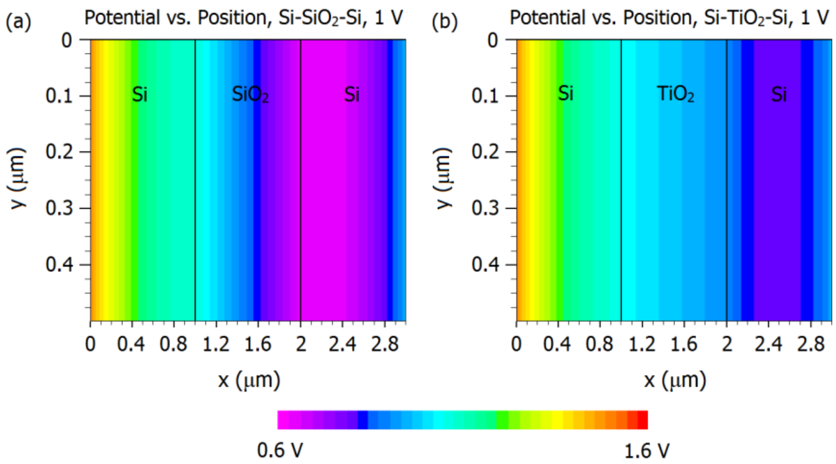

Figure 3.11. Electric potential across capacitive structures, including (a) silicon dioxide or (b) titanium dioxide, assuming an applied voltage of 1 V. (a) The voltage drop across the dielectric is approximately .7 V and the total voltage drop in the silicon is .3 V. (b) The voltage drop across the dielectric is approximately .2 V and the total voltage drop in the silicon is .8 V.

Titanium dioxide may be deposited through atomic layer deposition, and we have already demonstrated the deposition of highly conformal thin films, as shown in Fig. 3.12. The electrical properties of thin dielectric films can be determined through a capacitance-voltage measurement on silicon. In these commonly employed measurements [11,12], metal-oxide-semiconductor (MOS) structures are created by fabricating metallic electrodes on the deposited dielectric films and measuring their frequency- and voltage-dependent capacitances. The low-frequency permittivity of the dielectric may be extracted from the capacitance in the accumulation regime as [13]:

$$\varepsilon_r = \frac{Cd}{\varepsilon_0 A} \tag{3.2}$$

where C is the measured capacitance, d is the dielectric film thickness, and A is the area of the metallic electrode. Similarly, the fixed charge present at the semiconductor-dielectric interface may be calculated as [13]:

$$Q_f = \left(\phi_{ms} - V_{FB}\right)\frac{\varepsilon_d}{d} \tag{3.3}$$

where φ_{ms} is the work function difference between the metal and the semiconductor, V_{FB} is the measured voltage at which the semiconductor switches from accumulation to depletion (observed as an abrupt change in the capacitance), and ε_d is the dielectric's permittivity, $\varepsilon_d = \varepsilon_0 \varepsilon_r$. Past research efforts have shown through CV measurements that titanium dioxide may possess dielectric constants as high as 100 [14], and in the following section, we will see how this allows it to improve the performance of electro-optic modulators based on capacitive free-carrier dispersion.

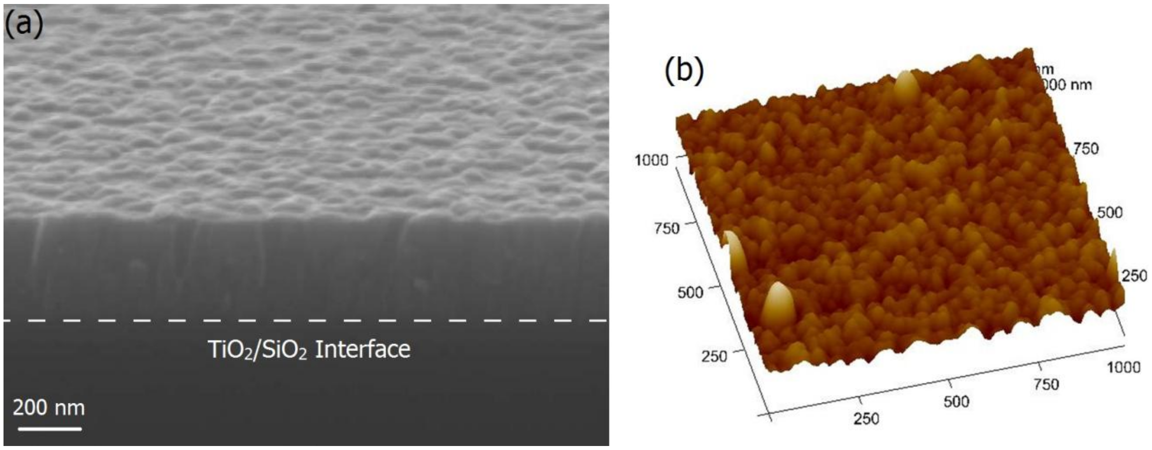

Figure 3.12. (a) SEM micrograph of a 400 nm-thick titanium dioxide film deposition on silicon dioxide. (b) Diamond stylus profilometer-obtained roughness profile for the deposited titanium dioxide film.

Just as we did for the case of unclad slot-rib waveguides, we were able to theoretically model the electro-optic behavior of dielectric-clad slot-rib waveguides by combining Silvaco simulations with Lumerical models. In Silvaco, we assumed the same waveguide geometry as that shown in Fig. 3.13, with the inclusion of a 50 nm-thick dielectric layer. The dielectric material was assumed to be either silicon nitride, with a k of 10, or titanium dioxide, with a k of 100, and the fixed charge at the semiconductor-dielectric interface was assumed to be zero for simplicity. Fig. 3.13a summarizes the results of these electro-optic simulations, confirming that as the dielectric constant of the dielectric layer increases, the strength of the free-carrier effects in the silicon waveguide increases as well. Fig. 3.13b plots the band-bending in one of the silicon portions of the waveguide as a function of the dielectric constant, and by comparing this plot with Fig. 3.12a it appears as if the electro-optic effect is roughly linearly proportional to this value. Considering the results shown in Fig. 3.13b, it is clear that the incorporation of a high-k dielectric layer into the slot-rib waveguide has the potential to reduce the switching voltage from ±1 to ±.5V, and to reduce the switching energy from 111f J to 28 J. Alternatively, the enhanced electro-optic effect may be used to reduce the insertion loss from 12 to 9 dB while holding the other metrics constant.

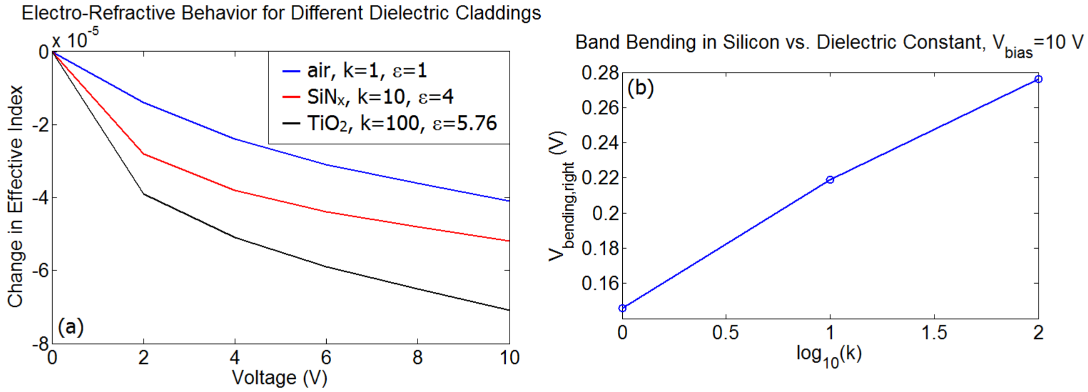

Figure 3.13. (a) Change in the real part of the effective index of the TM-like mode in a slot-rib waveguide as a function of the applied voltage, for several different electrical permittivities of the cladding layer. (b) Band-bending within the right silicon pedestal, assuming an applied voltage of 10 V, as a function of the cladding layer's electrical permittivity.

This chapter contains material which is being prepared for submission. The dissertation author was the primary investigator of this work.

Bibliography

1. A. Liu, R. Jones, L. Liao, D. Samara-Rubio, D. Rubin, O. Cohen, R. Nicolaescu, and M. Paniccia, “A high-speed silicon optical modulator based on a metal-oxide-semiconductor capacitor,” Nature **427**, 615-618 (2004).

2. M. Webster, P. Gothoskar, V. Patel, D. Piede, S. Anderson, R. Tunnidi, D. Adams, C. Appel, P. Metz, S. Sunder, B. Dama, and K. Shastri, “An efficient MOS-capacitor based silicon modulator and CMOS drivers for optical transmitters,” IEEE 11th International Conference on Group IV Photonics, 1-2 (2014).

3. COMSOL, Inc., http://www.comsol.com

4. B. Jalali and S. Fathpour, “Silicon Photonics,” Journal of Lightwave Technology **24**, 4600-4615 (2006).

5. A. Grico, B. Slutsky, and Y. Fainman, “Characterization of waveguide loss using distributed Bragg reflectors,” Applied Physics B **114**, 467-474 (2014).

6. D. Sparacin, S. Spector, and L. Kimerling, “Silicon waveguide sidewall smoothing by wet chemical oxidation,” Journal of Lightwave Technology **23**, 2455-2461 (2005).

7. H. Sun, A. Chen, D. Abeysinghe, A. Szep, and R. Kim, “Reduction of scattering loss of silicon slot waveguides by RCA smoothing,” Optics Letters **37**, 13-15 (2012).

8. K. Inoue, D. Plumwongrot, N. Nishiyama, and S. Arai, “Loss Reduction of Si Wire Waveguide Fabricated by Edge-Enhancement Writing for Electron Beam Lithography and Reactive Ion Etching Using Double Layered Resist Mask with C60,” Japanese Journal of Applied Physics **48**, 3R (2009).

9. G. Reed, G. Mashanovich, F. Gardes, and D. Thomson, “Silicon optical modulators,” Nature Photonics **4**, 518-526 (2010).

10. G. Wilk, R. Wallace, and J. Anthony, “High-κ gate dielectrics: Current status and materials properties considerations,” Journal of Applied Physics **89**, 5243 (2001).

11. H. Casey, G. Fountain, R. Alley, B. Keller, and S. DenBaars, “Low interface trap density for remote plasma deposited SiO2 on n-type GaN,” Applied Physics Letters **68**, 1850 (1996).

12. B. Hoex, J. Gielis, M. van de Sanden, and W. Kessels, “On the c-Si surface passivation mechanism by the negative-charge-dielectric Al2O3,” Journal of Applied Physics **104**, 113703 (2008).

13. S. Sze and K. Ng, *Physics of Semiconductor Devices*, Wiley (1981).

14. J. Kim, D. Kim, H. Jung, and K. Hong, “Influence of anatase-rutile phase transformation on dielectric properties of sol-gel derived TiO2 thin films,” Japanese Journal of Applied Physics **44**, 447-451 (2006).

Chapter 4:

Second-Harmonic Generation

As mentioned in Chapter 2, second-harmonic generation (SHG) is an important form of wavemixing, the general term for nonlinear phemonena which convert optical energy among different wavelengths. In SHG, light at a fundamental wavelength, called the pump, interacts with a medium to create a nonlinear polarization proportional to the square of the instantaneous pump electric field. As a result of this quadratic dependence, the nonlinear polarization contains a frequency component at twice that of the pump in addition to a DC component [1], and may therefore reemit electromagnetic radiation at the second-harmonic frequency. This process, which has been outlined in Chapter 2.2, is desirable for applications in which optically carried data need to be replicated at new carrier wavelengths. Furthermore, demonstrating this effect with a high conversion efficiency in a CMOS-compatible material platform allows more readily for integration with existing electronics technology. To this end, the following chapter demonstrates theoretical and experimental results for SHG in (1) waveguides composed purely of silicon nitride, and (2) hybrid waveguides consisting of both silicon nitride and silicon.

4.1: Silicon Nitride Waveguides

Silicon nitride is an interesting candidate for many integrated photonics applications. It has a moderately high index of refraction ranging from 1.9-2.2, allowing for good confinement of optical modes, and because it is a dielectric material rather than a semiconductor, such detrimental effects as electric field screening and free-carrier plasma dispersion do not occur in it [2-4]. Since the late 1970’s, research groups around the world have been exploring the potential benefits of using silicon nitride waveguides in place of silicon waveguides, and propagation losses well below 1 dB/cm have been demonstrated experimentally [5]. Perhaps the most appealing quality of silicon nitride is that its transparency window extends into the visible wavelength spectrum, allowing it to guide light at wavelengths as low as 250 nm [6]. Silicon nitride is however a polycrystalline, or ceramic material, and this has historically been thought to make it effectively centrosymmetric, disallowing electro-optic modulation based on the Pockels effect as well as second-order wavemixing.

Recently, however, researchers have observed that silicon nitride may possess a small but appreciable second-order nonlinear susceptibility due to slight asymmetries and deviations away from the typical 3:4 Si:N stoichiometry [7]. The coefficients measured have, in general, been found to be highly dependent upon the exact conditions which are enforced during the material's deposition, and this work has revitalized the study of silicon nitride for nonlinear optical applications. To date, electro-optic modulation and effective second-harmonic generation based on a bulk $\chi^{(2)}$ have not been demonstrated, likely due to a general lack of understanding of the exact origin of the second-order nonlinearity in silicon nitride waveguides. In an effort to contribute to the ongoing work surrounding this intriguing material, we have fabricated our own silicon nitride waveguides and characterized their second- and third- order nonlinearities through SHG both with and without the assistance of EFISH.

4.1.1: Modeling

To predict the second-harmonic conversion efficiency in a silicon nitride waveguide, we may modify Eq. 2.14 as:

$$\kappa = \frac{\omega \varepsilon_0 \chi_{ijk}^{(2)}}{4} \iint_{SiN_x} E^{2\omega}\left(x,y\right)^{*}\left(x,y\right) E^{\omega}\left(x,y\right)^{2} dxdy \tag{4.1}$$

where E^{ω} and $E^{2\omega}$ are the normalized electric fields of the pump and second-harmonic modes supported by the waveguide. Specifically, Eq. 4.1 assumes the existence of some nonzero $\chi^{(2)}$ tensor component which transfers energy among two optical modes. As mentioned in Chapter 2, efficient second-harmonic generation will only occur when the effective indices of these two modes are exactly equal to one another. It should also be mentioned that the combined electric fields of two separate pump modes may interact with one another, coupling shared power into a second-harmonic mode. In this case, the average effective index of the two pump modes should equal that of the second-harmonic mode in order to achieve phase-matching [1].

For a 550 nm-tall silicon nitride waveguide with a sidewall slope of 83º (assumed for reasons which will become clear in the following section), Fig. 4.1a shows that phase-matching can occur between (1) a TM-like pump mode and a TM-like second-harmonic, (2,3) combined TM- and TE-like pump modes and either a TM- or TE-like second-harmonic, or (4) a TM-like pump mode and a TE-like second-harmonic. Because each of the involved modes is TM-polarized for case (1), we know that the process scales with the yyy-component of the $\chi^{(2)}$ tensor. Similarly, case (2) depends up the existence of the xxy component, which may also be nonzero. Cases (3) and (4) may be neglected because they assume a nonzero value of $\chi^{(2)}_{xyy}$, and symmetry considerations tell us that this value is identically required to equal zero [8].

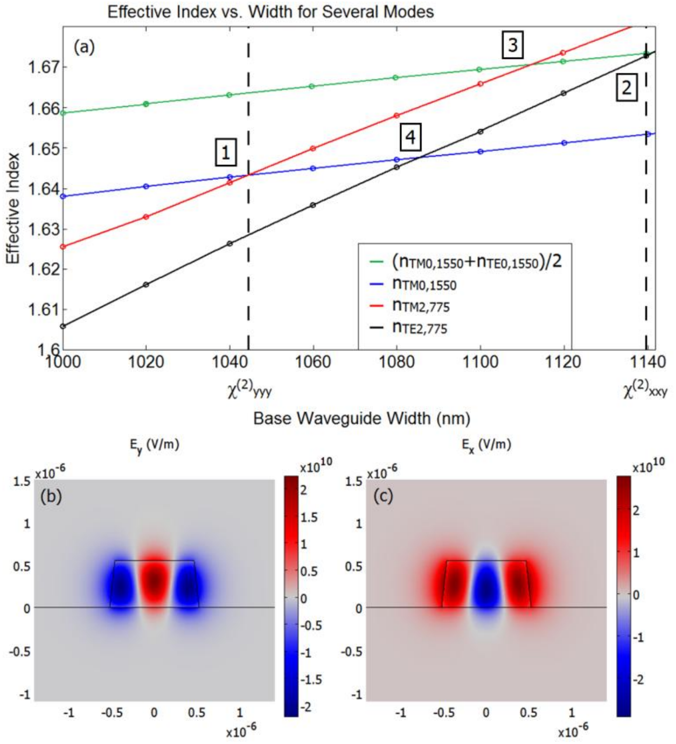

Figure 4.1 (a) Effective indices of the pump (blue) and two second-harmonic modes (red, black) as a function of the waveguide width, as well as the average effective index of the TE- and TM-like pump modes. (b,c) Electric field profiles of the TM- and TE-like second-harmonic modes, respectively.

Fig. 4.1b and Fig. 4.1c show, respectively, the profiles of the TM- and TE-like second-harmonic modes for this waveguide geometry. For case (1), assuming a phase-matched base waveguide width of approximately 1045 nm and a $\chi^{(2)}$ of 1 pm/V, the expression for the spatial evolution of the TM-like second-harmonic mode may be written as:

$$\frac{dA^{2\omega}(z)}{dz} = -j\left(1.926m^{-1}\right)A^{\omega}(z)^{2} - \frac{\alpha_{2\omega}A^{2\omega}(z)}{2} \tag{4.2}$$

where the first term on the right-hand side represents second-harmonic generation, with the term in parentheses equaling the coupling coefficient, and the second term on the right-hand side represents linear loss. $\alpha_{2\omega}$ is the loss coefficient of the second-harmonic mode, and A^{ω} is the amplitude of the pump, defined in turn as:

$$A^{\omega}(z) = A^{\omega}(0) - \frac{\alpha_{\omega}A^{\omega}(z)}{2} \tag{4.3}$$

In Eq. 4.3, $A^{\omega}(0)$ is the amplitude of the pump at the waveguide's input and α_{ω} is the loss coefficient of the pump mode. Fig. 4.2 plots the power in the second-harmonic as a function of waveguide length, assuming an input pump power of 25 mW, for several different loss values, and for simplicity we assume that these are the same for the pump and second-harmonic modes ($\alpha^{\omega}=\alpha^{2\omega}$).

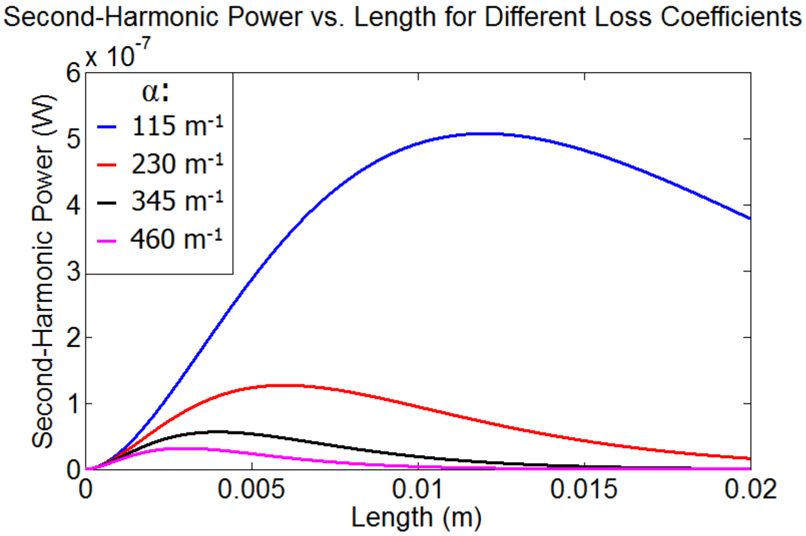

Figure 4.2 TM second-harmonic power as a function of propagation length, assuming phase-matching for several different loss coefficients and the waveguide cross-section and nonlinear coefficient specified in the text.

As Fig. 4.2 shows, more than just the maximum generated power changes with the loss coefficient. Additionally, the optimal waveguide length, at which the highest conversion efficiency will be achieved, increases as the loss coefficient decreases. Fortunately, silicon nitride is highly transparent at a wavelength of 1.55 μm, and silicon nitride waveguides have previously been measured to have propagation loss coefficients on the order of 4 dB/cm [9], which is low enough to be neglected for the waveguides we intend to fabricate. Based on our numerically generated results, we may fabricate silicon nitride waveguides for second-harmonic generation with a reasonable level of confidence.

4.1.2: Fabrication

To fabricate the silicon nitride waveguides for our second-harmonic generation experiment, we began as in Chapter 3 with silicon-on-insulator (SOI) wafers consisting of a 500 nm-thick device layer and a 3 µm-thick buried oxide layer. We removed the entire silicon device layer through submersion in a solution of dilute tetramethylammonium hydroxide (TMAH) heated to 80ºC, then deposited 550 nm of silicon nitride onto the samples using an Oxford Plasmalab Plasma-Enhanced Chemical Vapor Depositor (PECVD). We spin coated 330 nm of HSQ electron-beam resist, exposed the samples to patterns corresponding to waveguides, and removed the unexposed resist through development in a TMAH solution. Next, we etched through the unprotected silicon nitride layer through reactive ion etching using the gases C_4F_8 and SF_6, and clad the resulting waveguide with silicon dioxide through an additional PECVD step. To create electrodes, we finally deposited a 100 nm-thick aluminum layer on the silicon dioxide cladding through electron-beam evaporation. This fabrication process is illustrated in Fig. 4.3 along with an SEM micrograph of the resulting waveguide cross-section.

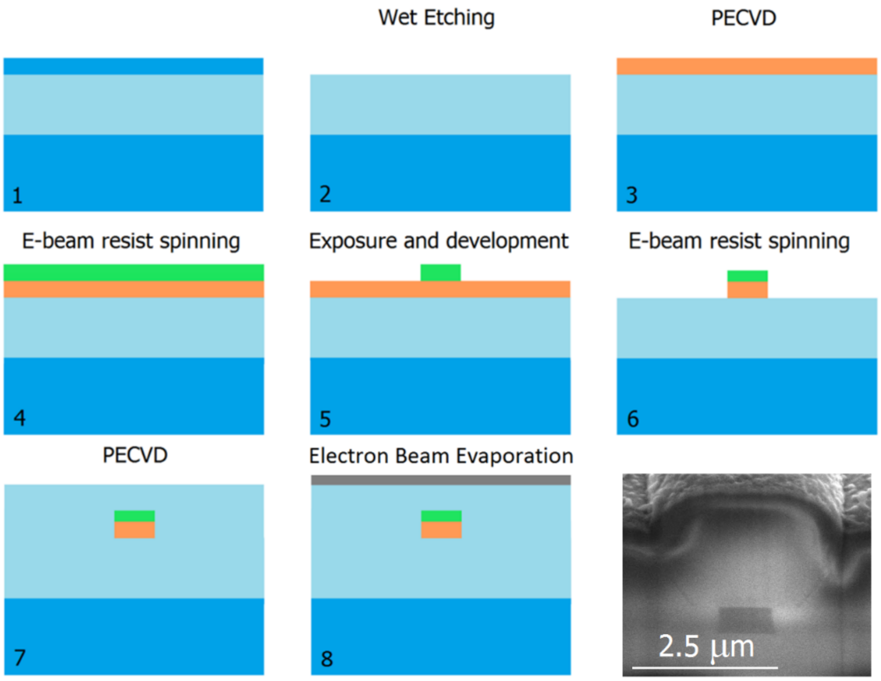

Figure 4.3 Illustration of the fabrication process for silicon nitride waveguides. In the figure, dark blue represents silicon, light blue represents silicon dioxide, orange represents silicon nitride, green represents HSQ, and gray represents aluminum. The bottom-right image is SEM micrograph showing the cross-section of a silicon nitride waveguide, including the aluminum electrode above it.

During the deposition of the silicon nitride layer, the flow rates of SiH_4, NH_3, and N_2 were maintained at 24, 276, and 600 sccm, respectively. These values were chosen to deposit films with low enough mechanical stress to avoid delamination [10,11]. The refractive index of the films was measured through interferometry using a Filmetrics Thin Film Measurement System, and was found to be approximately 1.96 at a wavelength of 1.55 µm.

We designed our silicon nitride waveguides to have widths ranging from 700 nm to 1.1 µm in order to achieve phase-matching in at least one device. As mentioned in the previous section, although there was very good agreement between the target waveguide width and the actual width at the base, the waveguide sidewalls were not completely vertical. Instead, the sidewalls slanted inward away from the base at a slope of 83º, leading to the width at the top of the waveguide being reduced by approximately 120 nm. This etch profile is shown in an SEM image of an unclad 1100 nm-wide waveguide, in Fig. 4.4. The image also shows the unetched HSQ layer above the waveguide, which creates a slight overhang.

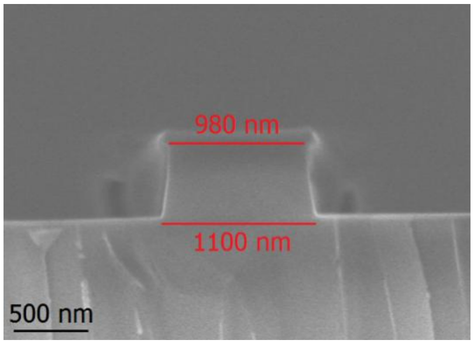

Figure 4.4 SEM micrograph of an unclad silicon nitride waveguide, showing the slope of the sidewalls and the remaining HSQ layer.

4.1.3: Results and Discussion

Confident that the fabricated structures would guide light at a wavelength of 1.55 μm with low propagation loss, we measured the transmission of our samples using the same experimental setup as that outlined in Chapter 2.3. Fig. 4.5 plots the transmission spectra of the fundamental TM-like mode for several different waveguide widths, for example. The silicon nitride exhibited significant absorption at wavelengths close to 1520 nm, but this effect vanished as the wavelength was increased. At wavelengths below 1500 nm, the mode supported by the 700 nm waveguide became partially deconfined, and its increased overlap with the waveguide's etched sidewalls resulted in an increase in loss. This effect was not however observed for the wider waveguides.

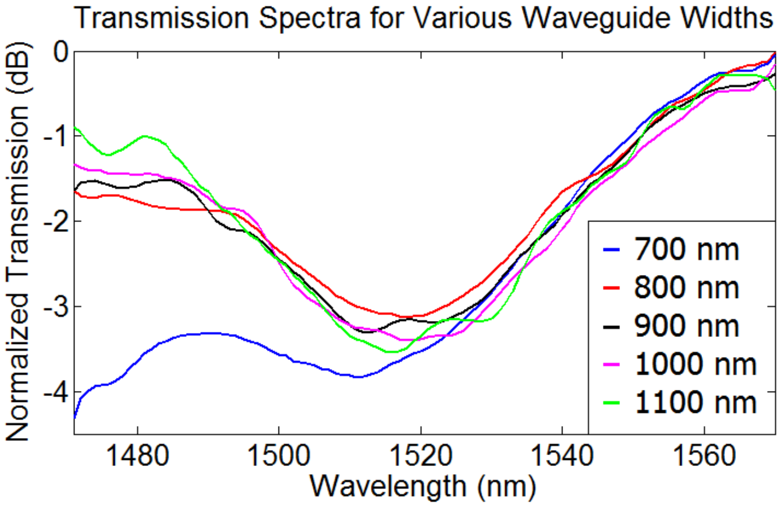

Figure 4.5. Transmission spectra of the TM-like mode supported by several different waveguide widths.

Following these preliminary measurements, we connected a high-power erbium-doped fiber amplifier (EDFA) to our tunable laser and injected approximately 1 W of optical power into each of the silicon nitride waveguides in turn. This modified experimental setup is shown schematically in Fig. 4.6.

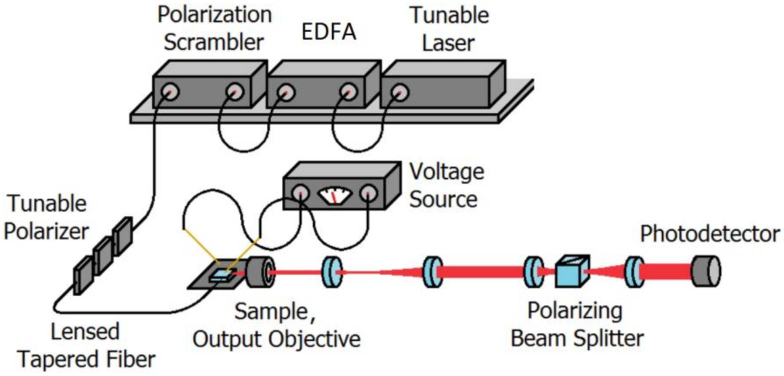

Figure 4.6. Schematic of the setup used to measure second-harmonic generation in silicon nitride waveguides, employing an erbium-doped fiber amplifier.

We optimized the coupling through our waveguides at a wavelength of 1550 nm, and following this optimization we positioned a free-space-to-fiber collimator in the transmitted beam's path, coupling the light through a CaF_2 fiber and into an Ocean Optics spectrometer. We then observed the signal received by the spectrometer for voltages ranging from 0 V to 500 V. As predicted by the models shown in Fig. 4.1, phase matching occurred between waveguide widths of 1100 and 1000 nm. Fig. 4.7a shows the phase-matched TE-like SHG signal, which is voltage-dependent, for a 1010 nm-wide waveguide and a pump wavelength of 1559 nm. Figh. 4.7b shows the voltage dependence of the peak count in the spectrometer, and a numerical fit confirms that the power in the second-harmonic scales quadratically with the voltage as anticipated.

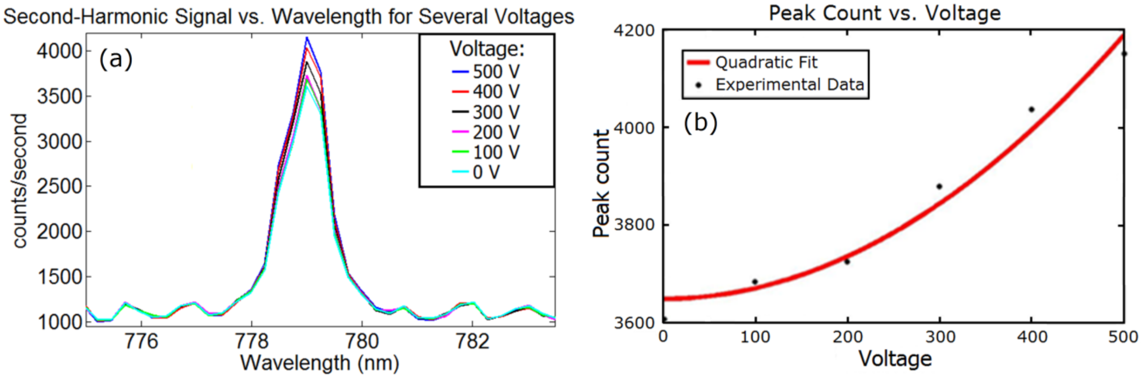

Figure 4.7. (a) The measured second-harmonic signal for a pump wavelength of 1559 nm, a waveguide width of 1010 nm, and a measured pump power at the waveguide's output of 30 mW. (b) Voltage dependence of the second-harmonic signal, as measured in (a), fit to a quadratic curve (R^2=.97).

It is important to note that, although the second-harmonic signal reduced as the applied voltage decreased, it had a nonzero value at 0 V. One possible explanation for this is that the silicon nitride we deposited has its own intrinsic $\chi^{(2)}$ value, as has been observed in the literature [7]. Alternatively, the unbiased signal could be the result of surface charges which exist along the interfaces between silicon nitride and silicon dioxide and lead to the existence of a built-in electric field. This field could lead to the generation of a second-harmonic signal through EFISH [12], even without the application of a bias voltage.

To confirm that the measured signal was in fact due to second-harmonic generation within the waveguide, we reduced the pump power and checked for quadratic dependence in the signal. The normalized results, presented in Fig. 4.8, verify the existence of the expected trend, giving us confidence that the signal is in fact generated as the pump propagates through the silicon nitride waveguides.

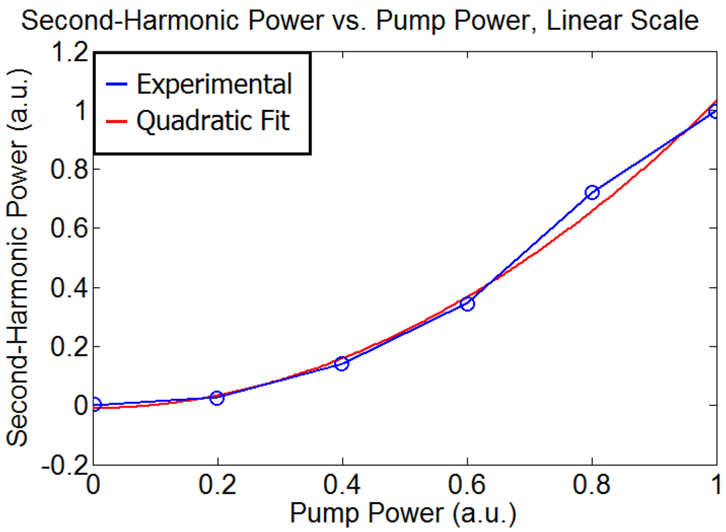

Figure 4.8. The dependence of the second-harmonic signal on the pump power measured at the waveguide's output. The quadratic fit, in red, shows good agreement with the measured data.

After observing phase-matched second-harmonic generation in our waveguides, we placed a visible power meter in the path of the transmitted light and collected the power in the second-harmonic signal for a 1010 nm-wide waveguide. The measured power is plotted against the pump wavelength for several different pump powers in Fig. 4.9, and in addition to again showing the quadratic dependence of the second-harmonic power on the pump power, these results reveal an interesting secondary effect. The measured second-harmonic signal appears to sit on a broad plateau which scales linearly with the pump power, which is the result of fluorescence due to impurities in the silicon nitride [13]. Nonetheless, the power contained at the second-harmonic wavelength may readily be distinguished from the plateau. Fig. 4.9b illustrates how the second-harmonic power scales quadratically whereas the fluorescence pedestal scales linearly with pump power. By inserting a second-harmonic power of 600 pW for 30 mW of pump power into Eq. 2.16 and Eq. 4.1, we were able to calculate the effective second-order nonlinear coefficient our waveguides possessed, $\chi^{(2)}_{\mathrm{eff,yyy}}$, as approximately .15 pm/V. It should be noted, however, that this treatment neglects loss within the waveguide at both the pump and second-harmonic wavelengths. The loss coefficient at 1550 nm may safely be assumed to be negligibly low, using reported values for comparable fabrication processes [9], and if we assume an upper limit for loss coefficient at 775 nm of 100 dB/cm, the extracted value of $\chi^{(2)}_{\mathrm{yyy}}$ only increases to .48 pm/V. We can therefore say with confidence that the actual value of $\chi^{(2)}_{\mathrm{yyy}}$ lies somewhere between .12 and .48 pm/V.

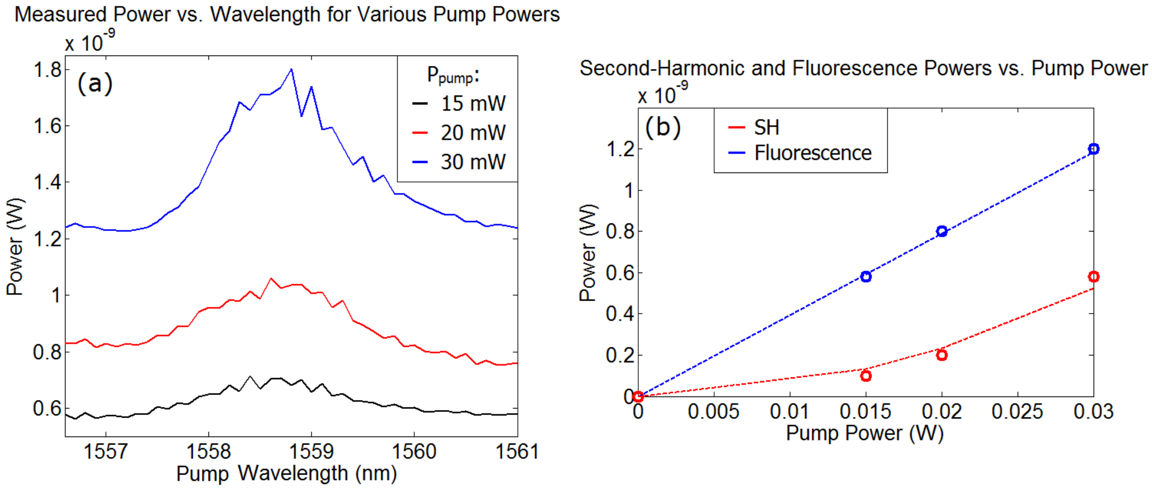

Figure 4.9. (a) The measured power at the output of a 1010 nm-wide waveguide, as a function of the pump wavelength, for several different pump powers. (b) Power dependence of the second-harmonic and fluorescence fit to quadratic and linear curves, respectively.

In addition to these measurements, we can also explore the existence of $\chi^{(2)}_{\mathrm{xxy}}$. For case (2) of the four phase-matching intersections discussed in Chapter 4.1.1, the coupled mode equation for the second-harmonic mode may be written as:

$$\frac{dA^{2\omega}(z)}{dz} = -j\left(.705m^{-1}\right)A^{\omega}(z)^{2} - \frac{\alpha_{2\omega}A^{2\omega}(z)}{2} \qquad (4.4)$$

where the number .705 is the Comsol-derived value of the coupling coefficient, assuming a $\chi^{(2)}_{xyy}$ of 1 pm/V. Phase-matching into the TE-like second-harmonic was observed for waveguides with a base width of 1070 nm at a pump wavelength of 1541 nm, and the measured second-harmonic power is plotted as a function of the pump wavelength in Fig. 4.10. Again, appreciable power is observed away from the phase-matched wavelength, and this is attributed once more to photoluminescence. Nonetheless, a phase-matched second-harmonic power of 110 pW may be extracted from the data. Applying a treatment identical to that used for $\chi^{(2)}_{yyy}$, we determine that the value of $\chi^{(2)}_{xxy}$ for these waveguides is between .06 and .22 pm/V.

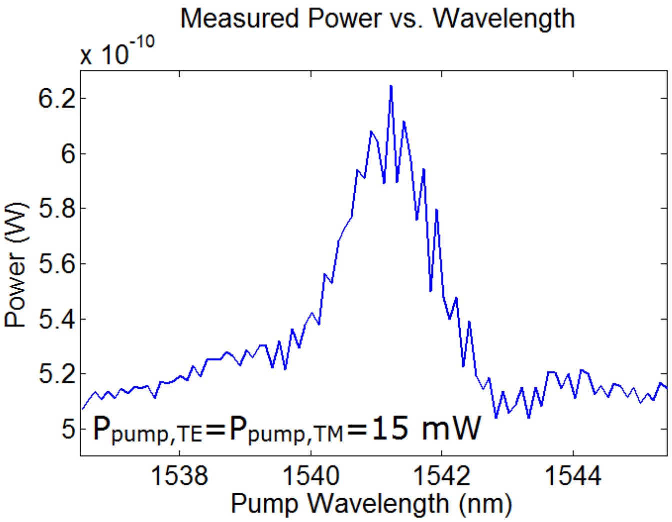

Figure 4.10. The measured TE power at the output of a 1070 nm-wide waveguide, as a function of the pump wavelength, for TE- and TM-like pump powers of 15 mW. The measured second-harmonic power is 110 pW, whereas the broad fluorescence power value is 510 pW.

Contrary to the commonly-held prediction that silicon nitride lacks a second-order nonlinear susceptibility, this work shows that silicon nitride waveguides may be made to possess effective second-order nonlinearities which approach in magnitude such nonlinear optical materials as gallium nitride, aluminum nitride, and gallium phosphide [14-16]. Coupled with silicon nitride's high transparency in the telecommunication wavelength regime and its dielectric nature, the results shown here make this material platform a strong candidate for the design of a wide range of integrated photonics devices. And perhaps most exciting, the tunability of the measured nonlinear coefficients suggests that new processes such as data-encoded second-harmonic generation may be possible in the future.

Additionally, recent work has shown through free-space measurements that increasing the silicon concentration in silicon nitride may lead to the formation of crystalline silicon nanoparticles, leading to a third-order nonlinear susceptibility greater than that of bulk crystalline silicon [17]. The implications of these results promise that the conversion efficiencies attainable through EFISH in waveguides which include silicon nitride may be significantly increased relative to the values shown here. In the following section, we will explore a prospective waveguide geometry consisting of silicon-rich silicon nitride as well as crystalline silicon, which could allow for the one of the highest SHG conversion efficiencies reported in a silicon-based integrated platform to date.

4.2: Hybrid Waveguides

The most significant result to take from our work with silicon nitride waveguides is that EFISH may serve as a practical tool for the realization of high conversion efficiency wavemixing. The results presented in Chapter 4.1 were limited, however, due to the large separation between the two electrodes used to induce the bias electric field. As in the case of electro-optic modulation, this limitation may be removed by moving to a slot-rib waveguide configuration in which the space between the two silicon ribs is filled with silicon nitride, as illustrated in Fig. 4.11. In such a waveguide, drastically larger electric fields could be applied for much smaller driving voltages, leading to larger effective second-order nonlinearities and consequent conversion efficiencies. Because silicon is however not transparent at wavelengths shorter than approximately 1.2 μm, the pump wavelength chosen for this prospective waveguide geometry would have to be greater than 2.4 μm. Nonetheless, the appeal of a hybridized slot-rib waveguide merits further consideration, and in this chapter we theoretically assess its aptitude for wavemixing based on EFISH. For the purposes of deriving an upper limit for the conversion efficiency, we will additionally assume that silicon-rich silicon nitride is used as the cladding material, corresponding to a significantly larger value of $\chi^{(3)}$.

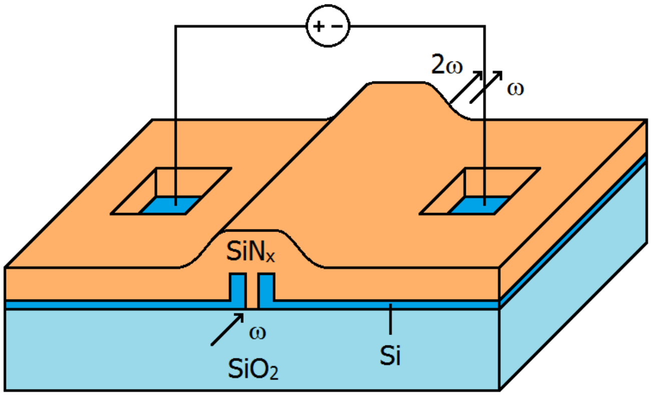

Figure 4.11. Schematic of the proposed hybridized slot-rib waveguide, in which an electric field may be applied across the silicon nitride between two silicon rib-like structures.

Just as in the case of the silicon nitride waveguides considered in Chapter 4.1, the evolution of the second-harmonic mode in a hybrid slot-rib waveguide may be calculated by determining the phase-matched dimensions and calculating the coupling coefficient. Assuming pump and second-harmonic wavelengths of 2.4 and 1.2 µm, respectively, we can use Comsol to determine that phase-matching is achieved between two TE-like modes when the waveguide's silicon ribs are 425 nm wide, the slot between them is 200 nm wide, and the silicon pedestal extending away from them is 50 nm tall. Fig. 4.12a shows how, as the slot width is increased, the effective index of the second-order second-harmonic mode first approaches and then surpasses that of the pump mode. Furthermore, Fig. 4.12b and Fig. 4.12c show the electric field profiles of these two modes, respectively.

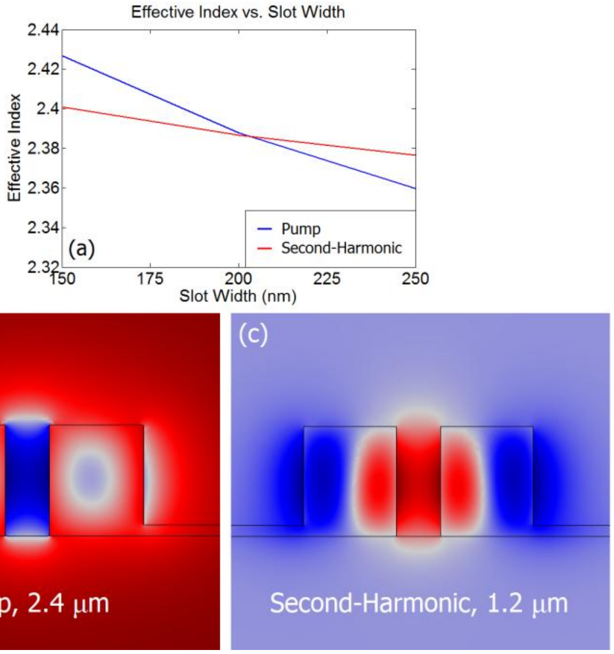

Figure 4.12. (a) Dependence of the pump and second-harmonic modes' effective indices on the width of the slot between the two silicon ribs. (b,c) Modle profiles of the (b) pump and (c) second-harmonic modes at the phase-matched waveguide dimensions.

As mentioned previously, the application of a bias voltage across the two silicon layers will generate a large electric field within the silicon nitride cladding. Using Silvaco, we are able to predict the magnitude of this field, and Fig. 4.13 shows the field for an applied voltage of 20 V. Assuming a third-order nonlinear susceptibility of $5.2(10^{-19})$ m^2/V^2 for silicon-rich silicon nitride [17], the nitride's effective second-order nonlinear susceptibility may be calculated through Eq. 2.17.

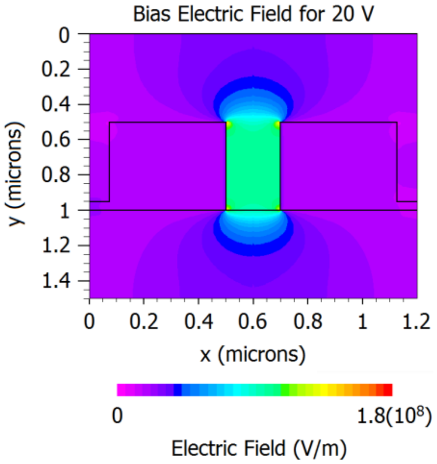

Figure 4.13. The bias electric field generated within a silicon nitride-clad slot-rib waveguide, assuming an applied voltage of 20 V.

As in the case of the conventional silicon nitride waveguide, the coupling coefficient of the waveguide may then be calculated by taking the overlap of the two optical modes within the nonlinear material and multiplying it by the second-order nonlinear susceptibility. For the phase-matched slot-rib waveguide, our expression defining the spatial evolution of the second-harmonic mode may be written as:

$$\frac{dA^{2\omega}(z)}{dz} = -j\left(\chi^{(3)}E_{DC}\left(2.64\left(10^{11}\right)Vm^{-2}\right)\right)A^{\omega}(z)^{2} - \frac{\alpha_{2\omega}A^{2\omega}(z)}{2} \tag{4.5}$$

where $\chi^{(3)}$ is the third-order nonlinear susceptibility of the silicon-rich silicon nitride cladding layer and E_{DC} is the applied bias field, equal in turn to:

$$E_{DC} = 5.5\left(10^{6}\right)V_{DC} \tag{4.6}$$

where V_{DC} is the applied voltage. For an applied voltage of 20 V, the coupling coefficient is then equal to 15.11 m^{-1}, which is roughly two orders of magnitude larger than the values obtained experimentally for the conventional silicon nitride waveguide. It should be noted that the EFISH effect may also occur in silicon, but in the geometry under consideration here, the electric field applied to the dielectric cladding layer is approximately an order of magnitude larger than that applied to the semiconductor region. If we assume that the third-order nonlinear susceptibility of the silicon-rich silicon nitride is comparable to that of silicon, as has been reported in the literature, then any contribution to second-harmonic generation due to EFISH in silicon may be neglected

Fig. 4.14a plots the theoretical second-harmonic power as a function of propagation length, assuming a pump power of 30 mW, for several different applied voltages, and Fig. 4.14b shows how the conversion efficiency through a 1 cm-long waveguide, in %W^{-1}, scales as the voltage is increased. This is of course neglecting optical loss, and provides only an upper limit on the practically realizable figures of merit. Nonetheless, the reported breakdown field for silicon nitride, 2.12(10^8) V/m [18], is achieved for a bias voltage of 38.5V, and at this upper maximum the conversion efficiency reaches a maximum possible value of 8.9%W^{-1}.

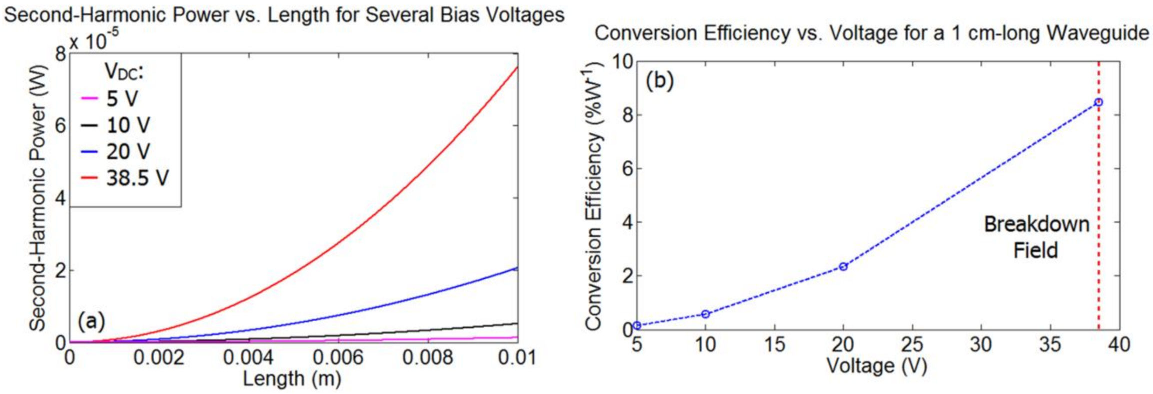

Fig. 4.14. (a) Theoretical plot of the second-harmonic power generated in a silicon-rich silicon nitride slot-rib waveguide, plotted as a function of length, for several different applied voltages. (b) Conversion efficiency for different applied voltages, assuming 1 cm of propagation. The red dashed line indicates the point of dielectric breakdown.

Based on these theoretical results, the hybrid slot-rib waveguide clad with silicon-rich silicon nitride is expected to outperform its more conventional predecessor, albeit for longer pump wavelengths in order to maintain optical transparency. As the suggested waveguide geometry does not rely on any fabrication steps which have not already been demonstrated directly, it stands to reason that an experimental validation of the behavior predicted here should be carried out in order to fully assess the potential for silicon-rich silicon nitride to act as a nonlinear material for second-order wavemixing applications.

This chapter contains material which has been submitted for publication in, "Observation of second-harmonic generation in silicon nitride waveguides through bulk nonlinearities," Optics Letters. The dissertation author was the primary investigator and author of this paper.

This chapter also contains material which is being prepared for submission. The dissertation author was the primary investigator of this work..

Bibliography

1. T. Suhara, M. Fujimura, *Waveguide Nonlinear Optic Devices*, Springer (2003).

2. D. Moss, R. Morandotti, A. Gaeta, and M. Lipson, "New CMOS-compatible platforms based on silicon nitride and Hydex for nonlinear optics," Nature Photonics **7**, 597-607 (2013).

3. J. Levy, A. Gondarenko, M. Foster, A. Turner-Foster, A. Gaeta, and M. Lipson, "CMOS-compatible multiple-wavelength oscillator for on-chip optical interconnects," Nature Photonics **4**, 37-40 (2010).

4. S. Khan, J. Chile, J. Ma, and S. Fathpour, "Silicon-on-nitride waveguides for mid- and near-infrared integrated photonics," Applied Physics Letters **102**, 121104 (2013).

5. W. Stutius and W. Streifer, "Silicon nitride films on silicon for optical waveguides," Applied Optics **16**, 3218-3222 (1977).

6. N. Manavizadeh, A. Khodayari, and E. Asl-Soleimani, "An investigation of the properties of silicon nitride (SiN_x) thin films prepared by RF sputtereing for application in solar cell technology," Proceedings of ISES World Congress 2007, 1120-1122 (2007).

7. T. Ning, H. Pietarinen, and O. Hyvarinen, "Strong second-harmonic generation in silicon nitride films," Applied Physics Letters **100**, 161902 (2012).

8. R. Sharipov, "Quick introduction to tensor analysis," arXiv.org (2004).

9. K. Ikeda, R. Saperstein, N. Alic, and Y. Fainman, "Thermal and Kerr nonlinear properties of plasma-deposited silicon nitride/silicon dioxide waveguides," Optics Express **17**, 12987-12994 (2008).

10. M. Hughey and R. Cook, "Massive stress changes in plasma-enhanced chemical vapor deposited silicon nitride films on thermal cycling," Thin Solid Films **460**, 7-16 (2004).

11. A. Gondarenko, J. Levy, and M. Lipson, "High confinement micron-scale silicon nitride high Q ring resonator," Optics Express **17**, 11366-11370 (2009).

12. S. Kielich, "Optical second-harmonic generation by electrically polarized isotropic media," IEEE Journal of Quantum Electronics **5**, 562-568 (2003).

13. Y. Wang, Y. Wang, L. Cao, Z. Cao, "High-efficiency visible photoluminescence from amorphous silicon nanoparticles embedded in silicon nitride," Applied Physics Letters **83**, 3474 (2003).

14. C. Sun, S. Chu, S. Tai, S. Keller, U. Mishra, and S. DenBaars, "Scanning second-harmonic/third-harmonic generation microscopy of gallium nitride," Applied Physics Letters **77**, 2331 (2000).

15. W. Pernice, C. Xiong, C. Schuck, and H. Tang, "Second harmonic generation in phase matched aluminum nitride waveguides and micro-ring resonators," Applied Physics Letters **100**, 223501 (2012).

16. K. Rivoire, Z. Lin, F. Hatami, W. Masselink, and J. Vuckovic, "Second harmonic generation in gallium phosphide photonic crystal nanocavities with ultralow continuous wave pump power," Optics Express **17**, 22609-22615 (2009).

17. C. Torres-Torres, A. Lopez-Suarez, L. Tamayo-Rivera, R. Rangel-Rojo, A. Crespo-Sosa, J. Alonso, and A. Oliver, "Thermo-optic effect and optical third order nonlinearity in nc-Si embedded in a silicon-nitride film," Optics Express **16**, 18390-18396 (2008).

18. S. Habermehl, R. Apodaca, and R. Kaplar, "On dielectric breakdown in silicon-rich silicon nitride thin films," Applied Physics Letters **94**, 012905 (2009).

Chapter 5:

Conclusion

The work presented in this dissertation provides evidence that such desirable functionalities as electro-optic modulation and second-harmonic generation may be improved upon, in comparison to the performance attainable by silicon nanowire and rib waveguides, by instead utilizing hybrid silicon-dielectric waveguides with carefully chosen cross-sections. Specifically, the slot-rib waveguide considered here has been shown to exhibit drastically reduced driving voltages as compared to previously demonstrated electro-optic modulators based on capacitively-induced free-carrier effects. This results from the minimization of the distance between the two materials across which driving voltages are applied. Whereas previous modulator geometries apply these voltages across several microns, the slot-rib waveguide does so across approximately 100 nm, leading to significantly stronger effects within the two halves of the semiconductor waveguide.

This dissertation has furthermore shown how the inclusion of high-k dielectrics in slot-rib modulator geometries forces applied voltages to drop within the semiconductor waveguide, rather than across the dielectric itself. This effect leads, as shown, to an additional enhancement to the measured electro-optic effects, yielding theoretical switching voltages as low as ±.5 V. This trend of improvement is predicted to continue as dielectric materials with even higher dielectric constants are explored.

It has additionally been experimentally demonstrated that silicon nitride, a material previously thought to be inadequate for second-order applications such as second-harmonic generation, possesses an appreciable, bulk second-order susceptibility which can be leveraged in an integrated platform. By combining silicon-rich silicon nitride with silicon slot-rib waveguides, it has been theoretically predicted that extremely high conversion efficiencies may be attainable via phase-matched second-harmonic generation, and future work is anticipated to demonstrate this experimentally.

The primary intent of this dissertation has been to persuade the reader to understand the unique benefits attainable by integrated waveguides which deviate in design from the conventional nanowire waveguides typically reported on. By including deeply subwavelength slots in the waveguide geometry, extremely high bias electric fields may be made to interact with propagating electromagnetic waves, and their interaction may be used in a number of ways in nonlinear optical devices. Either through such interesting processes as capacitive free-carrier modulation or electric field-induced second-order wavemixing, these waveguides show promise for the significant improvement of a wide range of device metrics. It is the author's hope that the work done here will encourage the design of a new wave of integrated photonics device components which drastically outperform their predecessors.